Response to reviewers' comments of Olin et al.: "Using a combined power law and log-normal distribution model to simulate particle formation and growth in a mobile aerosol chamber"

We thank the reviewers for their detailed and very useful comments, and have corrected the manuscript according to them.

Referee reports are in *black italic* and authors' responses are in blue roman font. The changes to the manuscript provided as the marked-up manuscript and the changed manuscript are included at the end of this file.

Referee 1 comments:

In their manuscript, "Using a combined power law and log-normal distribution model to simulate particle formation and growth in a mobile aerosol chamber", M. Olin, T. Anttila and M. Dal Maso have described a novel method for simulating the dynamics of aerosol particles, with the emphasis on simulating the early growth of a freshly-formed particle mode in a computationally cost-efficient manner. The authors have tested their model against previous aerosol dynamics models in a few simplified test scenarios to estimate the accuracy of the novel model, and also to demonstrate both the computational efficiency of the novel model in comparison to more accurate models and the accuracy of the novel model in comparison to other models with similar computational burden. Finally, the authors have used the model to reproduce a new particle formation and growth event as observed in aerosol chamber measurements. The main conclusions of the paper are that the newly- developed model is able to provide concentration, surface area and mass concentrations within a few percent to those obtained with a highly accurate model, and that the novel model is able to represent simultaneous new particle formation and particle growth, which is beyond purely log- normal model, which is often used for cost-efficient representation of an aerosol population.

Based on the results presented in the manuscript, the new model seems like a useful compromise between accurate and computationally cost-efficient representations of a particle population, and the manuscript is in the scope of ACP journal. A more thorough evaluation of the model is needed, however, and the language of the manuscript should be revised.

The evaluation of the model is now improved, and the language of the manuscript is checked once more.

General comments:

The main objectives of the manuscript are: 1) to describe the new model in detail, 2) to evaluate the accuracy and computational cost-efficiency of the model, and 3) to demonstrate the applicability of the model using a real life example. I find that the first objective is covered quite well in the manuscript. The second objective, however, is not covered sufficiently: the new model is evaluated against more accurate models in a handful of scenarios, but a more thorough examination is needed. The main issue is that only size-independent growth rates are considered. Another issue is the parameter γ, which is left as a free parameter in the model, but relatively little consideration is given to how sensitive the model results are to the choice of γ, or, especially, how to choose the value of γ for given simulation conditions. These, and some other issues, are described in more detail in the "Specific comments", below. Regarding the third objective, a single example of reproducing the time evolution of a particle size distribution during a new particle formation and growth event as observed in a chamber experiment is provided. A few different examples would probe the capabilities of the model much more comprehensively. Even more problematic, however, is that in this example, the particle formation and growth rates representing the measurement conditions are obtained with inverse modelling using another, more accurate, model, and those values are used as input in the novel model with the results being compared to the results from the more accurate model. In other words, the only connection to the real life measurement is that the formation and growth rates used as inputs in the models represent the measurement conditions, but otherwise there is not much difference to the scenarios used to evaluate the model. A more suitable demonstration of the usage of the model would be, for example, to estimate the formation and growth rates representing the measurements using inverse modelling with both the accurate model and the novel model, and then compare those values. Finally, the language of the manuscript is not very good at times. The grammatical errors are not exhaustively listed in the "Technical corrections", and a greater care for punctuation, for example, would be needed.

A more thorough examination to the model is now done. An additional case, where the condensational growth rate is size-dependent, is added to the test cases. Information on how to choose the value of the condensational transfer factor γ is added.

The part of inverse modelling is now separated from the part in which the accuracy and the computational cost of the model is examined. Inverse modelling is done using different models, the combined power law and log-normal distribution (PL+LN) model, a simple log-normal (LN) model, and highly accurate models, a fixed-sectional (FS400) and a moving-center fixed sectional (MC100) model. Additionally, the text describing the manually performed trial and error method in finding the best estimates for the functions of the new particle formation (J) and condensational growth rates (g) is now removed. Instead, a computationally executed least squares method is used to find the best estimates that the most accurately provide the measured number (N), surface area (S), and mass (M) concentrations at every time moment of the centers of the Nano-SMPS scans. In this way, the performance of the PL+LN model in inverse modelling is also examined by comparing the different time series of J and g. In other words, all four models have now straight connection to the real-world data. The associated computing time of the automatic inverse modelling procedure using the PL+LN model was approximately 2 orders of magnitude shorter than by using the FS400 or the MC100 model, which implies that a significant improvement in the computing time can be obtained using the PL+LN model in the case of inverse modelling.

The time series of J and g obtained from the FS400 model are then used in the examination of the accuracy and the computational cost of the models, because the comparison of the model outputs is best done by assuming that the FS400 model output is the correct one, not the measured data. In this way, the errors of the model outputs are best seen because the differences of the model outputs are mainly caused by numerical diffusion and the assumptions included in the models.

The language of the manuscript is checked once more.

Specific comments:

1. The title of the manuscript implies that the new model is able to simulate the actual process of particle formation, which is misleading, as the formation rate is used as an input in the model, and also that the emphasis of the manuscript would be on simulations related to the mobile aerosol chamber, but only one example is given. The title should be revised.

The PL+LN model is now able to simulate the actual process of particle formation, which is shown by performing the inverse modelling using the PL+LN model straightly to the measured data. The manuscript also includes the equations with which the condensational growth rate can be calculated from the vapor concentrations. With those equations, the actual process of particle formation could be simulated with the model if the vapors participating in particle formation and growth were known. The particle formation event measured with the mobile aerosol chamber has now a bigger role in the manuscript, because the inverse modelling part is widened. Therefore, the title is kept unchanged.

2. On page 7, lines 19-23, it is stated that the mass growth rate is assumed to be proportional to D_p^2 in the model, even though only one of the three conditions justifying that assumption is met. Then, on page 8, line 1, it is stated that this assumption of proportionality results to condensational growth rate being size-independent. The growth rates observed in the atmosphere, however, are not size- independent for the particle size range considered in the model (e.g., Kuang et al., 2012). Furthermore, in all of the simulations used to evaluate the new model, the growth rate is assumed to be size-independent. In other words, the model includes an approximation that is in contradiction to observation, but the error caused by this approximation is not probed at all when evaluating the model accuracy. This is a considerable omission, and additional simulations with size-dependent growth rates should be added. The sectional models used as reference obviously do not suffer from this approximation.

It is true that the growth rates for the particle size range considered in this manuscript can be size-dependent. However, because the exact function for the condensational growth rate is usually unknown due to unknown vapors participating in the growth process, and because this manuscript concentrates on the description of the PL+LN model, the main focus is on size-independent condensational growth rates.

An additional test case having size-dependent g is, however, included in the test cases now to probe the model more extensively. The function chosen for $g(D_\mathrm{p})$ is calculated by assuming condensational growth due to sulfuric acid and water vapors in

an atmospheric environment. The resultant function is shown in Fig. 1, from which it can be seen that g increases very steeply at small particle diameters and then remains nearly a constant. Particle diameters in this case lie mainly in the range between 1.6 and 7 nm. In that range, g varies significantly, and therefore, the applicability of the PL+LN model with size-dependent g is probed well with this case. Figure 2 shows the produced size distributions. Due to steeply increasing g at the smallest particle sizes, the size distribution is of a different form, which can be seen in the size distribution produced by the FS1000 model. This kind of size distribution does not follow a power law form, and therefore the PL+LN model is not able to express the distribution correctly at very small particle sizes. The relative errors of the concentrations produced by the PL+LN model compared to the FS1000 model are up to 17 $\%$ in this case. Nevertheless, the LN model behaves even more unsatisfactorily; the relative errors rise up to 90 $\%$.

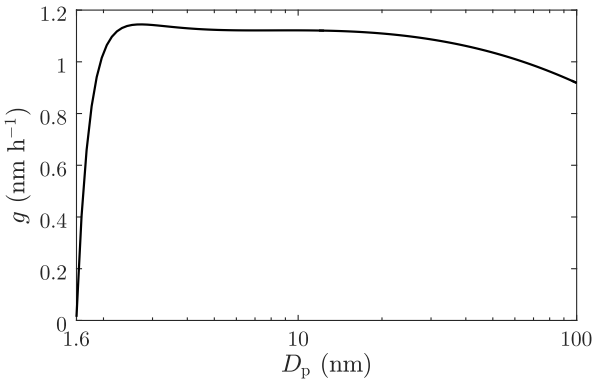

Figure 1. Size-dependent condensational growth rate of sulfuric acid-water particles with the sulfuric acid vapor concentration of $0.8 \times 10^7\,\mathrm{cm}^{-3}$, temperature of 280 K, and relative humidity of 60 $\%$ as a function of the particle diameter.

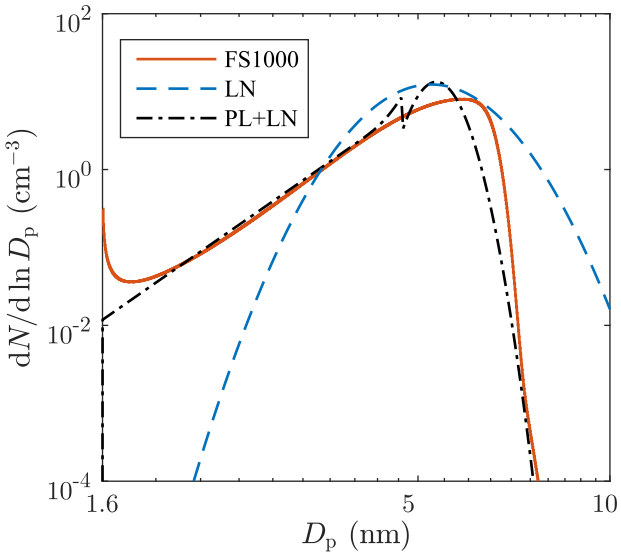

Figure 2. Particle size distribution modelled with size-dependent condensational growth rate using a very accurate fixed-sectional model (FS1000), the simple log-normal model (LN), and the combined power law and log-normal distribution model (PL+LN).

3. As stated on page 16, lines 7-14, the size distribution observed in the chamber measurement is combined from data from three separate instruments, but there is no information to how they are combined. For example, the information from all the three instruments could be used simultaneously (e.g., Viskari et al., 2012) to provide the size distribution, but this seems unlikely based on Figure 4. Another option is that the raw data are inverted separately, which raises the question, how a $\mathrm{d}N/\mathrm{d}\log D_\mathrm{p}$ *values are calculated for PSM and CPC, which only measure total concentration above a given cut diameter? Without the information of how the observed distribution is obtained, one cannot properly evaluate the accuracy of the new model against those measurements, especially in the sizes below the range of SMPS measurements. A proper explanation of how the measured size distributions are obtained should be given.*

An explanation of how the data from different devices are combined is now added. The approximated cut diameters of the devices, $D_\mathrm{PSM} = 1.6\,\mathrm{nm}$, $D_\mathrm{CPC} = 3.6\,\mathrm{nm}$, and $D_\mathrm{Nano\text{-}SMPS} = 7\,\mathrm{nm}$, are used to combine the data of PSM, CPC, and Nano-SMPS to obtain total aerosol size distributions for the diameter range of 1.6 – 64 nm with

$$\left.\frac{\mathrm{d}N}{\mathrm{d}\ln D_\mathrm{p}}\right|_\mathrm{measured} = \begin{cases} \frac{\max\{N_\mathrm{PSM}-N_\mathrm{CPC},0\}}{\ln(D_\mathrm{CPC}/D_\mathrm{PSM})}, & D_\mathrm{PSM} \le D_\mathrm{p} < D_\mathrm{CPC} \\ \frac{\max\{N_\mathrm{CPC}-N_\mathrm{Nano\text{-}SMPS},0\}}{\ln(D_\mathrm{Nano\text{-}SMPS}/D_\mathrm{CPC})}, & D_\mathrm{CPC} \le D_\mathrm{p} < D_\mathrm{Nano\text{-}SMPS} \\ \left.\frac{\mathrm{d}N}{\mathrm{d}\ln D_\mathrm{p}}\right|_\mathrm{Nano\text{-}SMPS}, & D_\mathrm{p} \ge D_\mathrm{Nano\text{-}SMPS} \end{cases}, \quad (1)$$

where N_{PSM}, N_{CPC}, and $N_{\mathrm{Nano\text{-}SMPS}}$ are the total number concentrations measured by the devices, and $\left.\frac{\mathrm{d}N}{\mathrm{d}\ln D_{\mathrm{p}}}\right|_{\mathrm{Nano\text{-}SMPS}}$ is the particle size distribution measured by Nano-SMPS.

4. Beginning from page 13, line 6, until page 14, line 3, it is described how the particles are transferred from PL distribution to LN distribution due to condensational growth. Based on Figure 10, it seems that the value of D_2 is affected by the choice of γ, so this relation should be given explicitly. Furthermore, it is inconvenient for any practical use of the model that γ is a free parameter, but very little information is given as to how to choose that value for given conditions to be simulated. In the manuscript, only one example case is provided, which makes it difficult to assess if the optimal value of γ for that case can be generalized to other cases or not. For example, does the optimal value of γ depend on the particle growth rate or formation rate? In order to facilitate any future use of the model, the authors should provide some advice for choosing the value of γ, preferably with added examples of comparisons to measurements with different conditions.

The value of D_2 is affected by the choice of γ, but not with an explicit relation, because the value of D_2 is not a direct consequence of the value of γ. The value of γ affects on the amount of particles transferred from the PL distribution to the LN distribution, which affects on the value of D_2 through the transferred amount of the largest particles in the PL distribution.

Information on how to choose the value of the condensational transfer factor γ is now added. The value $\gamma = 0$ produces a distribution that will be mainly in a power law form; the value $\gamma = 1$ produces a log-normal distribution only. To choose a suitable value for γ for a simulation, the user should consider how well does the aerosol formation event follow the approximations of the theory described in the manuscript. The value 0 is suitable only when the aerosol processes follow the theory exactly. To simulate a realistic particle formation event, the value has to be increased towards unity using the following guidelines. The more the following conditions are met, the higher γ should be used: (1) particle formation or growth are multicomponent processes, (2) the particle formation rate or the condensation growth rate vary significantly with time, (3) the condensational growth rate varies significantly with the particle size, (4) the background aerosol acting as a coagulation sink does not remain in a nearly constant state during the time domain of the simulation, (5) particle sizes in the background aerosol are not significantly higher than in the PL+LN distribution, (6) the depositional losses cannot be approximated with as simple form as described in the manuscript, e.g., in the case of complex geometry or turbulent flow. In real atmospheric particle formation events, γ should rarely has the value of less than 0.5, which can also be used as an initial guess if figuring the previous guidelines is problematic. If the shapes of the distributions to be modelled are initially known, the value of γ can be adjusted to obtain a proper model output, e.g., in the case of inverse modelling. The factor γ can also be considered a time-dependent function, but in the manuscript we concentrate only to constant values of γ.

5. Page 1, lines 12-16: the first paragraph of the manuscript feels like a few bullet points collected to give some background, and then the rest of the introduction deals with various approaches to modeling particle size distribution. It would serve the reader to have a little longer and more coherent description of the framework and motivation of modelling size distributions.

Introduction is now extended to contain description about the modelling of size distributions.

6. Page 5, line 27: Is the intramodal coagulation really the only process initiating the formation of the LN distribution, or can the condensational transfer initiate it also? According to Eq. (50) the amount of condensational transfer does not depend on the LN distribution, or on the existence of one. Furthermore, on page 17, line 10, it is stated that the coagulational transfer was neglected when simulating conditions of chamber experiment, but LN distribution is still seen in the results. This needs to be clarified.

The original sentence "The intramodal coagulation of the PL distribution remains the only process initiating the formation the LN distribution" was lacking an important part "if the condensational transfer is neglected" which is now added. It is true that both the coagulational transfer and the condensational transfer can alone initiate the LN distribution and these processes do not require the existence of the LN distribution.

7. Page 7, lines 5-11: Does this part have something to do with the current work? As far as I understand, the growth rate is used as an input value in the model in all of the simulations, and the condensation process is not really simulated. If this paragraph is important, then it should be made clear why, and if not, it would clarify the article to remove it.

The part, in which the condensation term is expressed using the properties and concentrations of the vapors participating in the growth process, is now relevant in the manuscript because the condensation process is now simulated in the case with size-dependent growth rate. Therefore, it is not removed from the manuscript.

8. Page 7, lines 12-14: It is unclear why the parameters in Eq. (16) need to be considered to vary with t and D_p for the mass growth rate to vary with t and D_p. According to Eq. (16), the mass growth rate depends explicitly on D_p, and if any term depends on t, then the mass growth rate should depend on both t and D_p.

The meaning of the sentence should have been that the parameters in Eq. (16) need to be considered to vary with t and D_p only, not with the spatial location. Thus, if the parameters do not vary with the spatial location, the mass growth rate will vary neither. The sentence is now clarified.

9. Page 7, lines 23-25: I do not understand why the new particle formation rate is in this sentence, please clarify.

There was nothing to do with the new particle formation rate in that sentence and it is now removed.

10. Page 10, lines 18-20: It is stated that the degrees of quadratures are low, but it would serve the reader to provide some examples, how much the simulation results would change due to lower or higher degree of the quadratures used in the model.

The effect of the degrees of the quadratures are now examined more thoroughly. Quadratures are now used also with the condensation term because it cannot be calculated analytically with a size-dependent growth rate. The examination of the quadrature developed here revealed that it should be used only when $\alpha > 0.5$, in the case of condensation, and when $D_2/D_1 < 3$, in the case of coagulation. In those regions, the absolute relative errors of the terms are less than 10^{-2} when calculated with the quadrature. In the remaining regions, numerical integration is used. The equation for the numerical integration is now added. The computing time associated in calculating the condensation term is 1 or 2 orders shorter with the quadrature compared to numerical integration. The degree of 5 used with the Hermite-Gauss quadrature provides the absolute relative errors of the terms less than 10^{-4}.

11. Page 14, line 16: It is stated that the diameter of newly-formed particles was assumed to be 1.6 nm. Would the results and/or conclusions change with another choice of this diameter? If so, it should be presented, and if not, then that should be mentioned.

The choice of D_1 does not affect on the results of the test cases and not on the examination of the accuracy and the computational cost of the model using the chamber event simulation, because sectional models have the diameter of newly-formed particles too. However, it has an effect in inverse modelling because it determines the sizes of the smallest particles. The smaller the particles are the higher their losses are; therefore, lower values of D_1 result in small particles with high losses, and higher new particle formation rate is needed to obtain the measured concentrations. Approximately $40\,\%$ higher values for J is needed if $D_1 = 1\,\mathrm{nm}$ is used compared to $D_1 = 3\,\mathrm{nm}$, in the chamber event simulation.

12. Page 15, lines 22-23: What is the reason for only considering coagulational transfer, but not condensational transfer?

Because the test cases are purely theoretical, the need of constructing log-normal features to the distributions through the condensational transfer artificially is minimal. This sentence is now added to the manuscript.

13. Page 16, lines 13-14: It would serve the reader to explain with a few words how the EEPS and ELPI+ are used to ensure the stability of the aerosol distribution.

EEPS and ELPI+ having time resolutions of only $1\,\mathrm{s}$ were used to ensure the stability of the aerosol distribution during a Nano-SMPS scan lasting $150\,\mathrm{s}$: no rapid changes in the aerosol distribution were observed in the time scales shorter than $150\,\mathrm{s}$. This sentence is now added to the manuscript.

14. Page 16, lines 28-30: The PL+LN model was used to estimate $J(t)$ and $g(t)$ via inverse modelling, before those estimates were fine-tuned with FS model. Comparison of the best estimates of J and g from inverse modelling using both the PL+NL and FS models would be an excellent way to demonstrate the capability of the new model. Adding such comparison would increase the practical use of the manuscript. Performing such comparison manually might not be the most robust approach, though.

Inverse modelling is now done using the PL+LN, the LN, the FS400, and the MC100 models. Figures 3 and 4 show the time series of $J(t)$ and $g(t)$ obtained using different models. It can be seen that there are no significant differences between the time series obtained using the PL+LN model compared to the highly accurate models. Therefore, the PL+LN model is capable in inverse modelling.

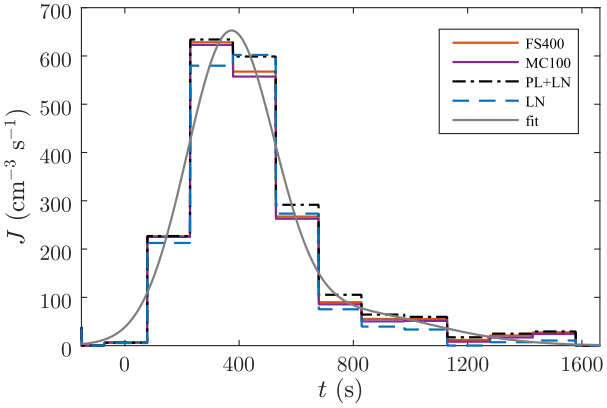

Figure 3. Time series for the new particle formation rates in the chamber event that produce the measured concentrations, N, S, and M, the most accurately compared to the measured ones, using different models. The fit denotes a bell-shaped function fitted to the values from the FS400 model.

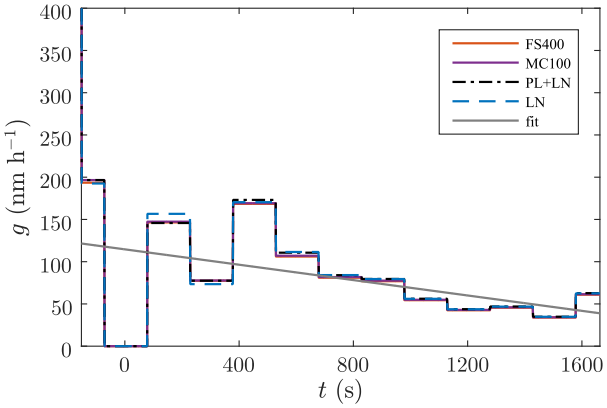

Figure 4. Time series for the condensational growth rates in the chamber event that produce the measured concentrations, N, S, and M, the most accurately compared to the measured ones, using different models. The fit denotes a linear function fitted to the values from the FS400 model.

15. Page 17, line 15: Only the distributions at the end of the simulations are shown, but it would serve the reader to also provide an example in which the distributions from the PL+NL model and FS1000 model would be compared at other times. This could be done, for example, by showing a surface plot of the relative difference between the two as a function of time and diameter. Such plot would make it possible to evaluate the accuracy of the PL+NL model at all particle sizes and stages of a new particle formation event, instead of just the end distribution.

The relative errors of the moments are now presented as time series (Fig. 5). A surface plot of the relative errors does not work well with particle size distributions because they have values in several different orders of magnitude. Therefore, particle size distributions of the test cases are now presented at every time moment using a video supplement.

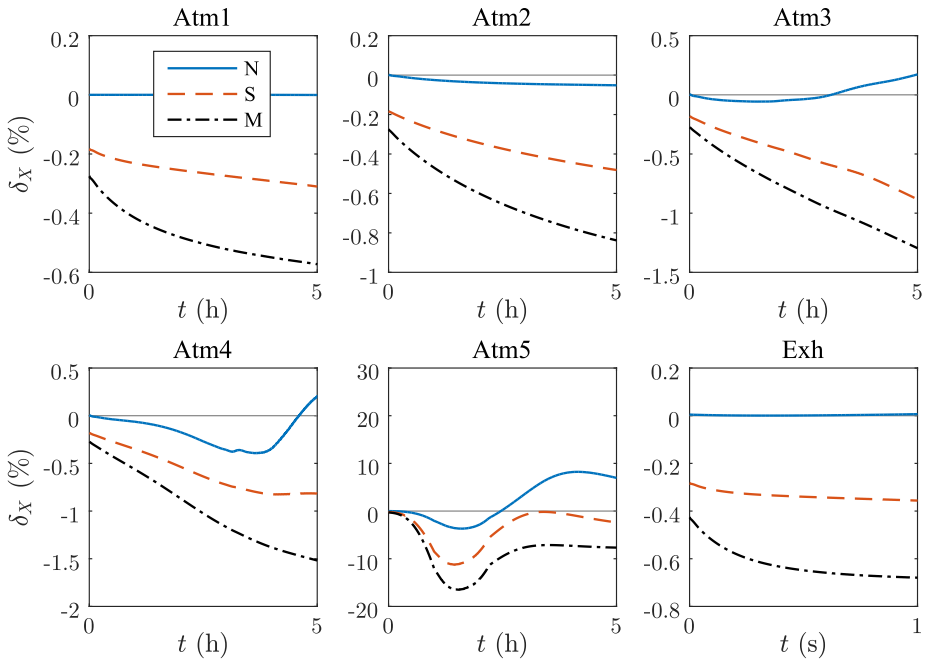

Figure 5. The relative errors of the moments (δ_X) in the test cases produced by the PL+LN model.

16. Page 18, lines 31-32: Even if the resolution of the measured distribution is poor below the size- range of the Nano-SMPS measurement, the measured GMD and GSD values would provide a valuable comparison to those from the simulations, especially towards the end of the time domain. I suggest showing also the measured GMD and GSD values in Figures 8 and 9, respectively.

The measured GMD and GSD are now shown in a figure.

17. Page 19, lines 1-6: This paragraph is a little confusing. I understand that the inverse modelling using the most accurate model produces the best estimates for the $J(t)$ and $g(t)$ representing the actual measurement conditions, and those values are then used as input in the other models, instead of some other values of $J(t)$ and $g(t)$ that would produce better correspondence between those simulation results and measurements. Choosing against what these simulation results are compared to, however, depends on the motivation of the comparison: If the point of interest is, how similar are the distributions simulated with a simple model and a more accurate model, when the same $J(t)$ and $g(t)$ values are used as input in both models, then the distributions from those models should be compared against each other. On the other hand, if the point of interest is, how well does the simple model reproduce the measured size distribution, when the best estimates for $J(t)$ and $g(t)$ representing the measurement conditions are used as input in the model, then the comparison should be against the measurement data, not

the accurate model. The authors should revise the paragraph and make it clear what they want to say with it.

The whole paragraph is now removed and the same message is said in different form in different part of the text because there is now an own section for inverse modelling.

Technical corrections:

1. Page 1, line 4: the word "validate" refers to something being labeled as valid, which is not really a proper metric in case of an aerosol dynamics model. I would suggest changing it to "evaluate" here and on other instances the word "validate" is used.

All validations are now replaced with evaluations.

2. Page 1, line 22: D_p and t are used, but they have not been defined yet.

D_p and t are now moved to a later point, where they are also defined.

3. Page 2, line 1: there should be a comma on both sides of "e.g.". This issue occurs repeatedly in the manuscript.

Commas to both sides of all occurrences of "e.g." are now added.

4. Page 2, line 4: should read "in which" instead of "of which".

It is corrected now.

5. Page 2, line 5: consider changing "changed" to "are allowed to vary".

It is changed now.

6. Page 2, line 5: One should avoid starting a sentence with "however" when the meaning is "nevertheless". The same issue occurs repeatedly in the manuscript.

All occurrences of "however" are now checked and replaced with "nevertheless" when relevant.

7. Page 2, line 10: it is unclear what "too" means in this context.

"due to the requirement of storing the center values of the sections too" is now replaced with "due to the requirement of storing also the center values of the sections".

8. Page 2, line 14: consider changing to "...the effect of numerical diffusion to their results is unknown.".

It is corrected now.

9. Page 4, line 2: consider using a comma on both sides of the defined variables.

It is corrected now.

10. Page 4, line 13: there should be a comma on both sides of "i.e.". This issue occurs repeatedly in the manuscript.

Commas to both sides of all occurrences of "i.e." are now added.

11. Page 5, line 15: consider changing "represents" to "presents".

It is corrected now.

12. Page 6, line 11: consider changing to "where terms on the right hand side denote...".

It is corrected now.

13. Page 7, line 2: it would serve the reader to clarify that "i" is just a shorthand notation for either PL or LN.

It is clarified now.

14. Page 7, line 5: variables longer than a single letter should not be in italics, "Kn". This error occurs multiple times in the manuscript.

All occurrences of "Kn" are now changed to roman font.

15. Page 7, line 6: add "where" to the beginning of the line.

It is added now.

16. Page 7, line 21: the word "latter" is confusing in the case of more than two items.

The word "latter" is now replaced with "last".

17. Page 14, line 15: the FS models are referred to in plural while only a single model was mentioned earlier in the paragraph, please clarify.

It is clarified now.

18. Page 16, line 1: the "254 nm" is probably the UV wavelength, but it should be made clear.

It is clarified now.

19. Page 16, lines 30-32: please revise the sentence, it is grammatically incorrect.

Trial and error method is now cancelled; therefore, the sentence does not exist in the manuscript any more.

20. Page 16, line 33, until page 17, line 1: This sentence is grammatically incorrect, and also somewhat ambiguous about how the deposition coefficient was obtained, which needs to made clear.

It is clarified now.

21. Page 17, line 16: should read "equal to".

It is corrected now.

22. Page 17, line 18: should read "the highest".

It is corrected now.

23. Page 17, lines 24-25: I eventually understood it, but this sentence is quite confusing, consider revising.

It is clarified now.

24. Page 18, line 15: consider changing "represents" to "presents".

It is corrected now.

25. Page 18, lines 28-30: I understand the message, but the sentence is poorly worded, consider revising the sentence.

The sentence is now revised.

26. Page 19, line 7: consider changing "represents" to "presents".

It is corrected now.

27. Page 19, lines 8-9: consider changing to "Conversely, using a high value of γ produces a more log-normal like form..."

It is revised now.

28. Page 19, lines 21-22: "...obtaining input parameters as the model output through inverse modelling" is quite unintuitive way of saying "... using inverse modelling to obtain the best estimates for parameters used as input in the model". Consider revising.

It is revised now.

29. Page 19, line 31: The word "conservation" is misleading in this context, as it is commonly used to describe what parameters are conserved in a model, instead of how similar certain parameter values in results from different models are.

The word "conservation" is now replaced with "accuracy".

30. Page 20, line 8: Saying "simple log-normal distribution model output GMD relatively well" seems to imply that there were rarely any issues with getting the GMD value from the model. Consider revising.

The GMD values were obtained well using the LN model in this case, and "in this case" is now added to the end of the sentence.

31. Page 23, Table 1: The value of the deposition coefficient is given in nm/s in the text, but in nm/h or nm/s in the table. Using nms^{-1} consistently is advised.

The units of the deposition coefficient are now changed consistently to $\mathrm{nm\,h^{-1}}$. However, in the case of the test case with the parameters reflecting vehicle exhaust, the units are $\mathrm{nm\,s^{-1}}$ due to the time scale of seconds instead of hours.

32. Page 24, Table 3: The first sentence "Computational costs and relative errors of different models using the chamber data." is problematic as the table shows errors in certain model outputs, not in the models themselves, and, furthermore, no chamber data per se was used in the simulations, only some input values representing the conditions of the chamber experiment.

It is now clarified that the relative errors in the table represent the values at the end of the simulation, and "chamber data" is replaced with "chamber simulation".

33. Page 25, Figure 1: The y-label refers to size distribution as "$\mathrm{d}N/\mathrm{d}\log D_\mathrm{p}$", while "$\mathrm{d}N/\mathrm{d}\ln D_\mathrm{p}$" is used in the equations. Consistent notation is suggested to avoid confusion.

All size distributions in the text and in the figures are now expressed with "$\mathrm{d}N/\mathrm{d}\ln D_\mathrm{p}$".

34. Page 30, Figure 6: It is often a good practice to provide ticks for the minimum and maximum values of both the x- and y-axis in figures, as it facilitates more accurate comparison to the presented values. In this case, for example, the reader might want to reproduce the model described in this manuscript, and then compare the results from that model to results presented in the manuscript using the same input values.

The minimum and maximum values of the both axes are now shown in figures, with the exception of some time axes, because they would disrupt with the time ticks of $0\,\mathrm{s}$ that should be visible because it is the time of switching the UV lights on.

35. Page 31, Figure 7, caption: It should read "...after the UV lights were switched on...".

It is corrected now

References

Kuang, C., Chen, M., Zhao, J., Smith, J., McMurry, P. H., and Wang, J.: Size and time-resolved growth rate measurements of 1 to 5 nm freshly formed atmospheric nuclei, Atmos. Chem. Phys., 12, 3573-3589, doi:10.5194/acp-12-3573-2012, 2012.

Viskari, T., Asmi, E., Virkkula, A., Kolmonen, P., Petäjä, T., and Järvinen, H.: Estimation of aerosol particle number distribution with Kalman Filtering – Part 2: Simultaneous use of DMPS, APS and nephelometer measurements, Atmos. Chem. Phys., 12, 11781-11793, doi:10.5194/acp-12- 11781-2012, 2012.

Referee 2 comments:

Review of Olin et al.

The authors present a new moment-type method for simulating aerosol microphysics, in which the size distribution is assumed a sum of a power-law part for the smallest particles and a lognormal part for larger ones. The performance is tested against a high resolution sectional model, and additionally compared with low resolution sectional methods as well as a pure lognormal method. The topic is in the scope of ACP but some more work is needed before publication.

In my view there are two major (and necessary!) issues to work on a bit more:

1. The new method is tested only in 0-D. For direct 0-D simulations we do not need faster methods - even PC:s can handle as many sections as are needed for very good accuracy. However, as the authors state in the conclusions, page 19, lines 19-23: "The PL+LN model is useful in simulations involving the initial steps of aerosol formation where a sectional representation of the size distribution causes too high computational cost, such as in multidimensional simulations or in the case of obtaining input parameters as the model output through inverse modelling." I suggest that the authors show the usefulness of their method in either of these cases: a spatially multidimensional system or an inverse modelling case! The authors have already done some inverse modelling with the method, however it was mentioned to be simple trial and error and not many details of this work were shown. E.g. applying the method with some automatic 'fitting' routine to search for some unknown parameters (such as nucleation rate, condensable vapour concentration or growth rate) would be much more impresssive.

Implementing the present code into a spatially multidimensional model would require significant additional work that we feel is outside of the scope of this manuscript. Inverse modelling is now performed automatically using also the PL+LN model for the mobile chamber particle formation event as mentioned earlier with the referee 1 comments.

2. The role of the fitting parameter γ is a little bit troublesome. The authors show that their choice of γ produces very nice results in the chosen example case. How about other systems? Is a high resolution sectional method always needed to complement the new method? And what about spatially multi-dimensional cases or inverse modelling? Will a single value work in a spatially multidimensional simulation with varying conditions? And, will results of inverse modelling be sensitive to the choice of γ? Some more advice to the readers/model users would be very valuable! In addition, I would very much like to see figure 4

also for other selections for γ.

Guidelines to choose a suitable value for γ are now added to the manuscript. In the case of figuring the guidelines is problematic, the value of 0.5 is recommended to use. Therefore, a high resolution sectional method is not needed at all to complement the PL+LN model. In spatially multidimensional cases and with inverse modelling, γ can be considered a spatially varying variable or time-dependent function, but due to the lack of the theory behind the value of γ, we concentrate only to constant values. The choice of the value for γ is also examined with inverse modelling: the values between 0.4 and 0.9 have only minor effect on the results. The contour plots with different values for γ are now added also.

Minor comments:

3. Page 1, line 17: Why is the sectional method called 'shape-preserving'? In my view, e.g. lognormal models are shape-preserving and in contrast, sectional methods allow the shape to evolve according to the dynamics.

That is true, "shape-preserving" is not the correct word for this purpose. The sentence is now replaced with "Methods that model a particle size distribution the most realistically are sectional methods".

4. Page 2, lines 3-4: In addition to moving centre method, similar so-called two-moment methods suffer also from less numerical diffusion than 'regular' fixed sectional methods (e.g. Adams and Seinfeld, JGR 107, D19).

The TOMAS model is now mentioned in the manuscript.

5. Is equation 1 correct? Shouldn't there be ΔD_{j-1} in the denominator of the first term on the right hand side of the lower equation?

That is true. It is corrected now.

6. Page 5, line 30: The lognormal features can arise also because of intramodal coagulation, resulting in a self-preserving distribution that resembles lognormal shape. (Friedlander, Smoke Dust and Haze)

This information is now included in the revised sentence.

7. Pages 9-10, gaussian quadratures: Such details of numerical integration would be more suitable in an Appendix?

The details of the Gaussian quadratures are now moved to Appendix.

8. Page 16, lines 8-14: Please explain in detail how the size distributions of the different instruments are combined.

The explanation is now added as mentioned earlier with the referee 1 comments.

9. Page 16, line 15: 'diameters around 15 nm' is very vague.

"particle diameters around 15 nm" is now replaced with "CMD of 15 nm".

10. Page 17, line 15: To get a nice result as in figure 6, is the LN distribution needed at all? If not, then it is no wonder that the LN result is much worse than the PL (which is in accordance with theory)?

The LN distribution is not needed in those cases to achieve as accurate results for the variables (the number, the surface area, and the mass concentrations, GMD, and GSD) as with both the PL and the LN distribution, but by visual inspection, the LN distribution is needed to obtain distributions that have the correct shapes in the highest particle sizes. This information is now added to the manuscript. It is in accordance with theory that the distribution will be in a purely power law form if coagulation is totally neglected, J and g are constants, and particle losses are modelled with the equations used in the manuscript. In that case, the LN distribution is not needed at all. However, by including coagulation and modelling other processes with more complex equations, the need for the LN distribution rises.

Using a combined power law and log-normal distribution model to simulate particle formation and growth in a mobile aerosol chamber

M. Olin, T. Anttila, and M. Dal Maso

Aerosol Physics Laboratory, Department of Physics, Tampere University of Technology, P.O. Box 692, 33101 Tampere, Finland

Correspondence to: M. Olin (miska.olin@tut.fi)

Abstract. We present the combined power law and log-normal distribution (PL+LN) model, a computationally efficient model to be used in simulations where the particle size distribution cannot be accurately represented by log-normal distributions, such as in simulations involving the initial steps of aerosol formation, where new particle formation and growth occur simultaneously, or in the case of inverse modelling. The model was ~~validated~~ evaluated against highly accurate sectional models using input parameter values that reflect conditions typical to particle formation occurring in the atmosphere and in vehicle exhaust, and tested in the simulation of a particle formation event performed in a mobile aerosol chamber at Mäkelänkatu street canyon measurement site in Helsinki, Finland. The number, surface area, and mass concentrations in the chamber simulation were conserved with the relative errors lower than 2 % using the PL+LN model, whereas a moment-based log-normal model and sectional models with the same computing time as with the PL+LN model caused relative errors up to ~~10~~17 % and ~~135~~79 %, respectively.

1 Introduction

Particle size distribution is the most important characteristic of ~~aerosols~~nanoparticles, as it controls ~~aerosol~~ their deposition to the human respiratory system~~and~~ , their behavior in the atmosphere~~. To accurately simulate aerosol evolution, the particle sizedistribution needs to be modelled carefully because particle size also strongly affects~~ , and the properties of engineered nanoparticles. The rates of several aerosol processes, such as condensation, coagulation, and deposition, are affected by particle size; thus, the particle size distribution controls also the evolution of the aerosol. While the rates of ~~several aerosol processes , such as condensation, coagulation, and deposition. Aerosol~~ the aerosol processes depend on the particle size, different particles within a particle size mode have different rates of aerosol processes and, thus, they evolve with different rates. This causes also the shape of the size distribution to evolve. Because particle size distributions usually contain particles with the diameters of several orders of magnitude rather than being monodisperse, i.e., equally sized, an accurate representation of aerosol properties and evolution requires that particle sizes are expressed as distributions. Due to a high count of particles with different sizes, shapes, and compositions within a volume of interest, computational costs to model them separately are extremely too high. Therefore, aerosol models typically model one or more parameter of the size distribution, such as particle number or mass

concentration of the total particle size range or of several size ranges separately. Simplifications made for size distributions in aerosol models cause unrealistic shapes for the distributions.

~~The most accurate shape-preserving methods to~~ Methods that model a particle size distribution the most realistically are sectional methods, in which the size distribution is split into separate size sections. The accuracy of a sectional model can be controlled by the number of the size sections. Increasing the number of sections increases accuracy, but the computational cost is also increased. In multidimensional simulations, such as in Computational Fluid Dynamics (CFD) and in climate simulations, computational efficiency is a key property of the model. Simulations involving inverse modelling (Verheggen and Mozurkewich, 2006), where the values of model input parameters (e.g., new particle formation rate ~~J~~ or condensational growth rate~~$g = \frac{\mathrm{d}D_\mathrm{p}}{\mathrm{d}t}$~~) are varied systematically to find out the values that most exactly produce the measured results, may suffer from long computing times even in one-dimensional cases.

Sectional methods vary depending on the conserved property of the aerosol. Only a single property, e.g., particle number, particle surface area, or particle mass concentration, can be conserved in the simulation but other properties will suffer from numerical diffusion, which is seen as the overestimation of the non-conserved properties (Wu and Biswas, 1998). Less numerical diffusion can be obtained, e.g., by using a moving-center fixed-sectional method, ~~of~~ in which size sections have fixed boundaries but the centers of the sections are ~~changed~~ allowed to vary so that number and mass concentrations are conserved better(Jacobson, 1997). However, implementing the moving-center fixed-sectional method in Eulerian simulation, such as in CFD simulation, with simultaneous new particle formation, condensation, coagulation, and transportation is challenging due to discontinuous behavior of the section variables (all particles of a section are transferred to an adjacent section when the center of a section exceeds a section boundary during growth), computationally time-consuming due to the transfer of the particles between the sections, and memory-consuming due to the requirement of storing also the center values of the sections~~too~~. Wang and Zhang (2012) have modelled simultaneous new particle formation and growth within diesel exhaust plumes using the moving-center fixed-sectional method in ~~three dimensional~~ three-dimensional CFD simulation and have obtained promising results for particle size distributions compared to the measured distributions with only 8 size sections in a particle diameter decade. However, they did not report comparison between their model and any highly accurate aerosol model; thus, the ~~amount~~ effect of numerical diffusion to their results is unknown. Another method to decrease numerical diffusion is the TwO-Moment Aerosol Sectional (TOMAS) model, in which both the number and the mass concentrations are stored for all size sections (Adams and Seinfeld, 2002) . The TOMAS model provides conservation for both the number and the mass concentrations of the total distribution, but the memory consumption in multidimensional simulations can be too high due to a high number of variables to be stored in every computational cell.

Other approaches to model the particle size distribution are methods based on the moments of the distribution (Whitby and McMurry, 1997), which are both computationally efficient (Mitrakos et al., 2007) and have continuous behavior of the variables. The number of the conserved properties of the aerosol is controlled by the number of the modelled moments; e.g., conserving number, surface area, and mass concentrations can be obtained by modelling the corresponding three moments. The number of the variables being stored during the simulation is the number of the modelled moments, which is significantly less compared to sectional methods, in which the number of the variables can be several hundreds. The major drawback in the

methods based on moments is that the size distribution needs to be presented with a pre-defined function, unless the quadrature-method of moments (QMOM, McGraw (1997)) is used. QMOM provides accurate results (Barrett and Webb, 1998) but the reconstruction of the distribution parameters from the moments is not unique (Mitrakos et al., 2007). The typical choice for the size distribution function is the log-normal distribution or the combination of several log-normal distributions. They correspond well with many laboratory aerosols and aged aerosols, but during the initial steps of the formation and growth of aerosol the size distribution can differ significantly. For example, Tammet and Kulmala (2014) recommend two-power law for the size distribution of atmospheric aerosols measured at least in Northern Europe. Two-power law distribution has four parameters, which implies that four moments are required for the reconstruction of the parameters from the moments, if the distribution is modelled using the moment method. However, there is no analytical solution for the system of equations of the two-power law approach, and solving the system of equations with four variables numerically is computationally very expensive.

The general dynamic equation (GDE) for the number concentration of a size section ~~N_j~~ j, with new particle formation ~~rate $J(t)$~~ and condensational growth ~~rate $g(t, D_\mathrm{p})$~~ without any other aerosol processes, is (Seinfeld and Pandis, 2006)

$$\frac{\mathrm{d}N_j}{\mathrm{d}t} = \begin{cases} J(t) - \frac{g(t,D_\mathrm{p})}{\Delta D_j} N_j, & j = 1 \\ \frac{g(t,D_\mathrm{p})}{\Delta D_{j-1}} N_{j-1} - \frac{g(t,D_\mathrm{p})}{\Delta D_j} N_j, & j > 1 \end{cases}, \tag{1}$$

where N_j and ΔD_j ~~is~~ are the number concentration and the diameter width of the ~~section j~~size section, respectively. $J(t)$ is new particle formation rate as a function of time t, and $g(t, D_\mathrm{p})$ is condensational growth rate $\frac{\mathrm{d}D_\mathrm{p}}{\mathrm{d}t}$, where D_p is the particle diameter. In the case of simultaneous new particle formation and condensation with time- and size-independent rates, the analytical solution for the GDE provides the particle size distribution

$$\frac{\mathrm{d}N}{\mathrm{d}\ln D_\mathrm{p}} = \begin{cases} \frac{J}{g} D_\mathrm{p}, & D_1 \le D_\mathrm{p} \le D_2 \\ 0, & \text{otherwise} \end{cases}, \tag{2}$$

where D_1 is the diameter of the newly formed particle (assumed constant) and D_2 is the largest diameter. Equation (2) is in the form of a power law where the power of D_p is unity. In a realistic particle formation process, $J(t)$ and $g(t, D_\mathrm{p})$ do not remain constants and other aerosol processes affect also; thus, the power of D_p can differ and log-normal features will appear in the distribution. Here, we present a method to express the particle size distribution as a combination of a power law and a log-normal distribution. This moment-based combined power law and log-normal distribution model ~~is validated~~ was evaluated against highly accurate sectional models ~~and tested in the~~ using theoretical test cases and a real-world case, which represents a simulation of a particle formation event ~~performed~~ occurred in a mobile aerosol chamber.

2 Model description

The combined power law (PL) and log-normal (LN) distribution model (PL+LN) is based on the sum of these distributions. The PL distribution handles the formation and the initial growth of new particles; the LN distribution represents the log-normal shape of the distribution and it is formed by coagulation and condensation from the PL distribution.

2.1 Particle size distributions

2.1.1 Power law distribution

The formulation of the PL distribution originates from Eq. (2), where the power of D_p is allowed to vary,

$$\left.\frac{\mathrm{d}N}{\mathrm{d}\ln D_\mathrm{p}}\right|_\mathrm{PL} = \begin{cases} \frac{N_\mathrm{PL}\alpha}{D_2^\alpha - D_1^\alpha} D_\mathrm{p}^\alpha, & D_1 \le D_\mathrm{p} \le D_2, \alpha \neq 0 \\ \frac{N_\mathrm{PL}}{\ln(D_2/D_1)}, & D_1 \le D_\mathrm{p} \le D_2, \alpha = 0\,, \\ 0, & \text{otherwise} \end{cases} \tag{3}$$

where N_PL is the total particle number concentration, α is the slope parameter, D_1 is the smallest diameter, and D_2 is the largest diameter of the PL distribution. In this form, the PL distribution has four parameters, which leads to numerical challenges for the reconstruction of the distribution parameters from four moments. ~~However~~Nevertheless, by fixing one parameter, only three moments are required to be modelled and the reconstruction will simplify. Here, the value of D_1 is fixed to the diameter of a newly formed particle, which is also physically sensible because that value is not expected to vary significantly; in atmospheric particle formation, the value is about ~~1.5 ± 0.3 nm~~ $1.5 \pm 0.3\,\mathrm{nm}$ (Kulmala et al., 2013).

Three moments required in the modelling of the PL distribution with parameters N_PL, α, and D_2 are, in this article, number, N_PL, surface area, S_PL, and mass, M_PL~~concentration~~, concentrations,

$$N_\mathrm{PL} = N_\mathrm{PL} \tag{4}$$

$$\begin{aligned} S_\mathrm{PL} &= \int_{-\infty}^{\infty} s_\mathrm{p} \left.\frac{\mathrm{d}N}{\mathrm{d}\ln D_\mathrm{p}}\right|_\mathrm{PL} \mathrm{d}\ln D_\mathrm{p} \\ &= s_1 N_\mathrm{PL} \frac{\alpha}{\alpha+2} \frac{\left(\frac{D_2}{D_1}\right)^{\alpha+2} - 1}{\left(\frac{D_2}{D_1}\right)^{\alpha} - 1} \end{aligned} \tag{5}$$

$$\begin{aligned} M_\mathrm{PL} &= \int_{-\infty}^{\infty} m_\mathrm{p} \left.\frac{\mathrm{d}N}{\mathrm{d}\ln D_\mathrm{p}}\right|_\mathrm{PL} \mathrm{d}\ln D_\mathrm{p} \\ &= m_1 N_\mathrm{PL} \frac{\alpha}{\alpha+3} \frac{\left(\frac{D_2}{D_1}\right)^{\alpha+3} - 1}{\left(\frac{D_2}{D_1}\right)^{\alpha} - 1}, \end{aligned} \tag{6}$$

where s_p and m_p are the surface area and the mass of a particle, respectively, and s_1 and m_1 are the surface area and the mass of a newly formed particle, respectively. All particles are assumed to be spherical. Equations (5) and (6) have singularities at α values of -3, -2, and 0. In those cases, the equations have different formulations, and from now on, the singularity equations are not shown here due to the fact that α will never equal a singularity value precisely in a simulation. ~~Modelling~~ To model the composition of particles can be done by separating the mass concentration to different components using the assumption that the particles are internally mixed, i.e., the composition does not vary with ~~the~~ particle diameter. ~~The modelling~~ Modelling of the particle composition is, however, outside of the scope of this article.

The reconstruction of the distribution parameters from the moments N_{PL}, S_{PL}, and M_{PL} is performed as follows. The zeroth moment N_{PL} is already one of the distribution parameters, but S_{PL} and M_{PL} are not. The latter are converted to the system of equations of two unknown variables α and $d = D_2/D_1$

$$\begin{cases} \frac{M_{\mathrm{PL}}}{N_{\mathrm{PL}}}\frac{1}{m_1} &= \left(\frac{\alpha}{\alpha+3}\right)\left(\frac{d^{\alpha+3}-1}{d^{\alpha}-1}\right) \\ \frac{M_{\mathrm{PL}}}{S_{\mathrm{PL}}}\frac{s_1}{m_1} &= \left(\frac{\alpha+2}{\alpha+3}\right)\left(\frac{d^{\alpha+3}-1}{d^{\alpha+2}-1}\right) \end{cases}. \tag{7}$$

However, there is no analytical solution for this system of equations, but solving two variables numerically is sufficiently fast for this purpose. A pre-calculated interpolation table is used in the numerical solution, with which a more rapid calculation is obtained. The interpolation table increases the memory cost of the model, but as the table is unique (independent on temporal or spatial coordinate) it needs to be stored in one memory location only.

2.1.2 Log-normal distribution

The LN distribution is expressed by the equation

$$\left.\frac{\mathrm{d}N}{\mathrm{d}\ln D_{\mathrm{p}}}\right|_{\mathrm{LN}} = \frac{N_{\mathrm{LN}}}{\sqrt{2\pi}\ln\sigma}\exp\left[-\frac{\ln^2(D_{\mathrm{p}}/D_{\mathrm{g}})}{2\ln^2\sigma}\right], \tag{8}$$

where N_{LN} is the total particle number concentration, σ the geometric standard deviation, and D_{g} the geometric mean diameter of the LN distribution. The LN distribution is also modelled as three moments, N_{LN}, S_{LN}, and M_{LN}. Following the method of Whitby and McMurry (1997), the reconstruction of the distribution parameters from the moments can be performed using the equations

$$N_{\mathrm{LN}} = N_{\mathrm{LN}} \tag{9}$$

$$D_{\mathrm{g}} = 6^{-2/3}\pi^{-5/6}\rho^{2/3}N_{\mathrm{LN}}^{-5/6}S_{\mathrm{LN}}^{3/2}M_{\mathrm{LN}}^{-2/3} \tag{10}$$

$$\ln^2\sigma = \ln\left(6^{2/3}\pi^{1/3}\rho^{-2/3}N_{\mathrm{LN}}^{1/3}S_{\mathrm{LN}}^{-1}M_{\mathrm{LN}}^{2/3}\right), \tag{11}$$

where ρ is the particle density.

2.1.3 Connection between the distributions

The combined particle distribution is modelled as the superposition of the PL and the LN distributions

$$\left.\frac{\mathrm{d}N}{\mathrm{d}\ln D_{\mathrm{p}}}\right|_{\mathrm{PL+LN}} = \left.\frac{\mathrm{d}N}{\mathrm{d}\ln D_{\mathrm{p}}}\right|_{\mathrm{PL}} + \left.\frac{\mathrm{d}N}{\mathrm{d}\ln D_{\mathrm{p}}}\right|_{\mathrm{LN}}. \tag{12}$$

Figure 1 ~~represents~~ presents examples of the PL+LN distribution. PL distributions with different values of α are shown in the left pane; $N = 10^6\,\mathrm{cm}^{-3}$, $D_1 = 1.5\,\mathrm{nm}$, and $D_2 = 5\,\mathrm{nm}$ are equal in all four distributions. The right pane shows the PL distribution with values $N = 10^6\,\mathrm{cm}^{-3}$, $\alpha = 1$, $D_1 = 1.5\,\mathrm{nm}$, and $D_2 = 3\,\mathrm{nm}$, the LN distribution with values $N = 5\times 10^5\,\mathrm{cm}^{-3}$, $D_{\mathrm{g}} = 4\,\mathrm{nm}$, and $\sigma = 1.1$, and the combination of them.

A schematic presentation of the connections between the distributions is shown in Fig. 2. Particles in the PL distribution, formed by new particle formation and grown by condensation and coagulation (Fig. 3), are transferred to the LN distribution through three intermodal processes: coagulational transfer, intermodal coagulation, and condensational transfer. The coagulational transfer is accounted by intramodal coagulation, i.e., self-coagulation, which is basically an intramodal process, but in this model it is used to initiate the LN distribution by transferring the coalesced resultant particles larger than D_2 to the LN distribution. The coagulational transfer is described in more detail in Sec. 2.2.5. After the LN distribution is initiated, particles of the both distributions begin to collide intermodally (the intermodal coagulation). In that case, the resultant particles are always assigned to the LN distribution, which is thought to consist of larger particles than the PL distribution.

The ~~intramodal coagulation of the PL distribution~~ coagulational transfer remains the only process initiating the formation of the LN distribution if the condensational transfer is neglected. Therefore, in the case of low particle number concentration, i.e., low intramodal coagulation rate, the formation rate of the LN distribution is slow; thus, the combined distribution would be mainly in a power law form. However, in realistic particle formation events, log-normal features in the size distribution are widely observed (Hinds, 1999). This is due to the facts that the aerosol processes have normally time- and size-dependent ~~J, g, or particle loss rate caused by coagulation to background particles or deposition to walls~~rates and that the particles can be multicomponent, and due to the intramodal coagulation that eventually results in self-preserving log-normal distribution (Friedlander, 2000) . The model described here ~~does not connect~~ connects the formation of the LN distribution with the ~~latter processes~~intramodal coagulation only. Therefore, log-normal features can be generated artificially to the PL+LN distribution by transferring some of the particles from the PL distribution to the LN distribution. This transfer is calculated through condensation (the condensational transfer). Particles that are to be grown beyond the diameter D_2 are transferred to the LN distribution by the condensational transfer instead of keeping them in the PL distribution and increasing the value of D_2. The condensational transfer is described in more detail in Sec. 2.2.5.

2.2 Aerosol processes

The general dynamic equation for a particular moment X ($= N_{\mathrm{PL}}$, S_{PL}, M_{PL}, N_{LN}, S_{LN}, or M_{LN}) in a one-dimensional (temporal coordinate only) simulation is

$$\frac{\mathrm{d}X}{\mathrm{d}t} = \mathrm{npf}_X + \mathrm{cond}_X + \mathrm{coag}_X + \mathrm{loss}_X^{\mathrm{coag}} + \mathrm{loss}_X^{\mathrm{dep}} + \mathrm{transfer}_X^{\mathrm{coag}} + \mathrm{transfer}_X^{\mathrm{cond}}, \tag{13}$$

~~of which terms~~ where terms on the right hand side denote new particle formation, condensation, coagulation, coagulational losses, depositional losses, coagulational transfer, and condensational transfer, respectively. The formulation of the terms is described next.

2.2.1 New particle formation

New particle formation is modelled by a term

$$\mathrm{npf}_X = \begin{cases} J(t), & X = N_{\mathrm{PL}} \\ J(t)\, s_1, & X = S_{\mathrm{PL}} \\ J(t)\, m_1, & X = M_{\mathrm{PL}} \\ 0, & X = N_{\mathrm{LN}},\, S_{\mathrm{LN}}, \text{ or } M_{\mathrm{LN}} \end{cases}, \tag{14}$$

where $J(t)$ can be calculated, e.g., through any nucleation theory, in which $J(t)$ depend also on vapor concentrations and temperature, for example. However, finding the correct formulation for $J(t)$ is outside of the scope of this article; thus, we decided to use formation rate as an input parameter that can be either a constant~~(, J) ,~~ or a time-dependent function~~(, $J(t)$)~~. Additionally, inverse modelling is done to obtain $J(t)$ from measured particle number concentrations.

The sizes of a newly formed particle (D_1, s_1, and m_1) can be obtained from nucleation theories, but they are assumed to be constants here. In the case where $J(t)$ suddenly drops to zero but condensation still continues, concentration of particles with diameters around D_1 would subsequently decrease down to zero due to the growth of newly formed particles to larger diameters. Therefore, D_1, as a parameter of the PL distribution, should be a variable to model the distribution accurately. However, this would change the distribution back to a more complex four-parameter distribution that is outside of the scope of this article. In that case or with smoothly decreasing $J(t)$, α has a tendency to increase.

2.2.2 Condensation

Condensation rate [$\mathrm{kg\,m^{-3}s}$] of vapor v on a particle distribution~~i~~, PL or LN (denoted with i), can be modelled as (Olin et al., 2015)

$$\mathrm{cond}_{M_i} = \int_{-\infty}^{\infty} \frac{\mathrm{d}m_{\mathrm{p},v}}{\mathrm{d}t} \left.\frac{\mathrm{d}N}{\mathrm{d}\ln D_{\mathrm{p}}}\right|_i \mathrm{d}\ln D_{\mathrm{p}}, \tag{15}$$

where $\frac{\mathrm{d}m_{\mathrm{p},v}}{\mathrm{d}t}$ is the mass growth rate of a particle [$\mathrm{kg\,s^{-1}}$] due to vapor v ~~is (Lehtinen and Kulmala, 2003)~~ (Lehtinen and Kulmala, 2003) ,

$$\frac{\mathrm{d}m_{\mathrm{p},v}}{\mathrm{d}t} = 2\pi(D_{\mathrm{p}} + D_v)(\mathcal{D}_{\mathrm{p}} + \mathcal{D}_v)(C_{v,\infty} - C_{v,\mathrm{p}}) \frac{Kn+1}{0.377Kn + 1 + \frac{4}{3\phi}(Kn^2 + Kn)} \frac{\mathrm{Kn}+1}{0.377\mathrm{Kn} + 1 + \frac{4}{3\phi}(\mathrm{Kn}^2 + \mathrm{Kn})}, \tag{16}$$

where D_v is the diameter of a vapor molecule. $\mathcal{D}_{\mathrm{p}}$ and $\mathcal{D}_v$ are the diffusion coefficients of a particle and of a vapor molecule, respectively. $C_{v,\infty}$ and $C_{v,\mathrm{p}}$ are the mass concentration of the vapor in the far-field and over the particle surface, respectively. ~~ϕ and Kn are the~~ Kn and ϕ are the Knudsen number and the mass accommodation coefficient~~and the Knudsen number~~, respectively. The concentration $C_{v,\mathrm{p}}$ is

$$C_{v,\mathrm{p}} = \Gamma_v\, C_{v,\mathrm{sat}} \exp\left(\frac{4\mathcal{S}m_v}{k_{\mathrm{B}}T\rho D_{\mathrm{p}}}\right), \tag{17}$$

where Γ_v, $C_{v,\mathrm{sat}}$, and m_v are activity, the saturation concentration, and the molecule mass of the vapor, respectively, $\mathcal{S}$ is surface tension, k_B is the Boltzmann constant, and T is temperature.

In one-dimensional simulation, the mass growth rate can be considered a function of time and the particle diameter

$$\frac{\mathrm{d}m_{\mathrm{p},v}}{\mathrm{d}t} = \frac{\mathrm{d}m_{\mathrm{p},v}}{\mathrm{d}t}(t, D_\mathrm{p})$$

only, not of the spatial location, if the other parameters in Eq. (16) are considered also. Here, the mass growth rate (single-component case) is expressed using condensational growth rate $g(t, D_\mathrm{p})$

$$\frac{\mathrm{d}m_\mathrm{p}}{\mathrm{d}t}(t, D_\mathrm{p}) = \frac{\mathrm{d}m_\mathrm{p}}{\mathrm{d}D_\mathrm{p}} \cdot \frac{\mathrm{d}D_\mathrm{p}}{\mathrm{d}t}(t, D_\mathrm{p}) = \frac{\pi}{2}\rho D_\mathrm{p}^2 g(t, D_\mathrm{p}). \tag{18}$$

Hence, the condensation rate for a particle distribution becomes

$$\mathrm{cond}_{M_i} = \frac{\pi}{2}\rho \int_{-\infty}^{\infty} D_\mathrm{p}^2 g(t, D_\mathrm{p}) \left.\frac{\mathrm{d}N}{\mathrm{d}\ln D_\mathrm{p}}\right|_i \mathrm{d}\ln D_\mathrm{p}, \tag{19}$$

which has an analytical solution for ~~both distributions~~ the both distributions, PL and LN, when $g(t, D_\mathrm{p})$ can be expressed with a polynomial of D_p. The mass growth rate is proportional to D_p^2 if the following conditions are met: 1) the particle size is in free-molecular regime, 2) $D_p \gg D_v$, 3) $C_{v,\infty} \gg C_{v,\mathrm{p}}$. The ~~latter~~ last one applies when the particle size is large or when the vapor has low saturation vapor pressure. Since particle sizes near the molecular size are modelled in this article, only the first condition applies satisfactorily. ~~However, for the sake of convenience,~~ Nevertheless, this article concentrates mainly in cases where the mass growth rate is assumed to be proportional to D_p^2. ~~As for new particle formation rate $J(t)$, the~~ Additionally, a single test case, where the mass growth rate is calculated using Eqs. (16) – (17), is presented. The main point in this article is not to provide the correct formulation for $g(t, D_\mathrm{p})$, but to compare different models, and additionally to perform inverse modelling to obtain $g(t)$ from the time evolution of measured aerosol size distributions. Due to the assumption of the proportionality of the mass growth rate, the condensational growth rate becomes size-independent, and finally, the condensation terms used in Eq. (13) become

$$\mathrm{cond}_X = \begin{cases} 0, & X = N_i \\ 2\pi\, g(t) \int_{-\infty}^{\infty} D_\mathrm{p}\, \mathrm{d}N_i, & X = S_i \\ \frac{\pi}{2}\rho\, g(t) \int_{-\infty}^{\infty} D_\mathrm{p}^2\, \mathrm{d}N_i, & X = M_i \end{cases} \tag{20}$$

where $\mathrm{d}N_i$ is an abbreviation of

$$\left.\frac{\mathrm{d}N}{\mathrm{d}\ln D_\mathrm{p}}\right|_i \mathrm{d}\ln D_\mathrm{p}. \tag{21}$$

The analytical ~~solutions for Eqs~~solution for Eq. (20) ~~are~~ is

$$\mathrm{cond}_X = X\, g(t) \cdot \begin{cases} 0, & X = N_{\mathrm{PL}} \\ \frac{2}{D_1}\left(\frac{\alpha+2}{\alpha+1}\right)\left(\frac{d^{\alpha+1}-1}{d^{\alpha+2}-1}\right), & X = S_{\mathrm{PL}} \\ \frac{3}{D_1}\left(\frac{\alpha+3}{\alpha+2}\right)\left(\frac{d^{\alpha+2}-1}{d^{\alpha+3}-1}\right), & X = M_{\mathrm{PL}} \\ 0, & X = N_{\mathrm{LN}} \\ \frac{2}{D_{\mathrm{g}}}\exp\left(-\frac{3}{2}\ln^2\sigma\right), & X = S_{\mathrm{LN}} \\ \frac{3}{D_{\mathrm{g}}}\exp\left(-\frac{5}{2}\ln^2\sigma\right), & X = M_{\mathrm{LN}} \end{cases} \tag{22}$$

when α is not -3, -2, or -1.

When the mass growth rate is calculated from the vapor concentrations and the properties of the vapor and the particles using Eqs. (16) – (17), it rarely can be expressed with a polynomial of D_{p}, unless polynomial fits are done for the function. However, if the vapor concentrations or the other properties are allowed to vary during the simulation, fits for the mass growth rate function may become inconvenient. In that case, the integral in Eq. (19) cannot be solved analytically. Therefore, numerical integration is required, in which Eq. (19) is calculated in a form of

$$\mathrm{cond}_{M_i} = \frac{\pi}{2}\rho \sum_{j=1}^{n} D_j^2\, g(t, D_j)\, \left.\frac{\mathrm{d}N}{\mathrm{d}\ln D_{\mathrm{p}}}\right|_i \ln\frac{D_{j+1}}{D_j}, \tag{23}$$

where D_j is the particle diameter of the size section j used in numerical integration when the particle diameter range is split into n sections. Computational cost of numerical integration is, however, higher compared to analytical solution of the integrals. Therefore, Gaussian quadratures are used here to reduce the associated computing time; they provide the optimal particle diameters and their weights for efficient evaluation of the integrals. The details of the Gaussian quadratures are described in Appendix A.

2.2.3 Coagulation

Coagulation is modelled as intramodal coagulation within the PL distribution and within the LN distribution, and as intermodal coagulation from the PL distribution to the LN distribution. The coagulation terms derived from the equations of Whitby and

McMurry (1997) are

$$\mathrm{coag}_{N_{\mathrm{PL}}} = -\frac{1}{2}\int_{-\infty}^{\infty}\int_{-\infty}^{\infty}\beta(D_{\mathrm{p}},D'_{\mathrm{p}})\,\mathrm{d}N_{\mathrm{PL}}\,\mathrm{d}N'_{\mathrm{PL}} - \int_{-\infty}^{\infty}\int_{-\infty}^{\infty}\beta(D_{\mathrm{p}},D'_{\mathrm{p}})\,\mathrm{d}N_{\mathrm{PL}}\,\mathrm{d}N'_{\mathrm{LN}} \tag{24}$$

$$\mathrm{coag}_{S_{\mathrm{PL}}} = -\frac{1}{2}\int_{-\infty}^{\infty}\int_{-\infty}^{\infty}\left[2s_{\mathrm{p}} - \left(s_{\mathrm{p}}^{\frac{3}{2}} + s_{\mathrm{p}}'^{\frac{3}{2}}\right)^{\frac{2}{3}}\right]\beta(D_{\mathrm{p}},D'_{\mathrm{p}})\,\mathrm{d}N_{\mathrm{PL}}\,\mathrm{d}N'_{\mathrm{PL}} - \int_{-\infty}^{\infty}\int_{-\infty}^{\infty}s_{\mathrm{p}}\,\beta(D_{\mathrm{p}},D'_{\mathrm{p}})\,\mathrm{d}N_{\mathrm{PL}}\,\mathrm{d}N'_{\mathrm{LN}} \tag{25}$$

$$\mathrm{coag}_{M_{\mathrm{PL}}} = -\int_{-\infty}^{\infty}\int_{-\infty}^{\infty}m_{\mathrm{p}}\,\beta(D_{\mathrm{p}},D'_{\mathrm{p}})\,\mathrm{d}N_{\mathrm{PL}}\,\mathrm{d}N'_{\mathrm{LN}} \tag{26}$$

$$\mathrm{coag}_{N_{\mathrm{LN}}} = -\frac{1}{2}\int_{-\infty}^{\infty}\int_{-\infty}^{\infty}\beta(D_{\mathrm{p}},D'_{\mathrm{p}})\,\mathrm{d}N_{\mathrm{LN}}\,\mathrm{d}N'_{\mathrm{LN}} \tag{27}$$

$$\mathrm{coag}_{S_{\mathrm{LN}}} = -\frac{1}{2}\int_{-\infty}^{\infty}\int_{-\infty}^{\infty}\left[2s_{\mathrm{p}} - \left(s_{\mathrm{p}}^{\frac{3}{2}} + s_{\mathrm{p}}'^{\frac{3}{2}}\right)^{\frac{2}{3}}\right]\beta(D_{\mathrm{p}},D'_{\mathrm{p}})\,\mathrm{d}N_{\mathrm{LN}}\,\mathrm{d}N'_{\mathrm{LN}} + \int_{-\infty}^{\infty}\int_{-\infty}^{\infty}\left[\left(s_{\mathrm{p}}^{\frac{3}{2}} + s_{\mathrm{p}}'^{\frac{3}{2}}\right)^{\frac{2}{3}} - s'_{\mathrm{p}}\right]\beta(D_{\mathrm{p}},D'_{\mathrm{p}})\,\mathrm{d}N_{\mathrm{PL}}\,\mathrm{d}N'_{\mathrm{LN}} \tag{28}$$

$$\mathrm{coag}_{M_{\mathrm{LN}}} = \int_{-\infty}^{\infty}\int_{-\infty}^{\infty}m_{\mathrm{p}}\,\beta(D_{\mathrm{p}},D'_{\mathrm{p}})\,\mathrm{d}N_{\mathrm{PL}}\,\mathrm{d}N'_{\mathrm{LN}}, \tag{29}$$

where $\beta(D_{\mathrm{p}},D'_{\mathrm{p}})$ is the coagulation coefficient of particles with ~~diameters~~ the diameters of D_{p} and D'_{p} calculated with the equation

$$\beta(D_{\mathrm{p}},D'_{\mathrm{p}}) = 2\pi(D_{\mathrm{p}}+D'_{\mathrm{p}})(\mathcal{D}_{\mathrm{p}}+\mathcal{D}'_{\mathrm{p}})f(Kn\mathrm{Kn}_{\mathrm{coag}}), \tag{30}$$

where ~~$f(Kn_{\mathrm{coag}})$~~ $f(\mathrm{Kn}_{\mathrm{coag}})$ is the transition regime function of Dahneke (1983)

$$f(Kn\mathrm{Kn}_{\mathrm{coag}}) = \frac{1+Kn_{\mathrm{coag}}}{1+2Kn_{\mathrm{coag}}+2Kn_{\mathrm{coag}}^2}\,\frac{1+\mathrm{Kn}_{\mathrm{coag}}}{1+2\mathrm{Kn}_{\mathrm{coag}}+2\mathrm{Kn}_{\mathrm{coag}}^2}, \tag{31}$$

where ~~Kn_{coag}~~ $\mathrm{Kn}_{\mathrm{coag}}$ is the Knudsen number for coagulation

$$Kn\mathrm{Kn}_{\mathrm{coag}} = \frac{4(\mathcal{D}_{\mathrm{p}}+\mathcal{D}'_{\mathrm{p}})}{(D_{\mathrm{p}}+D'_{\mathrm{p}})\sqrt{\bar{c}^2+\bar{c}'^2}}, \tag{32}$$

where $\bar{c}$ and $\bar{c}'$ are the mean thermal velocities of particles with the diameters of D_{p} and D'_{p}.

The integrals in Eqs. (24) – (29) cannot be solved analytically in the transition regime because Eq. (31) cannot be presented in a polynomial form. Therefore, the integrals are calculated numerically ~~. Gaussian quadratures are used here to reduce the associated computing time; they provide the optimal particle diameters and their weights for efficient evaluation of the integrals. The Hermite-Gauss quadrature (Steen et al., 1969) is used in the integrals involving the LN distribution, as the density function of the LN distribution Eq. (8) is in the form of the weight function of the Hermite-Gauss quadrature e^{-x^2}. E.g., an integral becomes, using the Hermite-Gauss quadrature,~~

~~$$\frac{N_{\mathrm{LN}}}{\sqrt{\pi}} \sum_{j=1}^{n} w_j \beta(D_j, D'_{\mathrm{p}})$$~~

~~where D_j and w_j are the abscissa and the weight for the bin j obtained from the quadrature, and n is the degree of the quadrature. In this article, the degree of $n = 5$ is used for the LN distribution denoting that the integrals are calculated with five diameter values. The integrals involved in the PL distribution are in the form of D_{p}^{α} which is not a weight function of any specific quadrature; therefore, a Gaussian quadrature for this purpose was developed. E.g., an integral becomes, using the quadrature developed here,~~

~~$$\frac{N_{\mathrm{PL}} \ln d^{\alpha}}{d^{\alpha} - 1} \sum_{j=1}^{n} w_j \beta(D_j, D'_{\mathrm{p}})$$~~

~~where D_j and w_j are the abscissa and the weight for the bin j obtained from the quadrature. The degree of $n = 4$ is used for the PL distribution.~~

~~The degrees of the quadratures, 4 and 5, are relatively low, which reduces the accuracy of the coagulation modelling, but due to double integrals in the coagulation terms, the computations for the coagulation coefficient is performed n squared (here $4 \times 4 = 16$, $4 \times 5 = 20$, or $5 \times 5 = 25$) times. Therefore, the degrees are kept low to maintain computational efficiency~~or by using quadratures in the same manner as with the condensation term described in Appendix A.

2.2.4 Particle losses

The losses due to coagulation of the particles in the PL+LN distribution to the background distribution ~~not included in~~ excluded from the PL+LN distribution are considered the coagulational losses. Particles in the background distribution are assumed to be significantly larger than the particles in the PL+LN distribution. Therefore, the particle diameters of the background distribution can be approximated with a single diameter value, e.g., $\mathrm{CMD}_{\mathrm{bg}}$ (count median diameter). According to Kerminen and Kulmala (2002), the coagulation coefficient will then become

$$\beta(D_{\mathrm{p}}, \mathrm{CMD}_{\mathrm{bg}}) \approx \beta(D_1, \mathrm{CMD}_{\mathrm{bg}}) \left(\frac{D_{\mathrm{p}}}{D_1} \right)^{l_{\mathrm{bg}}}, \tag{33}$$

where l_{bg} is the exponent depending on $\mathrm{CMD}_{\mathrm{bg}}$. The value of l_{bg} ranges between -2 and -1 (Lehtinen et al., 2007). The coagulational loss term, e.g., for a number concentration is

$$\mathrm{loss}_{N_i}^{\mathrm{coag}} = N_{\mathrm{bg}} \int_{-\infty}^{\infty} \beta(D_{\mathrm{p}}, \mathrm{CMD}_{\mathrm{bg}}) \mathrm{d}N_i \approx N_{\mathrm{bg}} \beta(D_1, \mathrm{CMD}_{\mathrm{bg}}) D_1^{-l_{\mathrm{bg}}} \int_{-\infty}^{\infty} D_{\mathrm{p}}^{l_{\mathrm{bg}}} \mathrm{d}N_i, \tag{34}$$

in which the last integral can be solved analytically. The analytical solutions for the coagulational loss terms are

$$\mathrm{loss}_X^{\mathrm{coag}} = XN_{\mathrm{bg}} \cdot \begin{cases} \beta(D_1, \mathrm{CMD}_{\mathrm{bg}}) \left(\frac{\alpha}{\alpha+l_{\mathrm{bg}}}\right) \left(\frac{d^{\alpha+l_{\mathrm{bg}}}-1}{d^{\alpha}-1}\right), & X = N_{\mathrm{PL}} \\ \beta(D_1, \mathrm{CMD}_{\mathrm{bg}}) \left(\frac{\alpha+2}{\alpha+2+l_{\mathrm{bg}}}\right) \left(\frac{d^{\alpha+2+l_{\mathrm{bg}}}-1}{d^{\alpha+2}-1}\right), & X = S_{\mathrm{PL}} \\ \beta(D_1, \mathrm{CMD}_{\mathrm{bg}}) \left(\frac{\alpha+3}{\alpha+3+l_{\mathrm{bg}}}\right) \left(\frac{d^{\alpha+3+l_{\mathrm{bg}}}-1}{d^{\alpha+3}-1}\right), & X = M_{\mathrm{PL}} \\ \beta(D_{\mathrm{g}}, \mathrm{CMD}_{\mathrm{bg}}) \exp\left[\frac{1}{2} l_{\mathrm{bg}}^2 \ln^2 \sigma\right], & X = N_{\mathrm{LN}} \\ \beta(D_{\mathrm{g}}, \mathrm{CMD}_{\mathrm{bg}}) \exp\left[\left(\frac{1}{2} l_{\mathrm{bg}}^2 + 2l_{\mathrm{bg}}\right) \ln^2 \sigma\right], & X = S_{\mathrm{LN}} \\ \beta(D_{\mathrm{g}}, \mathrm{CMD}_{\mathrm{bg}}) \exp\left[\left(\frac{1}{2} l_{\mathrm{bg}}^2 + 3l_{\mathrm{bg}}\right) \ln^2 \sigma\right], & X = M_{\mathrm{LN}} \end{cases} \tag{35}$$

when α is not 0 or $-l_{\mathrm{bg}}$.

The losses to walls due to diffusion of particles are considered the depositional losses. They are modelled with the method of Hussein et al. (2009), in which the deposition rate of particles in a test chamber is

$$\lambda = \frac{1}{V} \sum_w A_w u \tag{36}$$

where V is the volume of the chamber, A_w is the surface area of the wall w, and u is the deposition velocity of particles. A simple approximation for the deposition velocity is used here

$$u \propto D_{\mathrm{p}}^{-1}, \tag{37}$$

which is valid for particles smaller than $100\,\mathrm{nm}$ according to Lai and Nazaroff (2000). The depositional loss term, e.g, for a number concentration now become

$$\mathrm{loss}_{N_i}^{\mathrm{dep}} = \int_{-\infty}^{\infty} \lambda \mathrm{d}N_i = k_{\mathrm{dep}} \int_{-\infty}^{\infty} D_{\mathrm{p}}^{-1} \mathrm{d}N_i \tag{38}$$

where all effects, except the effect of the diameter, are included in the deposition coefficient k_{dep}. The last integral can be solved analytically, from which the depositional loss terms become

$$\mathrm{loss}_X^{\mathrm{dep}} = Xk_{\mathrm{dep}} \cdot \begin{cases} D_1^{-1} \left(\frac{\alpha}{\alpha-1}\right) \left(\frac{d^{\alpha-1}-1}{d^{\alpha}-1}\right), & X = N_{\mathrm{PL}} \\ D_1^{-1} \left(\frac{\alpha+2}{\alpha+1}\right) \left(\frac{d^{\alpha+1}-1}{d^{\alpha+2}-1}\right), & X = S_{\mathrm{PL}} \\ D_1^{-1} \left(\frac{\alpha+3}{\alpha+2}\right) \left(\frac{d^{\alpha+2}-1}{d^{\alpha+3}-1}\right), & X = M_{\mathrm{PL}} \\ D_{\mathrm{g}}^{-1} \exp\left(\frac{1}{2} \ln^2 \sigma\right), & X = N_{\mathrm{LN}} \\ D_{\mathrm{g}}^{-1} \exp\left(-\frac{3}{2} \ln^2 \sigma\right), & X = S_{\mathrm{LN}} \\ D_{\mathrm{g}}^{-1} \exp\left(-\frac{5}{2} \ln^2 \sigma\right), & X = M_{\mathrm{LN}} \end{cases} \tag{39}$$

when α is not 0 or 1.

The effect of particle losses on the PL distribution is seen as decreased α. In the trivial case, as in Eq. (1), α becomes less than zero when $k_{\text{dep}} > g$. This effect is due to increased losses with increasing particle diameters because larger particles have longer residence times from the moment since their formation. However, Eq. (37) counteracts in this effect by decreasing the deposition velocity with increasing particle size, but with small g, the effect of increased residence time dominates over the ~~the~~ effect of decreased deposition velocity. Additionally, ~~the coagulational lossesfurther decrease~~ α is further decreased due to coagulational losses.

2.2.5 Intermodal particle transfer

The intermodal coagulation is included together with the intramodal coagulation in the coagulation terms (coag_X) seen in Eqs. (24) – (29). The coagulational ($\text{transfer}_X^{\text{coag}}$) and condensational ($\text{transfer}_X^{\text{cond}}$) transfer are modelled as follows.

Particles with the diameter higher than the cut diameter

$$D_{\text{coag}} = \left(D_2^3 - D_{\text{p}}'^3\right)^{1/3} \tag{40}$$

form particles with the diameter higher than D_2 after coagulating with a particle having a diameter of D_{p}', assuming full coalescence (Fig. 2). Those resultant particles are transferred from the PL distribution to the LN distribution, because their particle diameters will correspond with the form of a log-normal distribution rather than a power law distribution, which can be observed using a highly accurate sectional model. The coagulational transfer terms are negative for the PL distribution and positive for the LN distribution to conserve the moments, and they are expressed as

$$\text{transfer}_{N_{\text{PL}}} = -\,\text{transfer}_{N_{\text{LN}}} = -\frac{1}{2}\int_{-\infty}^{\ln D_{\text{coag}}}\int_{\ln D_{\text{coag}}}^{\infty} \beta(D_{\text{p}}, D_{\text{p}}')\,\mathrm{d}N_{\text{PL}}\,\mathrm{d}N_{\text{PL}}' \tag{41}$$

$$\text{transfer}_{S_{\text{PL}}} = -\,\text{transfer}_{S_{\text{LN}}} = -\frac{1}{2}\int_{-\infty}^{\ln D_{\text{coag}}}\int_{\ln D_{\text{coag}}}^{\infty} \left(s_{\text{p}}^{\frac{3}{2}} + s_{\text{p}}'^{\frac{3}{2}}\right)^{\frac{2}{3}} \beta(D_{\text{p}}, D_{\text{p}}')\,\mathrm{d}N_{\text{PL}}\,\mathrm{d}N_{\text{PL}}' \tag{42}$$

$$\text{transfer}_{M_{\text{PL}}} = -\,\text{transfer}_{M_{\text{LN}}} = -\frac{1}{2}\int_{-\infty}^{\ln D_{\text{coag}}}\int_{\ln D_{\text{coag}}}^{\infty} \left(m_{\text{p}} + m_{\text{p}}'\right)\beta(D_{\text{p}}, D_{\text{p}}')\,\mathrm{d}N_{\text{PL}}\,\mathrm{d}N_{\text{PL}}', \tag{43}$$

which are calculated using the quadrature ~~technique~~ or numerical integration as in the case of the coagulation terms.

Considering a time step of Δt in a Lagrangian simulation, particles with the diameters larger than $D_{\text{cond}} = D_2 - g\,\Delta t$ will grow due to condensation to ~~become~~ have the diameters larger than D_2 (Fig. 2). Modelling condensation only, the value of D_2 at the next time step would increase to $D_2 + g\,\Delta t$. The condensational transfer is used to transfer the particles in the PL distribution with the diameters of $D_{\text{cond}} < D_{\text{p}} < D_2$ to the LN distribution. However, if the condensational transfer is modelled fully, D_2 would never increase and all condensation would affect the LN distribution only. In that case, the distributions would separate from each other. For this reason, the effect of condensational transfer is dampened using a factor γ as a multiplier in the condensational transfer equations. The factor can obtain values between ~~0 and 1~~zero and unity, and it describes how the particles

~~are~~ will be distributed between the PL and the LN distributions. The value $\gamma = 0$ produces a distribution that will be mainly in a power law form; the value $\gamma = 1$ produces a log-normal distribution only. To choose a suitable value for γ for a simulation, the user should consider how well does the aerosol formation event follow the approximations of the theory described here. The value 0 is suitable only when the aerosol processes follow the theory exactly. To simulate a realistic particle formation event, the value has to be increased towards unity using the following guidelines. The more the following conditions are met, the higher γ should be used: (1) particle formation or growth are multicomponent processes, (2) the particle formation rate or the condensation growth rate vary significantly with time, (3) the condensational growth rate varies significantly with the particle size, (4) the background aerosol acting as a coagulation sink does not remain in a nearly constant state during the time domain of the simulation, (5) particle sizes in the background aerosol are not significantly higher than in the PL+LN distribution, (6) the depositional losses cannot be approximated with as simple form as described here, e.g., in the case of complex geometry or turbulent flow. In real atmospheric particle formation events, γ should rarely has the value of less than 0.5, which can also be used as an initial guess if figuring the previous guidelines is problematic. If the shapes of the distributions to be modelled are initially known, the value of γ can be adjusted to obtain a proper model output, e.g., in the case of inverse modelling. The factor γ can also be considered a time-dependent function or a spatially varying variable, but here we concentrate only to constant values of γ because the theory behind the value of γ is currently unknown.

The number of particles in the PL distribution to be transferred to the LN distribution due to the condensational transfer in the time step of Δt is

$$N_{\mathrm{PL}\to\mathrm{LN}} = \gamma \int_{\ln D_{\mathrm{cond}}}^{\ln D_2} \left.\frac{\mathrm{d}N}{\mathrm{d}\ln D_\mathrm{p}}\right|_{\mathrm{PL}} \mathrm{d}\ln D_\mathrm{p}. \tag{44}$$

Considering infinitesimally small time step ($\Delta t \to 0$), D_{cond} approaches D_2 and $N_{\mathrm{PL}\to\mathrm{LN}}$ approaches

$$\gamma \frac{g\Delta t}{D_2} \left.\frac{\mathrm{d}N}{\mathrm{d}\ln D_\mathrm{p}}\right|_{\mathrm{PL},\, D_\mathrm{p}=D_2}. \tag{45}$$

The transferred amounts for S and M are obtained in the same approach as in Eq. (20), and they are negative for the PL distribution and positive for the LN distribution. Hence, the term for the condensational transfer becomes

$$\mathrm{transfer}_X^{\mathrm{cond}} = \gamma \frac{g(t)}{D_2} \left.\frac{\mathrm{d}N}{\mathrm{d}\ln D_\mathrm{p}}\right|_{\mathrm{PL},\, D_\mathrm{p}=D_2} \cdot \begin{cases} -1, & X = N_{\mathrm{PL}} \\ -s_2, & X = S_{\mathrm{PL}} \\ -m_2, & X = M_{\mathrm{PL}} \\ +1, & X = N_{\mathrm{LN}} \\ +s_2, & X = S_{\mathrm{LN}} \\ +m_2, & X = M_{\mathrm{LN}} \end{cases}, \tag{46}$$

where s_2 and m_2 are the surface area and the mass of the particle with the diameter of D_2. ~~Condensational~~ The condensational transfer does not alter the moments of the total distribution because particles are not altered in the transfer, it only transfers the

particles between the distributions; therefore, the value of γ has a minor effect only on the moments, but a noticeable effect on the shape of the PL+LN distribution.

3 ~~Model validation and test simulations~~Simulation setup for the evaluation of the PL+LN model

The PL+LN model was ~~validated and tested with simulations of artificial~~ evaluated with the simulations of theoretical test cases and a real particle formation case. The ~~validation~~ evaluation was done against sectional models that yield accurate results due to a ~~large~~ high number of size sections. Two types of sectional models were used: fixed-sectional (FS) and moving-center fixed-sectional (MC) models. The ~~FS model provides~~ models are further subdivided depending on the amount of size sections they use. FS models provide the best accuracy for the particle number concentration and ~~the MC model~~ MC models for the mass concentration, when a high number of size sections is modelled. The results from different models and from measurement data are examined by comparing the ~~relative errors of~~ distributions, the moments (N, S, and M) and the variables, GMD (geometric mean diameter) and GSD (geometric standard deviation). GMD and GSD can be calculated from a continuous or ~~from~~ a discrete total distribution with the equations

$$\ln \mathrm{GMD} = \frac{1}{N} \int_{-\infty}^{\infty} \ln D_\mathrm{p} \, \mathrm{d}N = \frac{1}{N} \sum_j N_j \ln D_{\mathrm{p},j} \tag{47}$$

$$\ln^2 \mathrm{GSD} = \frac{1}{N} \int_{-\infty}^{\infty} \ln^2 \left(\frac{D_\mathrm{p}}{\mathrm{GMD}} \right) \mathrm{d}N = \frac{1}{N} \sum_j N_j \ln^2 \left(\frac{D_{\mathrm{p},j}}{\mathrm{GMD}} \right), \tag{48}$$

where $D_{\mathrm{p},j}$ is the ~~particle diameter in the center~~ geometric average particle diameter of the size section j. ~~The reference models, with which the relative errors are calculated, are FS models~~Relative errors of the moments and the variables compared to the reference models are calculated with

$$\delta_X = \frac{X - X_\mathrm{ref}}{X_\mathrm{ref}}, \tag{49}$$

where X and X_ref are the moment or the variable from the model in examination and from the reference model, respectively. FS models are considered the reference models, with the exception of the mass moment, M, in a real particle formation case, for which the reference model is ~~the MC model~~an MC model, because it provides the best mass-conservation.

The capability of the PL+LN model in inverse modelling is also tested using the real measurement data from the particle formation event. The best estimates of the new particle formation rates, $J(t)$, and the condensational growth rates, $g(t)$, obtained from the different models, are compared with each other. These values for $J(t)$ and $g(t)$ are later used in the simulation that is used to examine the output accuracies and computational costs of different models.

The diameter of a newly formed particle was assumed to be a constant, $D_1 = 1.6\,\mathrm{nm}$, in all cases. The value was chosen because it is in the range of a relevant size of a particle from which atmospheric aerosol formation starts (Kulmala et al., 2007) and of a size of a smallest particle that can be detected with the Particle Size Magnifier (PSM) with the detection efficiency of nearly unity (Vanhanen et al., 2011). Single-component modelling was performed assuming a mixture with the particle bulk

density of ~~$\rho = 1.4\,\mathrm{g/cm^3}$~~ $\rho = 1.4\,\mathrm{g\,cm^{-3}}$ as the component. The value was chosen because it is a relevant density of small particles in the atmosphere (Kannosto et al., 2008). ~~Only coagulation rates are affected by the density value.~~

3.1 ~~Test~~ Theoretical test cases

~~Artificial~~ Theoretical test cases were used to compare the PL+LN model output with a highly accurate FS model. The FS model had 1000 size sections between 1.6 and 10 nm ~~and it~~ (FS1000) which is sufficiently dense to produce accurate results. Additionally, the PL+LN model was compared with the model having a log-normal distribution only (LN). All cases were simulated using constant and equal time steps to obtain a reliable comparison; the simulated ~~times~~ time domains ($t_{\max}$) were split into 3000 time steps.

The input parameters of the test cases are presented in Tab. 1. The Atm and Exh cases represent particle formation cases using input parameter values that reflect conditions typical to the atmosphere and to vehicle exhaust, respectively. Typical new particle formation rates in the atmosphere range from 0.01 to $10\,\mathrm{cm^{-3}\,s^{-1}}$ and condensational growth rates from 0.1 to $20\,\mathrm{nm\,h^{-1}}$ (Kulmala et al., 2004). In vehicle exhaust, new particle formation rates can reach up to $10^{10}\,\mathrm{cm^{-3}\,s^{-1}}$ and condensational growth rates up to $20\,\mathrm{nm\,s^{-1}}$ (Rönkkö et al., 2006; Uhrner et al., 2007; Olin et al., 2015). To test the PL+LN model in a wide range of J and g, low values for Atm cases (~~$J = 0.1\,\mathrm{cm^{-3}s^{-1}}$, $g = 1\,\mathrm{nm/h}$~~ $J = 0.1\,\mathrm{cm^{-3}\,s^{-1}}$, $g = 1\,\mathrm{nm\,h^{-1}}$) and high values for the Exh case (~~$J = 10^8\,\mathrm{cm^{-3}s^{-1}}$, $g = 5\,\mathrm{nm/s}$~~ $J = 10^8\,\mathrm{cm^{-3}\,s^{-1}}$, $g = 5\,\mathrm{nm\,s^{-1}}$) were chosen. ~~Constant values for~~ In addition to constant J and g ~~denote time- and size-independent behavior for growth~~values, a case having time-dependent $J(t)$ and a case having time-dependent $J(t)$ and size-dependent $g(D_\mathrm{p})$ were simulated.

The Atm1 case includes simultaneous new particle formation, condensation, intramodal-, and intermodal coagulation. For the Atm2 case, depositional losses were also added. The deposition coefficient ~~$k_{\mathrm{dep}} = 5 \times 10^{-4}\,\mathrm{nm/s}$~~ $k_{\mathrm{dep}} = 1.8\,\mathrm{nm\,h^{-1}}$ was calculated by assuming that particle formation takes place in a test chamber with the dimensions of $3\,\mathrm{m} \times 2\,\mathrm{m} \times 2\,\mathrm{m}$ and with the deposition velocities of salt particles measured by Hussein et al. (2009). For the Atm3 case, a background distribution was added to act as the coagulation sink. The chosen values for the number concentration $N_{\mathrm{bg}} = 10^3\,\mathrm{cm^{-3}}$ and count median diameter $\mathrm{CMD_{bg}} = 100\,\mathrm{nm}$ of the background distribution have been observed, e.g., in a boreal forest area (Riipinen et al., 2007). The value for the coagulational loss exponent $l_{\mathrm{bg}} = -1.6$ was obtained from Lehtinen et al. (2007) using $\mathrm{CMD_{bg}} = 100\,\mathrm{nm}$. ~~For~~ In the Atm4 case, a bell-shaped time-dependent function for the new particle formation rate (a bell-shaped form in the function of the number concentration between 3 and 6 nm is seen in studies of Sihto et al. (2006); Riipinen et al. (2007)) was ~~used:~~ modelled with

$$J(t) = J_0\, e^{-\left(\frac{t-t_0}{\tau_\mathrm{J}}\right)^2}, \tag{50}$$

where $t_0 = 1000\,\mathrm{s}$ is the time at which the highest new particle formation rate ~~$J_0 = 0.1\,\mathrm{cm^{-3}s^{-1}}$~~ $J_0 = 0.1\,\mathrm{cm^{-3}\,s^{-1}}$ occurs and $\tau_\mathrm{J} = 5000\,\mathrm{s}$ represents the width of the bell-shaped curve.

The applicability of the PL+LN model using size-dependent condensational growth rates was evaluated with the Atm5 case, where $g(D_\mathrm{p})$ was modelled using Eqs. (16) – (18) and (23) – (A4). In this case, particles were assumed to consist of the mixture of sulfuric acid and water. The growth is modelled as the growth due to sulfuric acid, $\frac{\mathrm{d}m_{\mathrm{p,H_2SO_4}}}{\mathrm{d}t}$, calculated using the sulfuric

acid vapor concentration $[H_2SO_4] = 0.8 \times 10^7\,\mathrm{cm}^{-3}$, following the growth due to water vapor,

$$\frac{\mathrm{d}m_{\mathrm{p,H_2O}}}{\mathrm{d}t} = \left[\frac{1}{Y_{\mathrm{H_2SO_4}}(D_\mathrm{p})} - 1\right] \cdot \frac{\mathrm{d}m_{\mathrm{p,H_2SO_4}}}{\mathrm{d}t}, \tag{51}$$

where $Y_{\mathrm{H_2SO_4}}(D_\mathrm{p})$ is the mass fraction of sulfuric acid in a particle in water equilibrium, i.e., a particle having the composition with which no condensation or evaporation of water vapor occurs in temperature of 280 K and relative humidity of 60 % when the particle diameter is D_p. The approximation of water equilibrium is reasonable because, with these environmental values, $\sim 2 \times 10^{10}$ times more water molecules than sulfuric acid molecules exist and thus there are probably a sufficient amount of water molecules to condense on the particle to reach the equilibrium state before the next sulfuric acid molecule condenses on it. The properties of the vapors and the particles were calculated, using the equilibrium composition, as described in Olin et al. (2015) . These environmental values were chosen because they are relevant values met in the atmosphere and they cause the condensational growth rate function that is far beyond a constant value in the particle diameter range of this case (from 1.6 nm to 8 nm), as seen in Fig. 4, which provides a beneficial test to examine how the model behaves with size-dependent q.

The Exh case represents simultaneous new particle formation, condensation, intramodal- and intermodal coagulation, coagulational losses, and depositional losses occurring in diesel vehicle exhaust inside the ageing chamber of a laboratory sampling system. The values $N_\mathrm{bg} = 10^6\,\mathrm{cm}^{-3}$ and $\mathrm{CMD_{bg}} = 60\,\mathrm{nm}$ were obtained from the measurements of Rönkkö et al. (2013) and the corresponding $l_\mathrm{bg} = -1.5$ from Lehtinen et al. (2007) using $\mathrm{CMD_{bg}} = 60\,\mathrm{nm}$. The deposition coefficient ~~$k_\mathrm{dep} = 7 \times 10^{-2}\,\mathrm{nm/s}$~~ $k_\mathrm{dep} = 0.07\,\mathrm{nm\,s}^{-1}$ was calculated using the ageing chamber dimensions of 5 cm (diameter) × 100 cm (length) and the deposition velocities of salt particles measured by Hussein et al. (2009). ~~The coagulational transfer was included in the simulations but~~

Because the test cases are purely theoretical, the need of constructing log-normal features to the distributions through the condensational transfer ~~was not.~~

3.2 ~~Mobile aerosol chamber particle formation event~~

~~A particle formation event performed in a mobile aerosol chamber was simulated using the PL+LN, LN, FS, and MC models. The output of the FS model with 720 size sections between 1.6 and 100(FS720) was considered the most accurate number concentration result, and the output of~~ artificially is minimal. In the Atm4 case, a time-dependent new particle formation rate suggests using the condensational transfer, but, according to the analysis of the shapes and the ~~MC model with 100 size sections between 1.6 and 100(MC100) the most accurate mass concentration result. Additionally, FS model with 24 size sections between 1.6 and 300(FS24) and MC model with 6 size sections between 1.6 and 1000(MC6) were used in comparing the computational cost and the accuracy of different models, because these section numbers provide nearly equal computing times as~~ moments of the distributions, the output is not very sensitive to the value of γ, which is probably due to the bell-shaped function for the new particle formation rate that produces distributions containing both power law and log-normal features. In the Atm5 case, a size-dependent condensational growth rate outputs size distributions having features of a different kind, and thus the PL+LN ~~model. The upper limits for particle diameters of FS24 and MC6 models are higher due to their high numerical~~

~~diffusion~~distribution does not fit very satisfactorily in this case. According to the analysis of the shapes and the moments of the distributions in the Atm5 case, the best estimate for γ is 0.25, which was used in the Atm5 case; $\gamma = 0$ was used in all the other cases.

3.2 Mobile aerosol chamber particle formation event

The mobile aerosol chamber is a Teflon bag with the dimensions of $3\,\mathrm{m} \times 2\,\mathrm{m} \times 2\,\mathrm{m}$. The chamber is operated in a batch process, i.e., firstly, the chamber is filled with the air sample, and secondly, the sample is measured from the chamber. ~~UVC lights (~~UV lights with the wavelength of 254 nm (UVC) are used in the chamber to initiate new particle formation and to boost the aging of the aerosol through photochemical processes. The chamber simulates a particle formation event occurring in the atmosphere, but with shorter time scale due to the UV lights. The chamber is designed to be mobile; therefore, it is fit to a car trailer.

The particle formation event measurement was performed at a street canyon measurement site of Helsinki Region Environmental Services Authority (HSY) located in Mäkelänkatu, Helsinki, Finland. The street had dense traffic during the measurement in ~~April 22nd~~ 22 April 2015. The chamber was firstly filled with urban air ~~, andonce filled;~~ and, once filled, the air sample was sucked with the measurement devices located in the mobile laboratory vehicle.

3.2.1 Processing the experimental data

The aerosol sample was measured using Airmodus ~~PSM~~Particle Size Magnifier (PSM), TSI Ultrafine Condensation Particle Counter (CPC), TSI Nano Scanning Mobility Particle Sizer (Nano-SMPS), TSI Engine Exhaust Particle Sizer (EEPS), and Dekati Electrical Low-Pressure Impactor (ELPI+). PSM in fixed saturator flow setting detects particles with the ~~diameter from~~ diameters of higher than about 1.6 nm (Vanhanen et al., 2011), CPC ~~from~~ higher than about 3.6 nm (Mordas et al., 2008), and Nano-SMPS from about 7 to 64 nm~~at~~ , with the detection efficiency of 50 % or higher. These cut diameters, $D_{\mathrm{PSM}} = 1.6\,\mathrm{nm}$, $D_{\mathrm{CPC}} = 3.6\,\mathrm{nm}$, and $D_{\text{Nano-SMPS}} = 7\,\mathrm{nm}$, are used to combine the data of PSM, CPC, and Nano-SMPS to obtain total aerosol size distributions for the diameter range of 1.6 – 64 nm with

$$\left.\frac{\mathrm{d}N}{\mathrm{d}\ln D_{\mathrm{p}}}\right|_{\text{measured}} = \begin{cases} \frac{\max\{N_{\mathrm{PSM}} - N_{\mathrm{CPC}}, 0\}}{\ln(D_{\mathrm{CPC}}/D_{\mathrm{PSM}})}, & D_{\mathrm{PSM}} \le D_{\mathrm{p}} < D_{\mathrm{CPC}} \\ \frac{\max\{N_{\mathrm{CPC}} - N_{\text{Nano-SMPS}}, 0\}}{\ln(D_{\text{Nano-SMPS}}/D_{\mathrm{CPC}})}, & D_{\mathrm{CPC}} \le D_{\mathrm{p}} < D_{\text{Nano-SMPS}} \\ \left.\frac{\mathrm{d}N}{\mathrm{d}\ln D_{\mathrm{p}}}\right|_{\text{Nano-SMPS}}, & D_{\mathrm{p}} \ge D_{\text{Nano-SMPS}} \end{cases}, \tag{52}$$

where N_{PSM}, N_{CPC}, and $N_{\text{Nano-SMPS}}$ are the total number concentrations measured by the devices, and $\left.\frac{\mathrm{d}N}{\mathrm{d}\ln D_{\mathrm{p}}}\right|_{\text{Nano-SMPS}}$ is the particle size distribution measured by Nano-SMPS. The maximum functions prevent the size distribution to become negative. Before the concentrations were input into Eq. (52), the concentrations output by the devices were synced. The data measured after the event were used in the synchronization, using the assumption that the device outputs are equal in that moment, because particle sizes are well within the range of high detection efficiency of all three devices. Nano-SMPS measures diameters down

to 2 nm, but due to its low accuracy for those diameters, all Nano-SMPS data below 7 nm ~~is~~ was neglected. EEPS and ELPI+ having time resolutions of only 1 s were used to ensure the stability of the aerosol distribution ~~in shorter time scale~~during a Nano-SMPS scan lasting 150 s: no rapid changes in the aerosol distribution were observed in the time scales shorter than 150 s.

Initially, the aerosol in the chamber consisted of a background aerosol mode with ~~particle diameters around~~ CMD of 15 nm and ~~with~~ the concentration of about 4000 cm^{-3}, according to the Nano-SMPS data shown in Fig. 5. No major changes in the distribution were observed until the UV lights were switched on ($t = 0\,\mathrm{s}$). After switching ~~on~~ the UV lights ~~, the number concentration and the particle diameters (Figs. 5 and ??) began to increase, i.e. the nucleation mode appeared~~on, a nucleation mode begins to from, which is seen as the appearance of new particles at small particle diameters. It can be also seen that small particles exist though the growth process proceeds, which implies continuing new particle formation. The total distributions were altered from a power law-shape towards a log-normal-shape. After about 500 s, particle concentration finished increasing (Fig. 6), which occurs because ~~all~~ the gaseous precursors initiating new particle formation began to expire. The decreasing trend of particle number concentration after 500 s was accounted by coagulation and deposition. ~~In the simulation of the event, a bell-shaped function as in~~ The particles of the nucleation mode and of the background mode grew to about 25 nm and to about 60 nm during the event, respectively. The total number, surface area, and mass concentrations of the measured nucleation mode were calculated from the total measured size distributions, Eq. (~~50)was used for the new particle formation rate, because it appeared to correspond well with the number concentration measured by PSM. In this case, the values $J_0 = 800\,\mathrm{cm}^{-3}\,\mathrm{s}^{-1}$ and $t_0 = 368\,\mathrm{s}$~~52), subtracted by log-normal distributions fitted to the background aerosol, assuming spherical particles with the density of 1.4 $\mathrm{g\,cm}^{-3}$. GMD and GSD of the measurement data were calculated also from the nucleation mode size distribution, using Eqs. (47) and (48), although the accuracy of the measured distribution for the diameters below the Nano-SMPS measurement range is poor.

3.2.2 Obtaining $J(t)$ and $g(t)$ through inverse modelling

Obtaining the values for the new particle formation rate, $J(t)$, and ~~$\tau_J = 190\,\mathrm{s}$ were obtained from inverse modelling by comparing the number concentration of the model with the number concentration measured by PSM. The same shape was also used~~ for the condensational growth rate~~function~~

$$g(t) = g_0\, e^{-\left(\frac{t-t_0}{\tau_g}\right)^2},$$

~~where $g_0 = 144\,\mathrm{nm/h}$, $t_0 = 418\,\mathrm{s}$, and $\tau_g = 600\,\mathrm{s}$, which were obtained from inverse modellingby comparing the particle diameters of the model with the particle diameters measured by~~ , $g(t)$, for the particle formation event, occurred in a mobile aerosol chamber, was performed through inverse modelling. A time domain, starting from 152 s before switching the UV lights on and ending to 1663 s after switching the UV lights on, including 13 Nano-SMPS ~~. Inverse modelling was performed, firstly, using a computationally efficient PL+LN model to obtain coarse estimates~~ measurement scans, was simulated using different values for $J(t)$ and $g(t)$~~, and lastly, using an accurate sectional model to fine tune the values. Inverse modelling was performed manually, i.e. iterating the input parameters~~ . Following the approach of Verheggen and Mozurkewich (2006) , the least squares method was used to minimize the errors of the concentrations N, S, and M at 13 time moments which represent the middles

of the Nano-SMPS scans. The values for $J(t)$ and $g(t)$ ~~and checking the correspondence of the particle number concentration and the size distribution with the measured ones were done manually using a trial and error method~~were assumed constants within a time step of a Nano-SMPS scan, 150 s. The condensational growth rate was assumed also size-independent due to the lack of knowledge of the vapors participating in the condensation process. ODE45 solver was used in the simulations, and it provides the time steps that are sufficiently short to keep the result from altering more than 1 % compared to a previous time step but sufficiently long to keep the total computing time convenient.

~~Only~~ Coagulation within the nucleation mode was ~~simulated and~~ included in the simulations, but the coagulational losses to the background mode ~~were neglected. Depositional~~ was neglected because its low number concentration would had a minor effect only on the nucleation mode. The particles formed in this case are possibly multicomponent due to the origin of the vapors, the new particle formation rate seems to vary significantly with time, and the measured distributions are wide, GSD values were up to 2. Therefore, a high value for the condensational transfer factor γ is expected to produce the best results using the PL+LN model. A constant value $\gamma = 0.8$ was used in the simulations because it produces the results that are the closest to the results of highly accurate sectional models, in this case. Due to a high value of γ, the coagulational transfer would had a minor effect only, and therefore it was neglected in the simulations. The depositional losses were modelled using the deposition coefficient ~~$k_{dep} = 0.01\,\mathrm{nm/s}$~~ $k_{dep} = 3780\,\mathrm{nm\,h^{-1}}$ which is obtained by fitting ~~using the measured number concentration data~~ the simulated number concentrations with the measured ones after particle formation and growth were quenched ($t > 1500\,\mathrm{s}$). ~~A time domain starting from 152before switching the UV lights on and ending to 1663after switching the UV lights on was simulated with 15000 equal time steps.During this time domain, particles are formed and grown to about 25~~

Firstly, inverse modelling was performed using the PL+LN model. The time series of $J(t)$ and $g(t)$, that produced the most corresponding concentrations compared to the measured ones (Fig. 6), are presented in Figs. 7 and 8. Secondly, inverse modelling was performed using both an FS model having 400 size sections between 1.6 and 100 nm ~~, formation~~ (FS400) and an MC model having 100 size sections between 1.6 and ~~condensational growth ratesare changed,~~ 100 nm (MC100), separately. The computing times of the FS400 and the MC100 models are significantly longer than of the PL+LN model; therefore, the time series of $J(t)$ and $g(t)$, obtained using the PL+LN model, were used as initial guesses when inverse modelling was performed using the FS400 or the MC100 model, to reduce the computing times. The associated computing time of the automatic inverse modelling procedure using the PL+LN model was approximately 2 orders of magnitude shorter than by using the FS400 or the MC100 model, which implies that a significant improvement in the computing time can be obtained using the PL+LN model in the case of inverse modelling. Inverse modelling was also performed using computationally more efficient LN model.

It can be seen from Fig. 7 that there are only minor differences in the values of $J(t)$ between the different models used in inverse modelling. The PL+LN model seems to need higher new particle formation rates compared to the accurate models, the FS400 and the ~~total distribution was altered from a power law-shape towards a log-normal-shape~~MC100 models. Conversely, the LN model seems to need lower new particle formation rates. These denote that the PL+LN model has a tendency to underestimate the number concentrations, and that the LN model has a tendency to overestimate the number concentrations, because the output number concentrations of the models are nearly equal (Fig. 6). The values of $g(t)$, seen in Fig. 8, have also only minor differences between the different models. The values of $J(t)$ and $g(t)$ before the UV lights ($t < 0\,\mathrm{s}$) seem

unphysically high. That is caused because the simulation begins with no particles at $t = -252\,\mathrm{s}$ but the measurement data include some nucleation mode particles at that time, even though the background aerosol distribution was subtracted from the measured distribution. All the particles are not subtracted because the subtraction was done with a purely log-normal distribution, which is exactly not the case of a measured data. Therefore, the simulation ~~of this event provides a useful test to examine the performance of the~~ time range $-252\,\mathrm{s} < t < -152\,\mathrm{s}$ was used to produce the measured nucleation mode at the time of the first Nano-SMPS scan, $t = -152\,\mathrm{s}$.

The effect of the choice for the lowest particle diameter, D_1, for the PL+LN model ~~in different shapes of a distribution and in changing real-world case~~was also examined by performing inverse modelling with $D_1 = 1\,\mathrm{nm}$ and $D_1 = 3\,\mathrm{nm}$, in addition to $D_1 = 1.6\,\mathrm{nm}$. Approximately 40 % higher values for $J(t)$ were needed to produce the measured concentrations when $D_1 = 1\,\mathrm{nm}$ was used compared to $D_1 = 3\,\mathrm{nm}$. This deviation occurs because smaller particles have higher losses, and with higher value for D_1, the smallest particles do not exist. The situation is the same for sectional models, because the smallest particle size needs to be chosen for them too. The choice for D_1 does not have significant effect on the condensational growth rate, in this case, due to size-independent $g(t)$.

The ~~distributions measured in the chamber were relatively wide, GSD values in the Nano-SMPS data were up to 1.8. For that reason, the condensational transfer was used in~~ effect of the choice for the value of the condensational transfer factor, γ, for the PL+LN model was also examined by performing inverse modelling with the values between 0 and 1, in addition to $\gamma = 0.8$. With the values between 0.4 and 0.9, the times series of $J(t)$ obtained from inverse modelling deviate within 3 %, in average. However, with the values outside of that range, the deviation increased up to 36 %. The highest new particle formation rates are needed when the value of γ is low because the PL distribution dominates the number of particles, which leads to more small particles, which have high losses. Only minor effect (the deviations within 4 %) was seen on the time series of the condensational growth rate when the value of γ was altered between 0 and 1. In conclusion, choosing the value of 0.5 for γ if better guess for its value is lacking, as mentioned earlier, would produce reasonable results.

Figure 9 presents the time series of GMD and GSD of the nucleation mode, obtained from the different models used in inverse modelling and from the measured data. It can be observed that the models output these variables relatively well compared to the measured data, although they were not selected as the variables, of which errors are to be minimized, in inverse modelling. However, underestimations of GSD are seen with the LN model. The measured values of GMD and GSD before the UV lights are inaccurate due to the assumption of a log-normal background aerosol distribution mentioned before.

3.2.3 Simulation setup for the examination of the accuracy and the computational cost of the PL+LN model

To examine the accuracy and computational cost of the PL+LN model~~to provide wide LN distributions; the value of γ was set to 0.8 providing the best corresponding shapes of the distribution compared to the measured ones. Due to high γ,~~ , the simulations using different models were performed using equal time series of $J(t)$ and $g(t)$ and equal time stepping. The time series obtained using the FS400 model are considered the best estimates to produce the measurement results due to the highest number of size sections modelled. Therefore, they were used as the time series for all the models used here, PL+LN, LN, FS400, MC100, FS35, and MC10. FS35 and MC10 denote a fixed-sectional model having 35 size sections and a moving-center

fixed-sectional model having 10 size sections between 1.6 and 300 nm, respectively. These section number were used because they provide approximately the same computing times as the PL+LN model. Higher upper diameter limit for the FS35 and the MC10 models were chosen due to higher numerical diffusion associated to these models, which causes higher concentrations in large particle diameters compared to more accurate models. The time series of $J(t)$ and $g(t)$ used here are presented as fits in Figs. 7 and 8. The fitted functions were used rather than the time series because the time series having sharp edges would produce distributions having sharp edges as well, which would be unphysical. Here, the time series have sharp edges due to a very limited number of data points (Nano-SMPS scans) within the time domain. It is obvious that because the fits are not very near the time series, the outputs of the models will not be very near the measured data. Nevertheless, the fits were used because the purpose here is to examine the accuracy and the computational cost of the PL+LN model, which is done against the highly accurate models, the ~~coagulational transfer would have had a minor effect only; thus, it was neglected from the simulation. The factor γ is a free parameter having no explicit physical meaning; thus~~FS400 and the MC100 models. This comparison is the most properly done when all the models have the same functions for $J(t)$ and $g(t)$. The time domain to be simulated was split into 7953 time steps for all the models. The time splitting was obtained from the ODE45 solver used with the FS400 model. The time steps had the lengths of between 0 and 0.5 s, the shortest ones being in the beginning of the time domain.

The accuracy of the PL+LN model is examined by comparing the relative errors (δ_X) of the moments, N, S, and M, and the variables, GMD and GSD. The reference distributions used in the comparison are the distributions produced by the FS400 model and by the MC100 model, which are considered the models that most accurately conserve the number and the mass concentrations, respectively. The distributions from the FS400 model are used as the reference distribution when calculating δ_X for all the moments and variables, with the exception of the mass concentration, M, for which the MC100 model is used as the reference model. Because the distributions produced by the sectional models are considered here the correct ones rather than the measured distributions, the modelled distributions are used as the reference distributions. In this manner, the differences of the model outputs are caused by the models itself, e.g., due to numerical diffusion or some simplifications used in the model, not by how accurately they correspond with the measured data. The accuracies of the LN, FS35, and MC10 models are also examined.

All the other input parameters were the same as were used with the inverse modelling. The simulations used to examine the model accuracies provide also the possibility of comparing the computational costs of different models, because all the simulations were run using the same computer (Intel Core i5-3470 processor at 3.2 GHz) and had equal time stepping, and therefore equal number of computations of the general dynamic equation per a moment or a size section. Additionally, the sensitivity of the value of γ was ~~also examined using additionally the values~~ examined using also the values of 0.1, 0.5, and 0.9~~for it~~, in addition to the value of 0.8.

4 Results and discussion

4.1 ~~Test~~ Theoretical test cases

Figure 10 shows the size distributions at the ends of the theoretical test simulations using different models. The distributions of the Atm cases during the whole time domain are presented as a video in the Supplement. It can be observed ~~from those~~ that the shape of the distribution produced by the PL+LN model is nearly equal ~~as~~ to the reference distribution (FS1000). The largest deviations between the PL+LN distributions and the reference distributions are the gap between the PL and the LN distribution and the sharp peak in the PL distribution. These are most clearly seen in the Atm4 case where α is ~~highest~~the highest. In the Atm5 case, the shape of the distribution produced by the FS1000 model is different: the distribution of the smallest particles do not follow a power law form due to low condensational growth rates near the particle diameter of D_1. Consequently, the PL+LN model is not able to express the distribution correctly at very small particle sizes. The effect of γ is also seen with the Atm5 case where the ratio of the concentrations of the LN distribution and of the PL distribution is higher due to higher γ. Conversely, the distributions produced by the LN model are far beyond the reference distributions. In the Atm4 ~~case~~ and the Atm5 cases where new particle formation ~~rate decreases~~ rates decrease towards the end of the simulation, the LN model begins to act better while the reference distribution transforms towards a log-normal shape.

The effect of the depositional losses can be seen as a decreased α in the Atm2 case compared to the Atm1 case. Because $k_{\mathrm{dep}} > g$, the value of α becomes negative. Comparing the Atm3 case with the Atm2 case, it can be seen that the coagulational losses decrease α further. ~~Using a decreasing function for $J(t)$ but time-independent g as in~~ In the Atm4 ~~case,~~ and the Atm5 cases, the values of α ~~increases again , because~~ are again increased compared to the Atm3 case. This occurs because $J(t)$ decreases with increasing time but g remains constant, in time, and thus there will be less small particles with increasing time. The distribution of the Exh case is mainly comparable to the Atm1 case with the exception of higher ~~concentrations~~ concentration levels in the Exh case due to higher $\frac{J}{g}$. It can be also observed that the ratio of the concentrations of the LN distribution and of the PL distribution is higher in the Exh case than in the Atm1 case. This is due to increased coagulational transfer in the Exh case because it is calculated through the intramodal coagulation, ~~which~~ of which rate is proportional to N_{PL}^2. The depositional and coagulational losses do not have significant effect on the distribution in the Exh case because $k_{\mathrm{dep}} \ll g$ and $N_{\mathrm{bg}} \ll N$.

~~Table 2~~ Figure 11 shows the relative errors of the ~~variables~~ moments (δ_X) in the PL+LN model compared to the reference model~~(~~, FS1000~~)~~, as a function of time, and Tab. 2 at the ends of the test simulations. The highest relative errors of the total concentrations, N, S, and M, are usually met at the ends of the simulated time domains, and they are less than 2 % in all the cases, except the Atm5 case, the total number concentration N being the most ~~accurate~~accurately conserved moment. In the Atm5 case, $|\delta_X|$ for the moments are 17 % at the highest. The errors of this high level are caused by the reference distribution having features that do not fit well neither with the PL distribution nor with the LN distribution. The form of the size-dependence of the condensational growth rate in the Atm5 case represents, however, one of the worst cases that are to be simulated with the PL+LN model. For comparison, the parameters of the Atm5 case would cause $|\delta_X|$ to reach the levels of 24 % if the condensational transfer is neglected, the levels of 19 % if only the PL distribution is simulated, and the levels of

90 % if only the LN distribution is simulated. GMD and GSD have ~~the relative errors~~ $|\delta_X|$ of less than 0.5 % in the cases with ~~time-independent~~ the constant parameters, but for the Atm4 ~~case~~ and the Atm5 cases, the errors are higher (around ~~±2 %)due to time-dependent new particle formation rate.~~ ±4 %). All the cases, with the exception of the Atm5 case, can be simulated with the PL distribution only to achieve the levels of the relative errors as with the PL+LN distribution, but the need of the LN distribution in addition to the PL distribution arises with the Atm5 case. However, visually inspecting, the LN distribution is needed in all the cases to obtain distributions that have the correct shapes in the highest particle sizes.

The total computing time of the Atm5 case with the PL+LN model compared to the Atm4 case is approximately 2-fold, which is mainly caused by the need of numerical integration in calculation of the condensation terms in the Atm5 case. The associated computing time, and the accuracy, can be controlled by the number of size sections used in numerical integration or by using a polynomial form for the condensational growth rate. Because condensation is calculated using size sections with the FS1000 model, regardless of the size-dependency of the condensational growth rate, the total computing time increases only about 7 % when switching from size-independent condensational growth rates to size-dependent ones. The increase of the total computing time, in that case, is related to additional computations to obtain the values for the condensational growth rate itself.

4.2 Mobile aerosol chamber particle formation event

Particle size distributions obtained from the ~~FS720,~~ FS400, the LN, and the PL+LN models are shown as contour plots in Fig. 5 together with the measured distributions. Comparing the plots of the LN and the PL+LN models with the plot of the ~~FS720~~ FS400 model, it can be seen that the PL+LN model behaves better for small diameters than the LN model. However, there is a sharp discontinuity between the PL and the LN distributions in the PL+LN model. In this case, the discontinuity is mainly formed due to the condensational transfer that is separating the distributions from each other. It is also seen that the PL+LN model is capable in vanishing the PL distribution when the aerosol ages and begins to have mainly a log-normal like form. Particle distributions ~~528~~378 and 978 s after the UV lights were switched on are also shown in Fig. 12. The ~~shape of the distribution~~ time $t = 378$ s presents the center of the Nano-SMPS scan where the new particle formation rate is at the highest. At the time $t = 978$ s, new particle formation was mostly quenched but growth still occurred. The shapes of the distributions produced by the PL+LN model ~~is~~ are near the reference ~~distribution (FS720~~distributions (FS400) with the exception of the ~~gap~~ gaps between the PL and the LN ~~distribution. The shape of the distribution~~ distributions. The shapes of the distributions at the largest particles produced by the LN model ~~corresponds~~ correspond better with the measured ~~distribution~~ distributions than at the smallest particles. In the simulation using the ~~FS24~~ FS35 model, a high numerical diffusion that widens the distribution towards the larger particles is seen. The distributions produced by the MC models, MC100 and MC10, have sharp features but follow the distributions produced by the FS400 model. The number of size sections in the MC10 model is obviously too low to plot the distributions well. The modelled distributions at the time $t = 978$ s are not very near the measured distribution due to the fitted functions used for $J(t)$ and $g(t)$.

Table 3 ~~represents~~ presents the computational costs and the accuracies of the models. ~~Computational costs are reported as computing times~~ Computing times are reported relative to the computing time of the PL+LN simulation~~(110~~, 24 s~~). All~~

~~simulations were run using the same computer (Intel Core i5-3470 processor at 3.2)~~. The PL+LN model has the best accuracy for the total number (N) and mass (M) concentrations compared to the sectional models with approximately the same computing time (~~FS24 and MC6~~FS35 and MC10) and to the LN model. The ~~FS24 model , however, is more~~ FS35 model is relatively accurate in N output but suffers from high numerical diffusion seen as high relative error (~~135~~79 %) in M. The PL+LN model has also low memory consumption due to a low number of variables. The LN model ~~has~~is, however, the most ~~computational efficiency~~ computationally efficient but the relative errors are high too (up to ~~9.87~~17 % in N).

The development of N~~is~~ , M, GMD, GSD, and the relative errors of N and M are shown in Fig. **??**~~, from which it~~ 13. It can be seen that the PL+LN model has nearly the same output for N as the reference models during the whole time domain. The beginning of the overestimation of N in the LN and in the ~~MC6~~ MC10 models are clearly seen at the region where the new particle formation has the highest rate ($t_0 = 368$ ~~s~~$t \approx 400$ s). The ~~development of GMD can be seen from Fig. **??**: the~~ LN model functions better in M, but overestimations are encountered with the MC10 model. In addition to the MC10 model, the FS35 model overestimates M clearly. The PL+LN model ~~produces GMD~~ outputs M very accurately during the whole time domain~~, the LN model nearly as accurately as~~ . GMD is overestimated slightly with the FS35 and the MC10 models due to numerical diffusion, but the PL+LN and the LN models output it accurately during the whole time domain. The highest error in GMD produced by the PL+LN model ~~, but the FS24 model overestimates GMD at the end of the simulation due to numerical diffusion. The MC6 model overestimates GMD during the whole time domain and has uneven features~~is the underestimation of 1.3 % compared to the FS400 model which occurs at the time of the highest new particle formation rate. The highest deviations between the models are seen in the development of GSD~~(Fig. **??**)~~. The PL+LN model underestimates GSD ~~slightly~~ with 3 % at the end of the time domain, but the FS35 model overestimates it significantly and the MC10 model and the LN model ~~significantly at the time of the highest new particle formation rates and slightly at the end of the time domain. The FS24 model overestimates GSD significantlyduring the whole time domain and the MC6~~ underestimate it significantly. Additionally, the MC10 model suffers from uneven behavior ~~and underestimations. The development of GMD and GSD for the measurement data is not shown due to the lack of an accurate distribution data for the diameters below the Nano-SMPS measurement range~~due to its low number of size sections. The relative errors of the moments, δ_N and δ_M, are at the highest levels mostly at the ends of the simulations. The models having at least the same computational efficiency as the PL+LN model (the FS35, the MC10, and the LN models) fail to produce N and M accurately: the relative errors can be up to tens of percent. The relative errors with the PL+LN model are below 2 % during the whole time domain. In conclusion, the PL+LN model has the best accuracy for the production of N, M, GMD, and GSD during the whole time domain compared to the other models having at least the same computational efficiency~~(LN, FS24, and MC6).~~

~~The functions $J(t)$ and $g(t)$ can be optimized so that the other models would produce the most accurate time series for N, GMD, and GSD if the comparison is done against the measurement data. E.g., the LN model would produce an accurate time series for N if $J(t)$ is decreased approximately with 10. However, in that kind of inverse modelling, too low $J(t)$ is obtained because the most correct $J(t)$ would be obtained from the most accurate model, a sectional model. Therefore, the comparison must be done against the output of a sectional model rather than the measurement data. Additionally, an incorrectly predicted $J(t)$ would also cause errors in the prediction of other parameters, such as $g(t)$.~~

Figure 14 ~~represents the same distributions as in Fig. 12, but with~~ presents the particle distribution at the time of $t = 978$ s using the PL+LN model ~~using different values for~~ with different values of γ. It can be seen that the PL distribution in the total distribution is mostly dominating when a low value for γ is used (left pane). Conversely, using a high value ~~produces more a~~ of γ (right pane) produces a more log-normal like form, which, at least in this case, corresponds best with the measured distribution. However, a gap between the PL and the LN distributions is larger in cases of high values of γ. The sensitivity of the value of γ is also shown in Tab. 4, in which the relative errors of N, M, GMD, and GSD are reported. It can be seen that a value ~~between 0.5 and~~ near 0.8 ~~may provide~~ provides the most accurate results, depending on the variable of the main interest. ~~Comparing~~ By comparing the errors of N and M produced by the PL+LN model with the errors produced by different models reported in Tab. 3, it can be seen that the lowest errors for N and M simultaneously are produced by the PL+LN model regardless of the value of γ used. Contour plots with different values of γ are shown in Fig. 15. By visual inspection, it can be seen that the values 0.5 and 0.8 produce the contour plots being the closest to the measured contour plot in Fig. 5.

5 Conclusions

The combined power law and log-normal distribution (PL+LN) model was developed to represent a particle size distribution in simultaneous new particle formation and growth situation, in which log-normal distributions do not represent the aerosol sufficiently well. The PL+LN distribution combines a power law form typical to simultaneous new particle formation and growth situation at the initial steps of aerosol formation with a log-normal form typical to aged aerosols. The PL+LN model is useful in simulations involving the initial steps of aerosol formation where a sectional representation of the size distribution causes too high computational cost, such as in multidimensional simulations or in the case of ~~obtaining input parameters as the model output through inverse modelling~~using inverse modelling to obtain the best estimates for parameters used as input in the model. These parameters can be, e.g., the new particle formation rate or the condensational growth rate that the most accurately produce the distributions as the measured ones. The model uses six moment variables to model the distribution, denoting lower memory consumption compared to sectional models which require tens or hundreds variables. The model includes simultaneous new particle formation, condensation, coagulation, coagulational loss, and depositional loss processes.

The PL+LN model was ~~validated and tested using~~ evaluated using theoretical test simulations and a real-world particle formation event simulation. The test cases represented particle formation events with the parameters related to the atmosphere and to vehicle exhaust. The real-world case was the simulation of a particle formation event measurement performed in a mobile aerosol chamber at Mäkelänkatu street canyon measurement site in Helsinki, Finland. The ~~validation~~ evaluation was done against highly accurate sectional models using fixed-sectional and moving-center fixed-sectional methods. The ~~conservation~~ accuracy of the total number, surface area, and mass concentrations ~~in~~ simulated by the PL+LN model was examined: the relative errors of the concentrations were lower than 2 % compared to the highly accurate sectional models, with the exception of a theoretical test case having size-dependent condensational growth rate with which the relative errors were up to 17 % due to the shape of the size distribution produced. The performance of producing geometric mean diameter (GMD) and geometric standard deviation (GSD) of the total distributions ~~in the test cases~~ using different models was also examined: the highest

relative error with the PL+LN model was ~~2.143~~3.5 % for ~~GSD when time-dependent~~ GMD when size-dependent new particle formation rate was modelled ~~, but the errors were lower than 0.5when constant rate was modelled~~in a theoretical test case. The shapes of the distributions produced by the PL+LN model were noticeably more similar to the reference distributions than produced by a simple log-normal distribution model.

Considering the same computing time as the PL+LN model in the chamber event simulation, only ~~24~~ 35 size sections for a fixed-sectional ~~and 6~~ model and 10 size sections for a moving-center fixed-sectional ~~models~~ model were allowed to be modelled. With these section numbers, the results for the number and mass concentrations, for GMD, and for GSD were not as accurate as using the PL+LN model: the relative errors were up to tens of percent. Additionally, a simple log-normal distribution model seemed to output GMD relatively well ~~but overestimated number concentration~~ in this case, but the number concentration was overestimated and GSD was underestimated during almost the whole time domain, especially at times when new particle formation and growth occurred simultaneously.

The new particle formation rates, $J(t)$, and the condensational growth rates, $g(t)$, used in the chamber simulation were obtained through inverse modelling. Firstly, the PL+LN and the LN models were used to obtain the best estimates for $J(t)$ and ~~underestimated GSD~~ $g(t)$ that produce the measured concentrations the most accurately. Secondly, the time series of $J(t)$ and $g(t)$ obtained using the PL+LN model were used as initial guesses in the inverse modelling with the highly accurate models. Only minor differences were found in the time series of $J(t)$ and $g(t)$ obtained using different models: the PL+LN model overestimates and the LN model underestimates $J(t)$ slightly. The associated computing times using the highly accurate sectional models are approximately 2 orders of magnitude longer compared to the PL+LN model. Therefore, the PL+LN model provides a rapid and accurate solution to obtain input parameters, such as new particle formation and condensational growth rates, from the measured data through inverse modelling.

Appendix A: Gaussian quadratures

The Hermite-Gauss quadrature (Steen et al., 1969) is used in the integrals involving the LN distribution, as the density function of the LN distribution, Eq. (8), is in the form of the weight function of the Hermite-Gauss quadrature e^{-x^2}. E.g., an integral

$$\int_{-\infty}^{\infty} D_\mathrm{p}^2\, g(t, D_\mathrm{p})\, \frac{\mathrm{d}N}{\mathrm{d}\ln D_\mathrm{p}}\bigg|_\mathrm{LN} \mathrm{d}\ln D_\mathrm{p} = \frac{N_\mathrm{LN}}{\sqrt{2\pi}\ln\sigma} \int_{-\infty}^{\infty} D_\mathrm{p}^2\, g(t, D_\mathrm{p}) \exp\left[-\frac{\ln^2(D_\mathrm{p}/D_\mathrm{g})}{2\ln^2\sigma}\right] \mathrm{d}\ln D_\mathrm{p} \tag{A1}$$

becomes, using the Hermite-Gauss quadrature,

$$\frac{N_\mathrm{LN}}{\sqrt{\pi}} \sum_{j=1}^{n} w_j D_\mathrm{p}^2\, g(t, D_j) \tag{A2}$$

where D_j and w_j are the abscissa and the weight for the bin j obtained from the quadrature, and n is the degree of the quadrature. In this article, the degree of $n = 5$ is used for the LN distribution denoting that the integrals are calculated with five diameter values. The integrals involved in the PL distribution are in the form of D_p^α which is not a weight function of any

specific quadrature; therefore, a Gaussian quadrature for this purpose was developed. E.g., an integral

$$\int_{-\infty}^{\infty} D_\mathrm{p}^2\, g(t, D_\mathrm{p})\, \frac{\mathrm{d}N}{\mathrm{d}\ln D_\mathrm{p}}\bigg|_\mathrm{PL} \mathrm{d}\ln D_\mathrm{p} = \frac{N_\mathrm{PL}\alpha}{D_2^\alpha - D_1^\alpha} \int_{\ln D_1}^{\ln D_2} D_\mathrm{p}^2\, g(t, D_\mathrm{p})\, D_\mathrm{p}^\alpha \,\mathrm{d}\ln D_\mathrm{p} \tag{A3}$$

becomes, using the quadrature developed here,

$$\frac{N_\mathrm{PL} \ln d^\alpha}{d^\alpha - 1} \sum_{j=1}^{n} w_j D_\mathrm{p}^2\, g(t, D_j) \tag{A4}$$

where D_j and w_j are the abscissa and the weight for the bin j obtained from the quadrature. The degree of $n = 4$ is used for the PL distribution.

The degree of the quadrature developed here, $n = 4$, is relatively low, but by using higher degrees, internal equations in the quadrature will become more complicated which results in increased computing time. In the cases described in this article, the degree of 4 results in the absolute relative errors of the condensation and the coagulation terms less than 10^{-2} compared to a very high degree numerical integration or, if exists, to an analytical solution, but only when $\alpha > 0.5$, in the case of the condensation terms, and when $d < 3$, in the case of the coagulation terms. A drawback of the quadrature with a low degree is that with the values of $\alpha < 0.5$ (condensation) and $d > 3$ (coagulation), errors increase, which causes numerical problems during a simulation. Therefore, the quadrature is used only with the values of $\alpha < 0.5$ (condensation) or $d < 3$ (coagulation), but numerical integration as in Eq. (23) otherwise, or, if exists, an analytical solution for the condensation terms as in Eq. (22). In numerical integration, $n = 200$ size sections are used for condensation calculation, which is required to produce the absolute relative errors less than 10^{-2}. Calculating coagulation using numerical integration, $n = 20$ is used. However, with only 20 size sections, relative errors increase up to 30 % when d increases towards 100 and α towards ± 5. Nevertheless, a higher degree is not used due to increasing computing time, which is squarely proportional to the number of size sections due to double integrals in the coagulation terms. Therefore, the degrees are kept low to maintain computational efficiency. To produce the same accuracy by using numerical integration with n size sections as by using the quadrature with the degree of 4 for the PL distribution, with the values of α and d where the quadrature is applicable, about 1 or 2 orders of magnitude longer computing time is consumed. The degree for the Hermite-Gauss quadrature, $n = 5$, can be increased easily without encountering steep increases to computing time; nevertheless, in the cases of this article, $n = 5$ produces the absolute relative errors of less than 10^{-4} for the condensation and the coagulation terms.

Acknowledgements. This work was funded by the Maj and Tor Nessling Foundation (project number 2014452), by Tampere University of Technology Graduate School, and by the Finnish Funding Agency for Technology and Innovation (Tekes) as a part of the CLEEN MMEA program. Authors acknowledge the personal of the Air Protection Group at the Helsinki Region Environmental Services Authority (HSY) for enabling the measurement campaign at the HSY's street canyon measurement site in Helsinki.

References

Adams, P. and Seinfeld, J.: Predicting global aerosol size distributions in general circulation models, J. Geophys. Res.-Atmos., 107, AAC 4–1–AAC 4–23, doi:10.1029/2001JD001010, 2002.

Barrett, J. and Webb, N.: A comparison of some approximate methods for solving the aerosol general dynamic equation, J. Aerosol Sci., 29, 31–39, doi:10.1016/S0021-8502(97)00455-2, 1998.

Dahneke, B.: Simple kinetic theory of Brownian diffusion in vapors and aerosols, in: Theory of Dispersed Multiphase Flow, edited by Meyer, R. E., pp. 97–133, Academic Press, doi:10.1016/B978-0-12-493120-6.50011-8, 1983.

Friedlander, S. K.: Smoke, dust, and haze: Fundamentals of aerosol dynamics, Oxford University Press, New York, USA, 2nd edn., 2000.

Hinds, W. C.: Aerosol technology: properties, behavior, and measurement of airborne particles, John Wiley & Sons, Inc., Hoboken, USA, 2nd edn., 1999.

Hussein, T., Hruška, A., Dohányosová, P., Džumbová, L., Hemerka, J., Kulmala, M., and Smolík, J.: Deposition rates on smooth surfaces and coagulation of aerosol particles inside a test chamber, Atmos. Environ., 43, 905–914, doi:10.1016/j.atmosenv.2008.10.059, 2009.

Jacobson, M.: Development and application of a new air pollution modeling system–II. Aerosol module structure and design, Atmos. Environ., 31, 131–144, doi:10.1016/1352-2310(96)00202-6, 1997.

Kannosto, J., Virtanen, A., Lemmetty, M., Mäkelä, J. M., Keskinen, J., Junninen, H., Hussein, T., Aalto, P., and Kulmala, M.: Mode resolved density of atmospheric aerosol particles, Atmos. Chem. Phys., 8, 5327–5337, doi:10.5194/acp-8-5327-2008, 2008.

Kerminen, V.-M. and Kulmala, M.: Analytical formulae connecting the "real" and the "apparent" nucleation rate and the nuclei number concentration for atmospheric nucleation events, J. Aerosol Sci., 33, 609–622, doi:10.1016/S0021-8502(01)00194-X, 2002.

Kulmala, M., Vehkamäki, H., Petäjä, T., Maso, M. D., Lauri, A., Kerminen, V.-M., Birmili, W., and McMurry, P.: Formation and growth rates of ultrafine atmospheric particles: a review of observations, J. Aerosol Sci., 35, 143–176, doi:10.1016/j.jaerosci.2003.10.003, 2004.

Kulmala, M., Riipinen, I., Sipilä, M., Manninen, H. E., Petäjä, T., Junninen, H., Dal Maso, M., Mordas, G., Mirme, A., Vana, M., Hirsikko, A., Laakso, L., Harrison, R. M., Hanson, I., Leung, C., Lehtinen, K. E. J., and Kerminen, V.-M.: Toward direct measurement of atmospheric nucleation, Science, 318, 89–92, doi:10.1126/science.1144124, 2007.

Kulmala, M., Kontkanen, J., Junninen, H., Lehtipalo, K., Manninen, H., Nieminen, T., Petäjä, T., Sipilä, M., Schobesberger, S., Rantala, P., Franchin, A., Jokinen, T., Järvinen, E., Äijälä, M., Kangasluoma, J., Hakala, J., Aalto, P., Paasonen, P., Mikkilä, J., Vanhanen, J., Aalto, J., Hakola, H., Makkonen, U., Ruuskanen, T., Mauldin III, R., Duplissy, J., Vehkamäki, H., Bäck, J., Kortelainen, A., Riipinen, I., Kurtén, T., Johnston, M., Smith, J., Ehn, M., Mentel, T., Lehtinen, K., Laaksonen, A., Kerminen, V.-M., and Worsnop, D.: Direct observations of atmospheric aerosol nucleation, Science, 339, 943–946, doi:10.1126/science.1227385, 2013.

Lai, A. and Nazaroff, W.: Modeling indoor particle deposition from turbulent flow onto smooth surfaces, J. Aerosol Sci., 31, 463–476, doi:10.1016/S0021-8502(99)00536-4, 2000.

Lehtinen, K. E. J. and Kulmala, M.: A model for particle formation and growth in the atmosphere with molecular resolution in size, Atmos. Chem. Phys., 3, 251–257, doi:10.5194/acp-3-251-2003, 2003.

Lehtinen, K. E. J., Dal Maso, M., Kulmala, M., and Kerminen, V.-M.: Estimating nucleation rates from apparent particle formation rates and vice versa: Revised formulation of the Kerminen-Kulmala equation, J. Aerosol Sci., 38, 988–994, doi:10.1016/j.jaerosci.2007.06.009, 2007.

McGraw, R.: Description of aerosol dynamics by the quadrature method of moments, Aerosol Sci. Tech., 27, 255–265, doi:10.1080/02786829708965471, 1997.

Mitrakos, D., Hinis, E., and Housiadas, C.: Sectional modeling of aerosol dynamics in multi-dimensional flows, Aerosol Sci. Tech., 41, 1076–1088, doi:10.1080/02786820701697804, 2007.

Mordas, G., Manninen, H., Petäjä, T., Aalto, P., Hämeri, K., and Kulmala, M.: On operation of the ultra-fine water-based CPC TSI 3786 and comparison with other TSI models (TSI 3776, TSI 3772, TSI 3025, TSI 3010, TSI 3007), Aerosol Sci. Tech., 42, 152–158, doi:10.1080/02786820701846252, 2008.

Olin, M., Rönkkö, T., and Dal Maso, M.: CFD modeling of a vehicle exhaust laboratory sampling system: sulfur-driven nucleation and growth in diluting diesel exhaust, Atmos. Chem. Phys., 15, 5305–5323, doi:10.5194/acp-15-5305-2015, 2015.

Riipinen, I., Sihto, S.-L., Kulmala, M., Arnold, F., Dal Maso, M., Birmili, W., Saarnio, K., Teinilä, K., Kerminen, V.-M., Laaksonen, A., and Lehtinen, K. E. J.: Connections between atmospheric sulphuric acid and new particle formation during QUEST III–IV campaigns in Heidelberg and Hyytiälä, Atmos. Chem. Phys., 7, 1899–1914, doi:10.5194/acp-7-1899-2007, 2007.

Rönkkö, T., Virtanen, A., Vaaraslahti, K., Keskinen, J., Pirjola, L., and Lappi, M.: Effect of dilution conditions and driving parameters on nucleation mode particles in diesel exhaust: Laboratory and on-road study, Atmos. Environ., 40, 2893–2901, doi:10.1016/j.atmosenv.2006.01.002, 2006.

Rönkkö, T., Lähde, T., Heikkilä, J., Pirjola, L., Bauschke, U., Arnold, F., Schlager, H., Rothe, D., Yli-Ojanperä, J., and Keskinen, J.: Effects of gaseous sulphuric acid on diesel exhaust nanoparticle formation and characteristics, Environ. Sci. Technol., 47, 11 882–11 889, doi:10.1021/es402354y, 2013.

Seinfeld, J. and Pandis, S.: Atmospheric chemistry and physics: From air pollution to climate change, John Wiley and Sons, Inc., New York, USA, 2nd edn., 2006.

Sihto, S.-L., Kulmala, M., Kerminen, V.-M., Dal Maso, M., Petäjä, T., Riipinen, I., Korhonen, H., Arnold, F., Janson, R., Boy, M., Laaksonen, A., and Lehtinen, K. E. J.: Atmospheric sulphuric acid and aerosol formation: implications from atmospheric measurements for nucleation and early growth mechanisms, Atmos. Chem. Phys., 6, 4079–4091, doi:10.5194/acp-6-4079-2006, 2006.

Steen, N., Byrne, G., and Gelbard, E.: Gaussian quadratures for the integrals $\int_0^\infty \exp(-x^2) f(x) dx$ and $\int_0^b \exp(-x^2) f(x) dx$, Math. Comp., 23, 661–671, 1969.

Tammet, H. and Kulmala, M.: Performance of four-parameter analytical models of atmospheric aerosol particle size distribution, J. Aerosol Sci., 77, 145 – 157, doi:10.1016/j.jaerosci.2014.08.001, 2014.

Uhrner, U., von Löwis, S., Vehkamäki, H., Wehner, B., Bräsel, S., Hermann, M., Stratmann, F., Kulmala, M., and Wiedensohler, A.: Dilution and aerosol dynamics within a diesel car exhaust plume-CFD simulations of on-road measurement conditions, Atmos. Environ., 41, 7440–7461, doi:10.1016/j.atmosenv.2007.05.057, 2007.

Vanhanen, J., Mikkilä, J., Lehtipalo, K., Sipilä, M., Manninen, H. E., Siivola, E., Petäjä, T., and Kulmala, M.: Particle size magnifier for nano-CN detection, Aerosol Sci. Tech., 45, 533–542, doi:10.1080/02786826.2010.547889, 2011.

Verheggen, B. and Mozurkewich, M.: An inverse modeling procedure to determine particle growth and nucleation rates from measured aerosol size distributions, Atmos. Chem. Phys., 6, 2927–2942, doi:10.5194/acp-6-2927-2006, 2006.

Wang, Y. and Zhang, K.: Coupled turbulence and aerosol dynamics modeling of vehicle exhaust plumes using the CTAG model, Atmos. Environ., 59, 284–293, doi:10.1016/j.atmosenv.2012.04.062, 2012.

Whitby, E. and McMurry, P.: Modal aerosol dynamics modeling, Aerosol Sci. Tech., 27, 673–688, doi:10.1080/02786829708965504, 1997.

Wu, C.-Y. and Biswas, P.: Study of numerical diffusion in a discrete-sectional model and its application to aerosol dynamics simulation, Aerosol Sci. Tech., 29, 359–378, doi:10.1080/02786829808965576, 1998.

Table 1. Input parameters for the test cases. Case names with Atm have the parameter sets related to atmospheric particle formation and the Exh case related to particle formation ~~occurred~~ occurring in vehicle exhaust. J and ~~$g(t)$~~ g are the new particle formation rate and the condensational growth rate, respectively. N_{bg} is the concentration of the background aerosol distribution having a count median diameter of $\mathrm{CMD}_{\mathrm{bg}}$. The coagulational loss exponent l_{bg} depend on the value of $\mathrm{CMD}_{\mathrm{bg}}$. Wall deposition is modelled using the deposition coefficient k_{dep}. The length of the simulated time domain is t_{max}.

Case	J ($\mathrm{cm^{-3}\,s^{-1}}$)	g	T (K)	Coagulation	N_{bg} ($\mathrm{cm^{-3}}$)	$\mathrm{CMD}_{\mathrm{bg}}$ (nm)	l_{bg}	k_{dep}	γ	t_{max}
Atm1	0.1	$1\,\mathrm{nm\,h^{-1}}$	280	intra, inter	0	–	–	0	0	5 h
Atm2	0.1	$1\,\mathrm{nm\,h^{-1}}$	280	intra, inter	0	–	–	$1.8\,\mathrm{nm\,h^{-1}}$	0	5 h
Atm3	0.1	$1\,\mathrm{nm\,h^{-1}}$	280	intra, inter, bg	10^3	100	-1.6	$1.8\,\mathrm{nm\,h^{-1}}$	0	5 h
Atm4	Eq. (50)	$1\,\mathrm{nm\,h^{-1}}$	280	intra, inter, bg	10^3	100	-1.6	$1.8\,\mathrm{nm\,h^{-1}}$	0	5 h
Atm5	Eq. (50)	Eqs. (16) – (18)	280	intra, inter, bg	10^3	100	-1.6	$1.8\,\mathrm{nm\,h^{-1}}$	0.25	5 h
Exh	10^8	$5\,\mathrm{nm\,s^{-1}}$	500	intra, inter, bg	10^6	60	-1.5	$0.07\,\mathrm{nm\,s^{-1}}$	0	1 s

Table 2. Relative errors, δ_X (%), of the variables ~~in~~ at the ends of the test ~~cases~~ case simulations using the PL+LN model compared to the variables produced by the fixed-sectional model with 1000 size sections. The input parameter sets are shown in Tab. 1. N, S, and M are the number, the surface area, and the mass concentration of the total particle distribution, respectively. GMD and GSD are the geometric mean diameter and the geometric standard deviation of the distribution.

Case	N	S	M	GMD	GSD
Atm1	-0.001	~~-0.312~~ -0.310	~~-0.574~~ -0.573	~~+0.067~~ 0.068	~~-0.195~~ -0.193
Atm2	~~-0.056~~ -0.052	~~-0.482~~ -0.481	-0.838	~~-0.080~~ -0.083	~~-0.036~~ -0.039
Atm3	~~+0.182~~ 0.173	~~-0.868~~ -0.884	~~-1.286~~ -1.296	~~-0.085~~ -0.086	~~-0.497~~ -0.505
Atm4	~~+0.037~~ 0.202	~~-0.845~~ -0.816	~~-1.526~~ -1.518	~~+1.716~~ 0.933	~~-2.143~~ -1.251
Atm5	+6.957	-2.384	-7.666	-3.511	-2.879
Exh	~~-0.347~~ +0.007	~~-0.705~~ -0.356	~~-0.982~~ -0.680	~~+0.011~~ 0.084	~~-0.213~~ +0.011

Table 3. Computational costs of different models and relative errors of ~~different models using~~ number (N) and mass (M) concentrations obtained from the time of 1663 s after the UV lights were switched on in the chamber ~~data~~simulation. The number of variables compared to size sections in MC models is ~~twofold~~ 2-fold because the centers of the size sections need to be stored in addition to the ~~concentration in~~ concentrations of the sections. Relative ~~numbers~~ values are calculated using a model with (ref.) as the reference model.~~Number (N) and mass (M) concentrations are obtained from the time of 1663after the UV lights switched on.~~

Model name	Method	Size sections	Variables	Relative computing time	Error in N (%)	Error in M (%)
~~FS24~~ FS35	fixed-sectional	~~24~~ 35	~~24~~ 35	1.0	+~~0.78~~ 1.6	+~~135~~ 79
~~MC6~~ MC10	moving-center	~~6~~ 10	~~12~~ 20	~~1.6~~ 1.0	+~~26.4~~ 18	+~~59.0~~ 29
LN	log-normal	-	3	~~0.11~~ 0.09	+~~9.87~~ 17	+~~7.40~~ 6.4
PL+LN	combined PL and LN	-	6	~~1~~ 1.0 (ref.)	+~~1.14~~ 0.48	~~-0.34~~ -1.2
~~FS720~~ FS400	fixed-sectional	~~720~~ 400	~~720~~ 400	~~2000~~ 170	0 (ref.)	+~~1.63~~ 3.4
MC100	moving-center	100	200	~~100~~ 200	+~~0.28~~ 0.31	0 (ref.)

Table 4. Relative errors (%) of the variables in the chamber simulation with the PL+LN model using different values for the condensational transfer factor γ. The errors are compared to the ~~FS720~~ FS400 model, except for M that is compared to the MC100 model.

γ	N	M	GMD	GSD
0.1	~~-5.64~~ -1.2	~~-5.81~~ -7.8	+~~4.40~~ 2.6	~~-3.38~~ -5.8
0.5	~~-1.09~~ +0.75	~~-1.75~~ -2.7	~~-0.53~~ -3.7	~~-0.06~~ +3.4
0.8	+~~1.14~~ 0.48	~~-0.34~~ -1.2	~~+1.00~~ -0.33	~~-2.37~~ -2.8
0.9	+~~3.03~~ 2.6	~~+1.26~~ -0.43	~~-0.22~~ -0.11	~~-2.65~~ -6.0

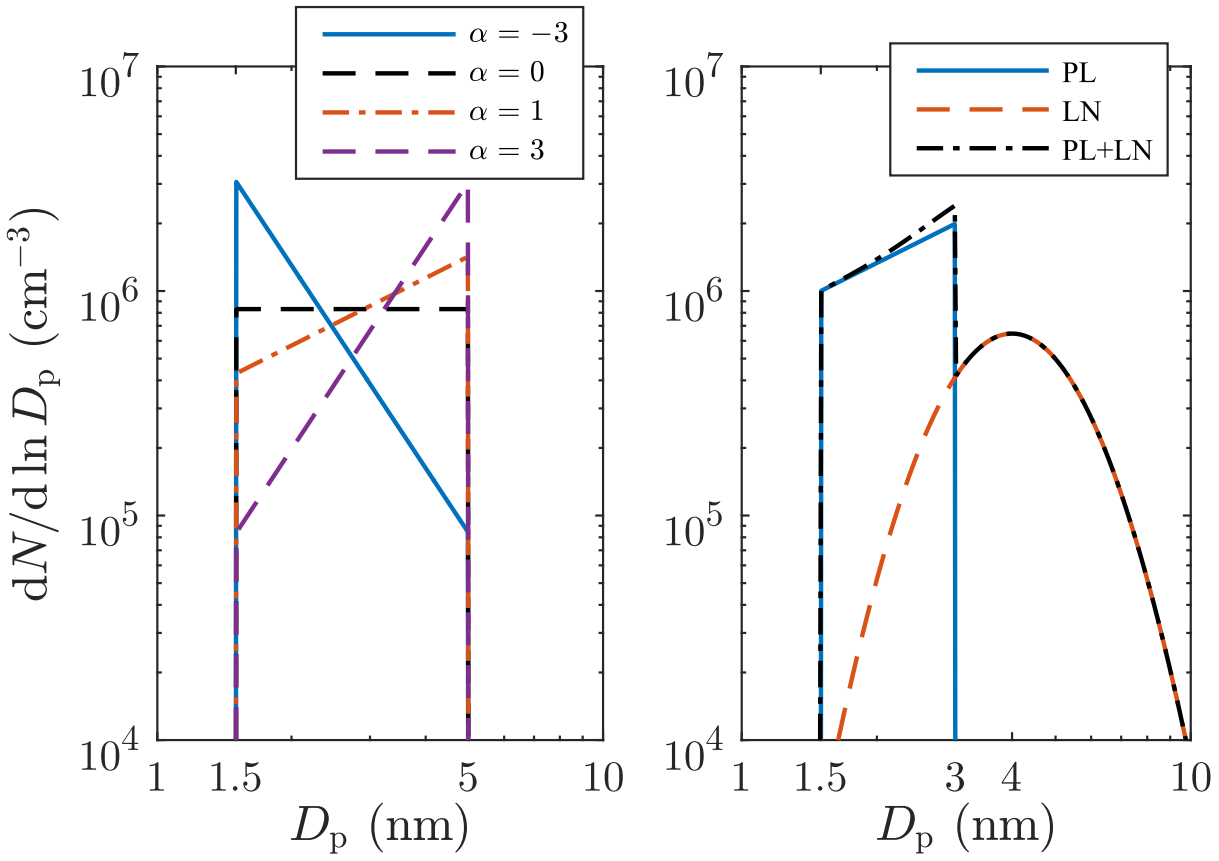

Figure 1. Left pane shows examples of power law distributions with different values of the slope parameter α. Right pane shows the combination of a power law (PL) and a log-normal (LN) distribution (PL+LN).

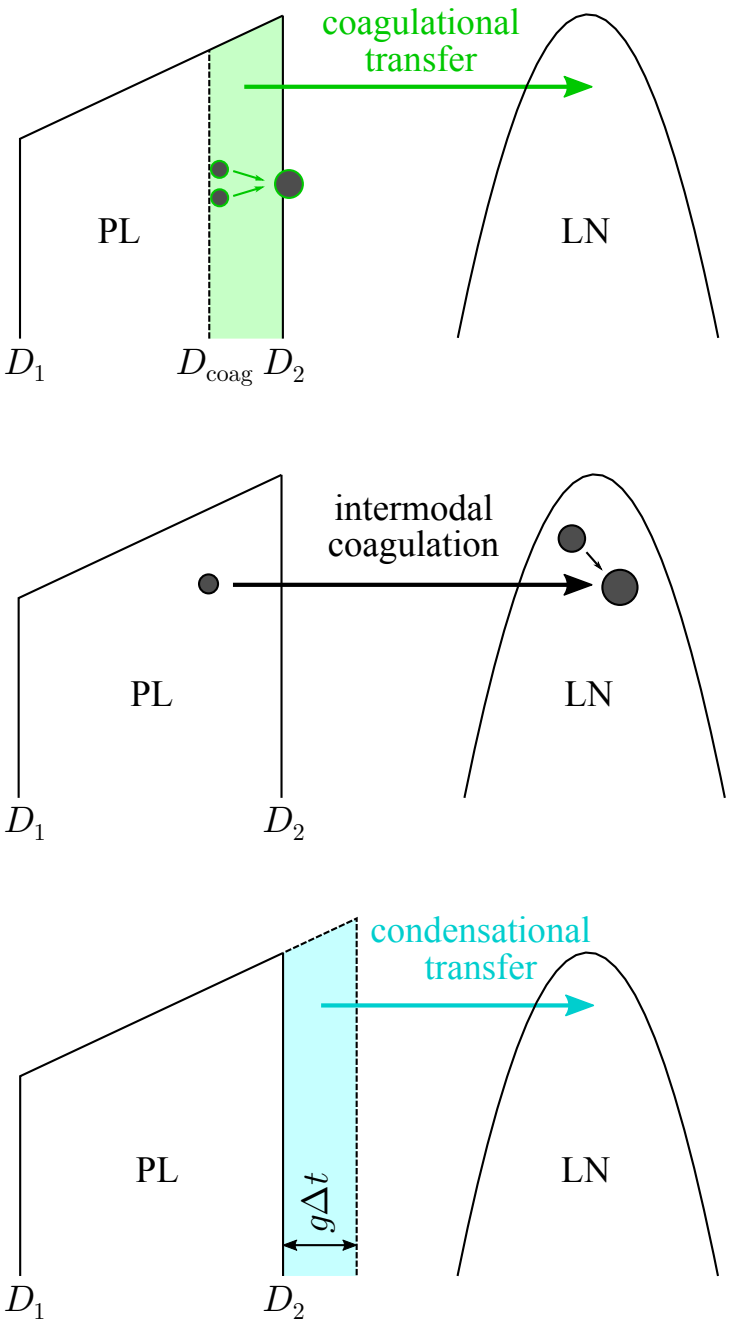

Figure 2. Intermodal processes between the PL and the LN distributions. Particles larger than D_{coag} (green area) form particles larger than D_2 by the intramodal coagulation in the PL distribution; the coalesced resultant particles are transferred to the LN distribution. When the LN distribution exists, particles of the both distributions begin to coagulate intermodally; the resultant particles are assigned to the LN distribution. Condensation grows the largest particle diameter by $g\Delta t$ in a time step of Δt, but the condensational transfer transfers a part of the particles larger than D_2 (blue area) to the LN distribution.

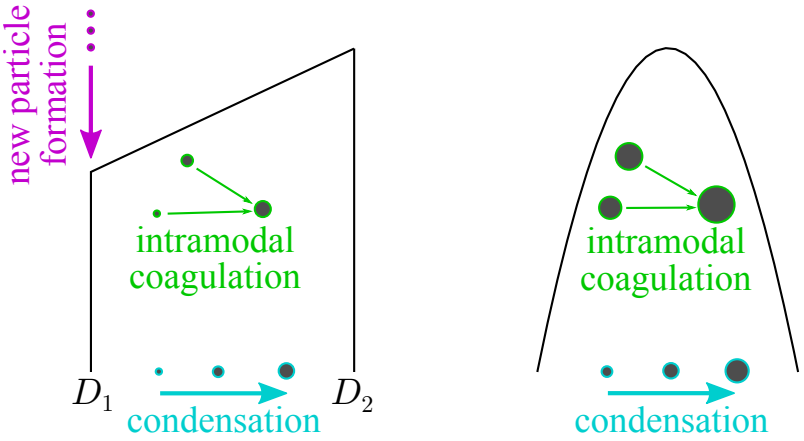

Figure 3. Intramodal processes. New particle formation forms particles with the diameter of D_1 to the PL distribution. Condensation and intramodal coagulation grow particles within a distribution.

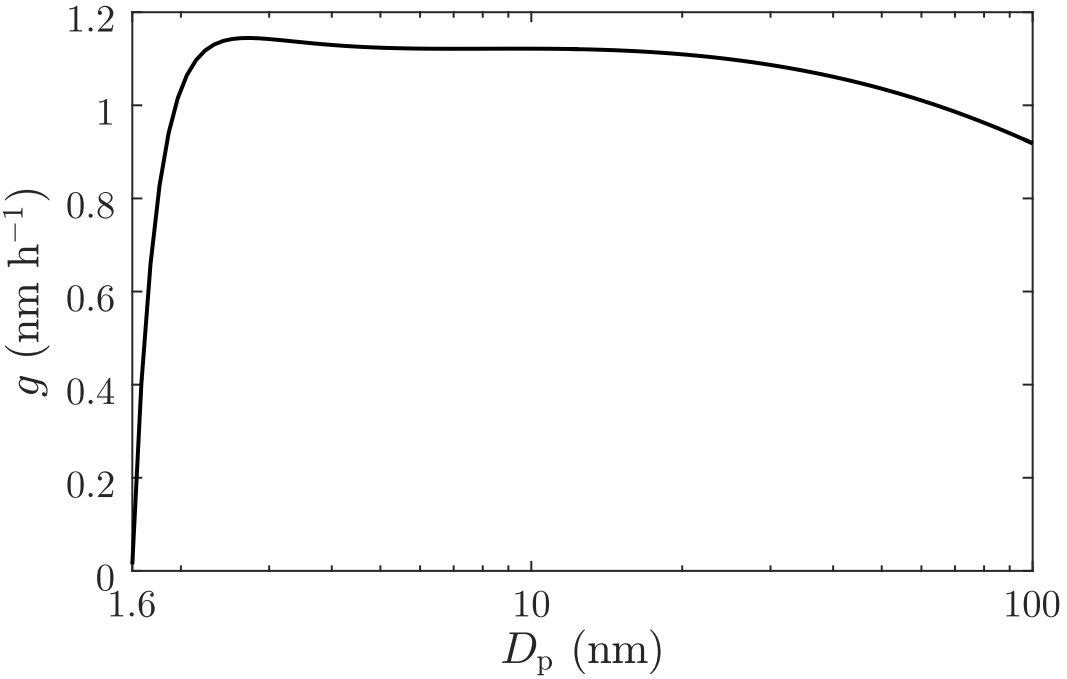

Figure 4. ~~Contour plots~~ Size-dependent condensational growth rate of ~~particle distributions measured by PSM~~sulfuric acid-water particles with the sulfuric acid vapor concentration of 0.8×10^7 cm^{-3}, ~~CPC~~temperature of 280 K, and ~~Nano-SMPS and simulated by different models. FS720 denotes~~ relative humidity of 60 % as a function of the ~~fixed-sectional model with 720 size sections~~particle diameter, used in the Atm5 case.~~Note that~~

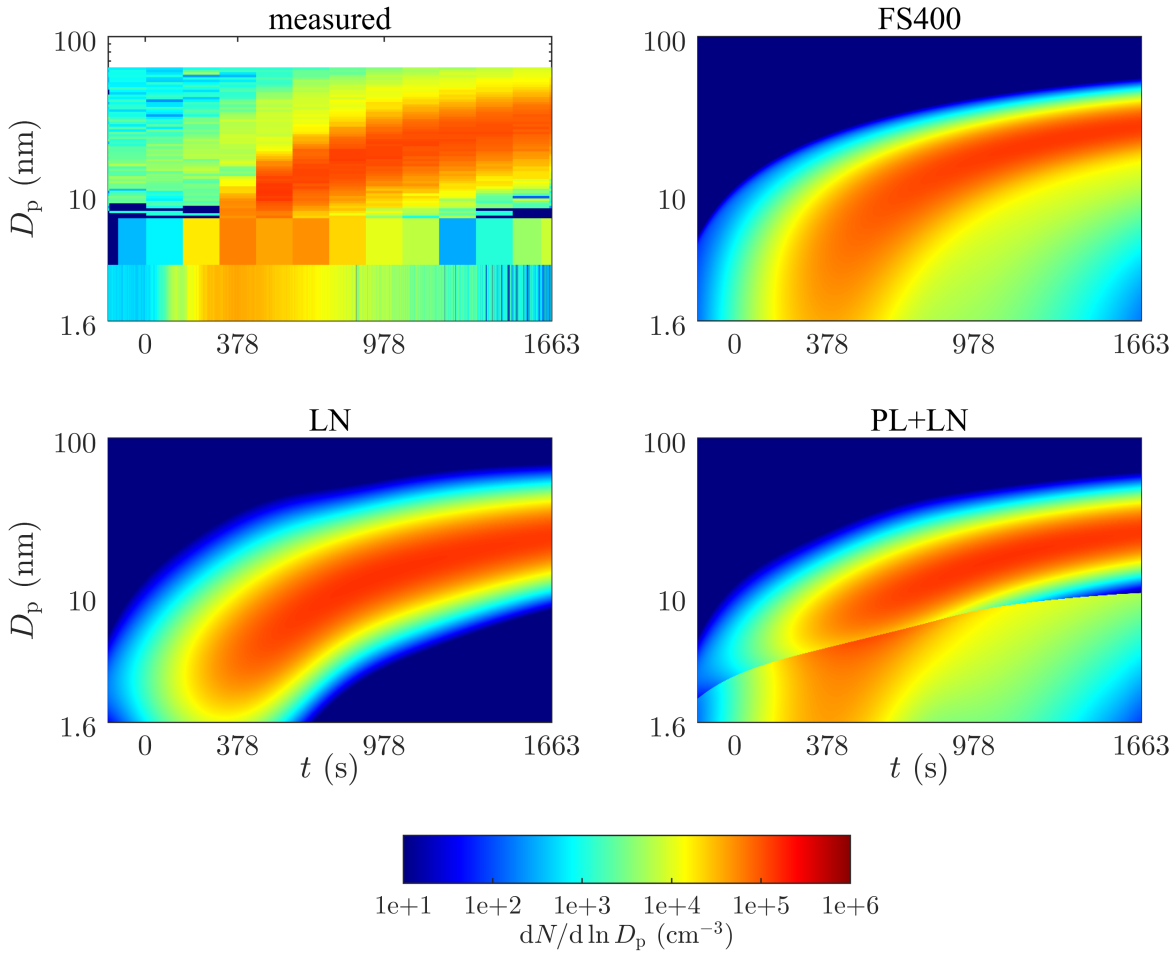

Figure 5. Contour plots of particle distributions measured by PSM, CPC, and Nano-SMPS and simulated by different models in the chamber event. FS400 denotes the fixed-sectional model with 400 size sections. The value of 0.8 was used for γ with the PL+LN model. The UV lights were switched on at time $t = 0\,\mathrm{s}$. Note that the background particle distribution seen in the measured data was excluded from the simulations.

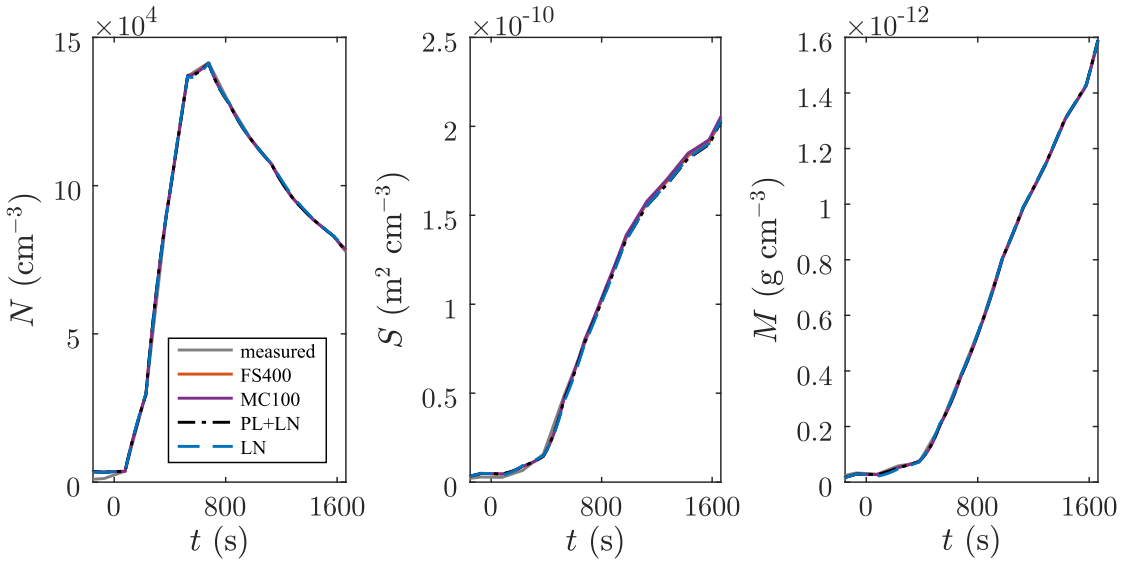

Figure 6. Number (N), surface area (S), and mass (M) concentrations of the ~~background particle distribution seen~~ nucleation mode in the chamber event. The measured ~~data was excluded from~~ concentrations and the ~~simulations~~concentrations produced during inverse modelling using different models are nearly equal. The ~~vertical lines at 528indicate~~ data are shown for the ~~time~~ centers of the ~~center of a~~ Nano-SMPS ~~scan for which the distributions~~ scans only, because those values only are ~~plotted also~~ used in ~~Fig~~inverse modelling. ~~12~~MC100 denotes the moving-center fixed-sectional model with 100 size sections.

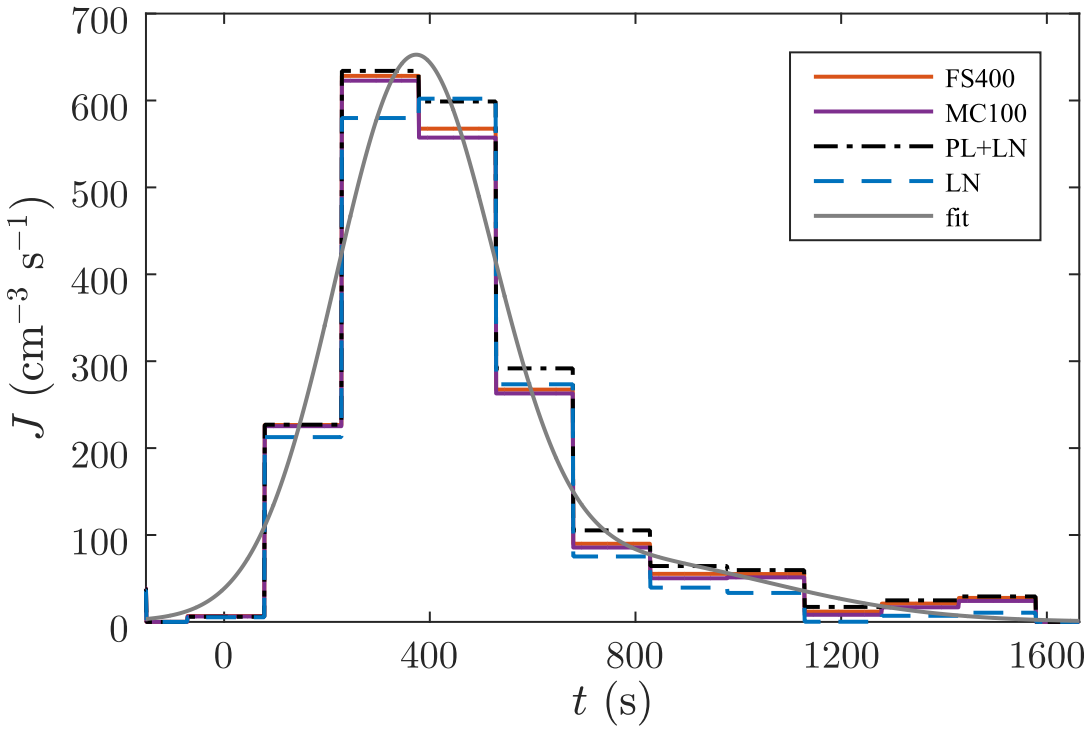

Figure 7. ~~The development of~~ Time series for the ~~nucleation mode~~ new particle ~~number concentration~~ formation rates in the chamber event ~~. PSM dots denote~~ that produce the measured ~~concentration (subtracted by the background aerosol concentration) and the others the simulated~~ concentrations~~. Concentrations from all the models except MC6~~ , N, S, and ~~LN are nearly equal at~~ M, the ~~end of~~ most accurately compared to the ~~simulations~~measured ones, using different models. The ~~abbreviations are explained in Tab. 3~~fit denotes a bell-shaped function fitted to the values from the FS400 model.

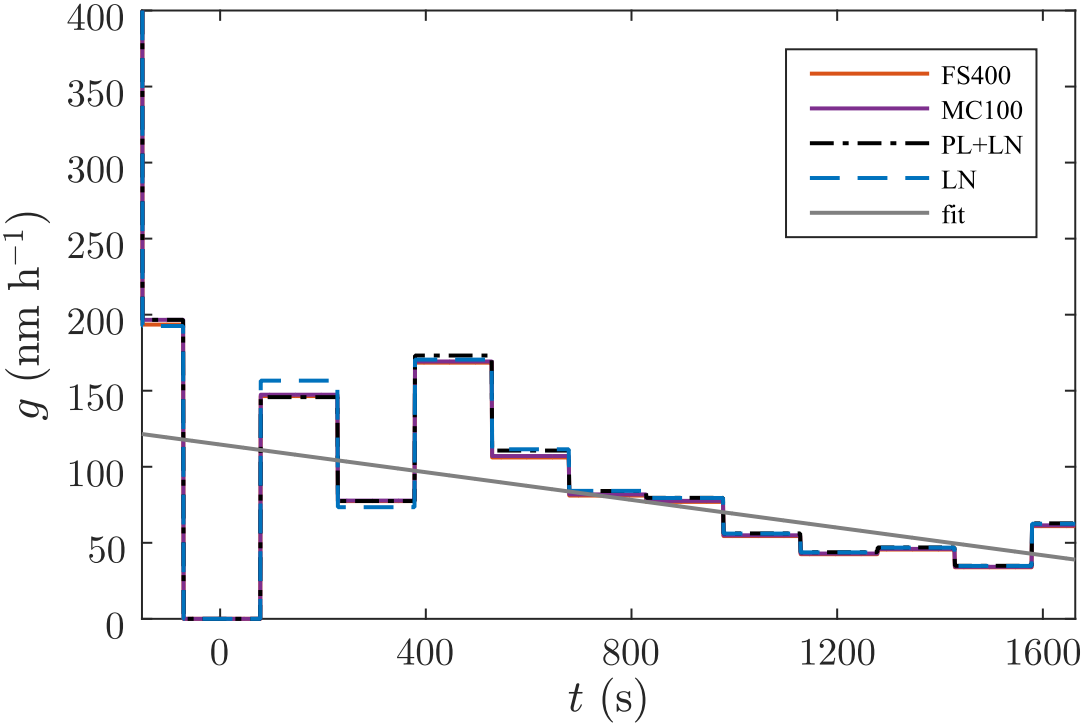

Figure 8. Time series for the condensational growth rates in the chamber event that produce the measured concentrations, N, S, and M, the most accurately compared to the measured ones, using different models. The fit denotes a linear function fitted to the values from the FS400 model.

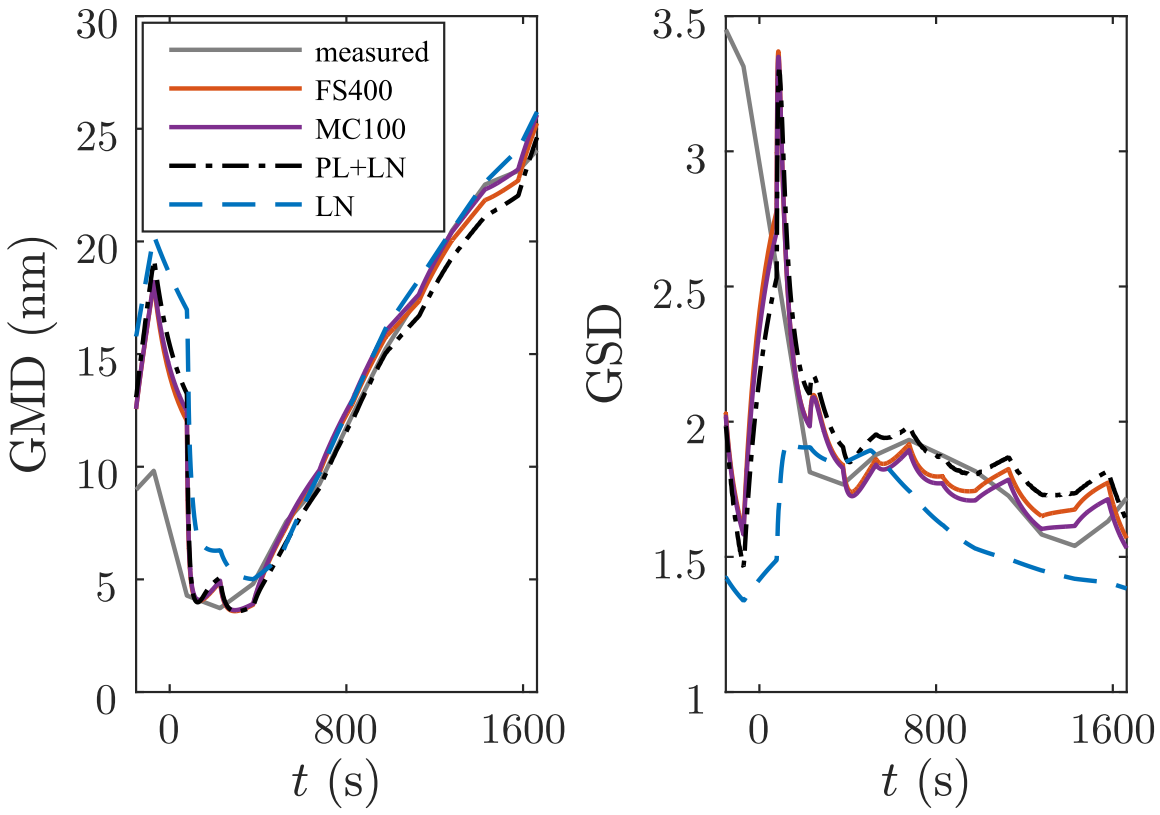

Figure 9. Geometric mean diameter (GMD) and geometric standard deviation (GSD) of the nucleation mode in the chamber event, obtained through inverse modelling, using different models.

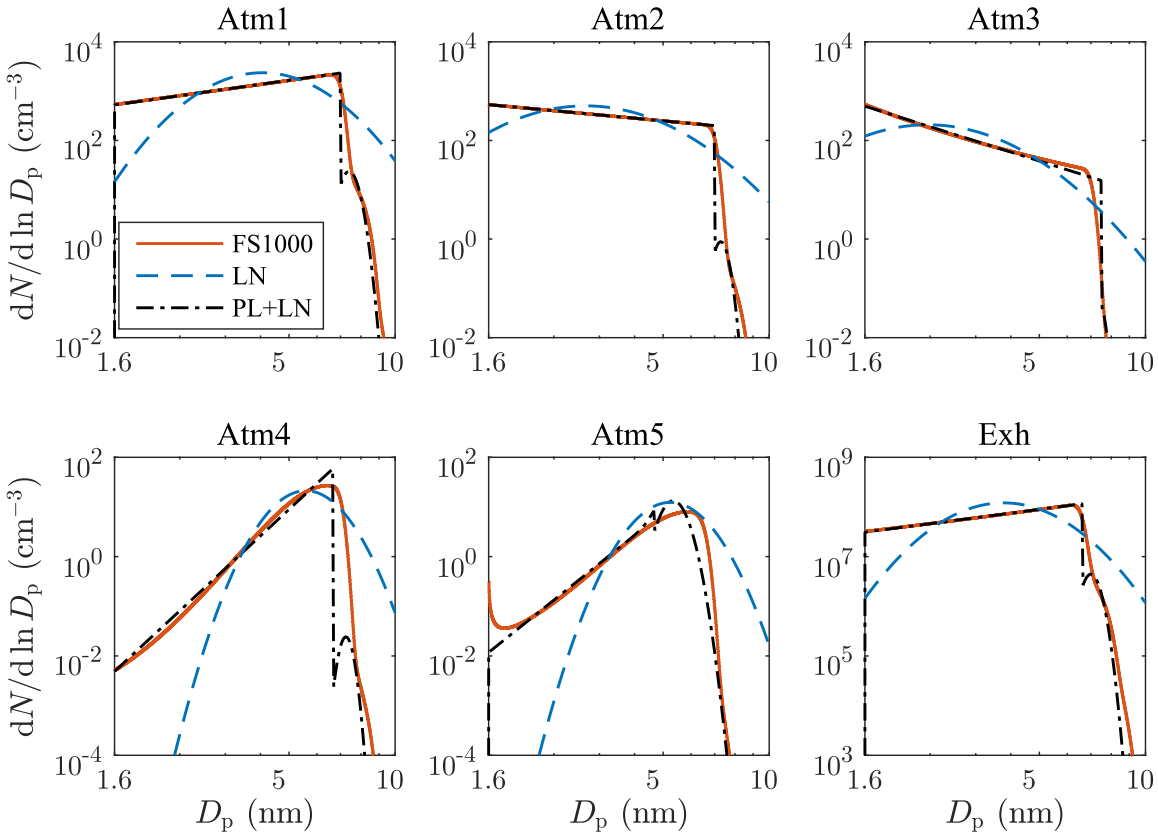

Figure 10. Particle size distributions at the ends of the test case simulations produced by different models. The input parameter sets are shown in Tab. 1. FS1000 denotes the fixed-sectional model with 1000 size sections. Note the different scales in the vertical axes on the bottom row.

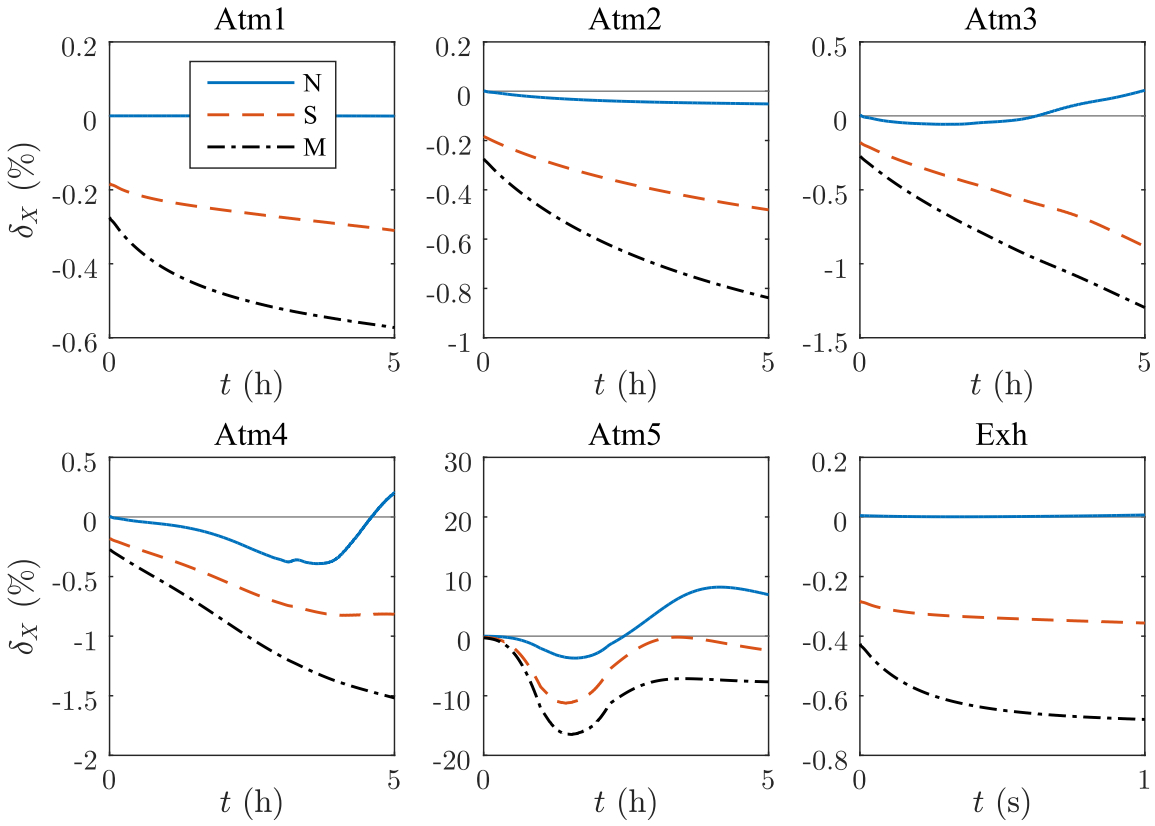

Figure 11. The ~~size distributions~~ relative errors of the moments (δ_X) in the test cases produced by ~~different models~~the PL+LN model. The input parameter sets are shown in Tab. 1.~~FS1000 denotes the fixed-sectional model with 1000 size sections. Note the different scales in the vertical axes on the bottom row.~~

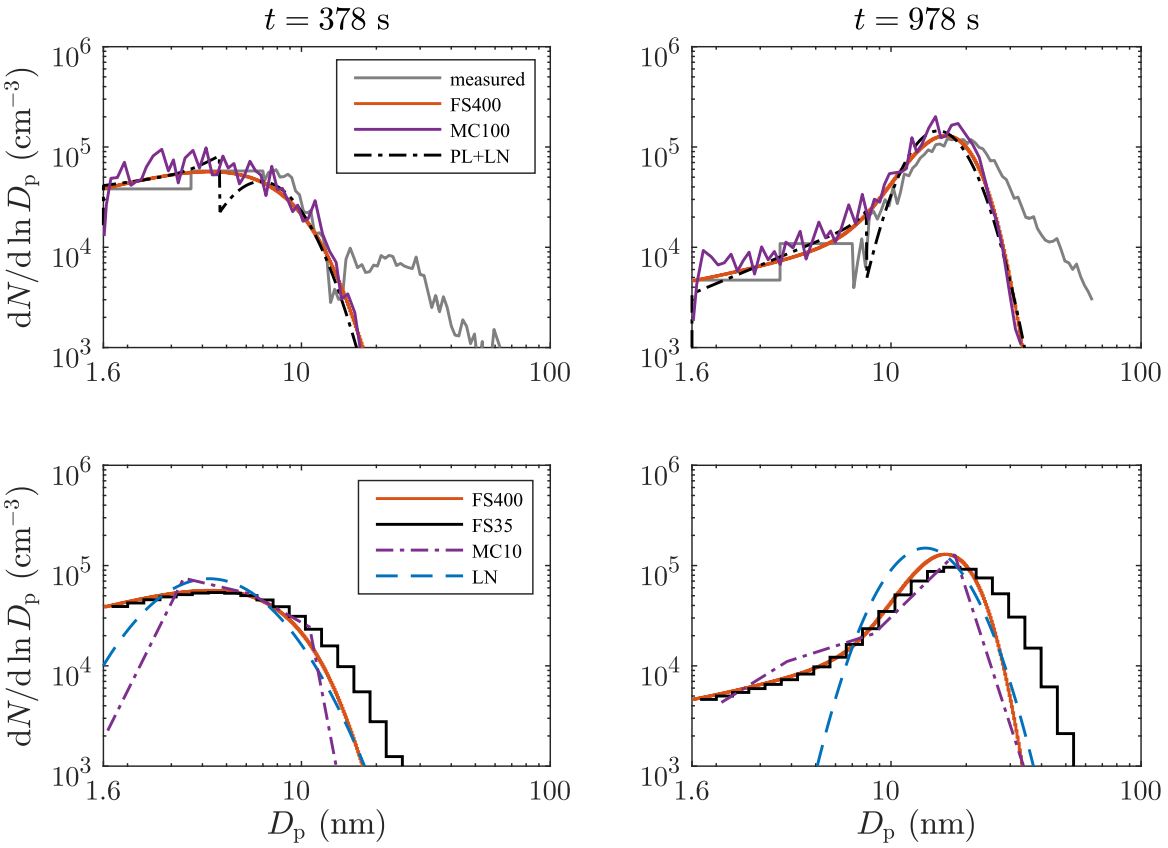

Figure 12. Particle size distributions in the chamber event ~~528~~378 and 978 s after the UV lights were switched on. The top row shows the accurate model outputs together with the measured distribution~~includes~~. The bottom row shows the less accurate model outputs together with the accurate FS400 model output. The measured distributions include also the background ~~mode~~ distributions around 30 and 50 nm which ~~was~~ were excluded from the simulations. The abbreviations are explained in Tab. 3.

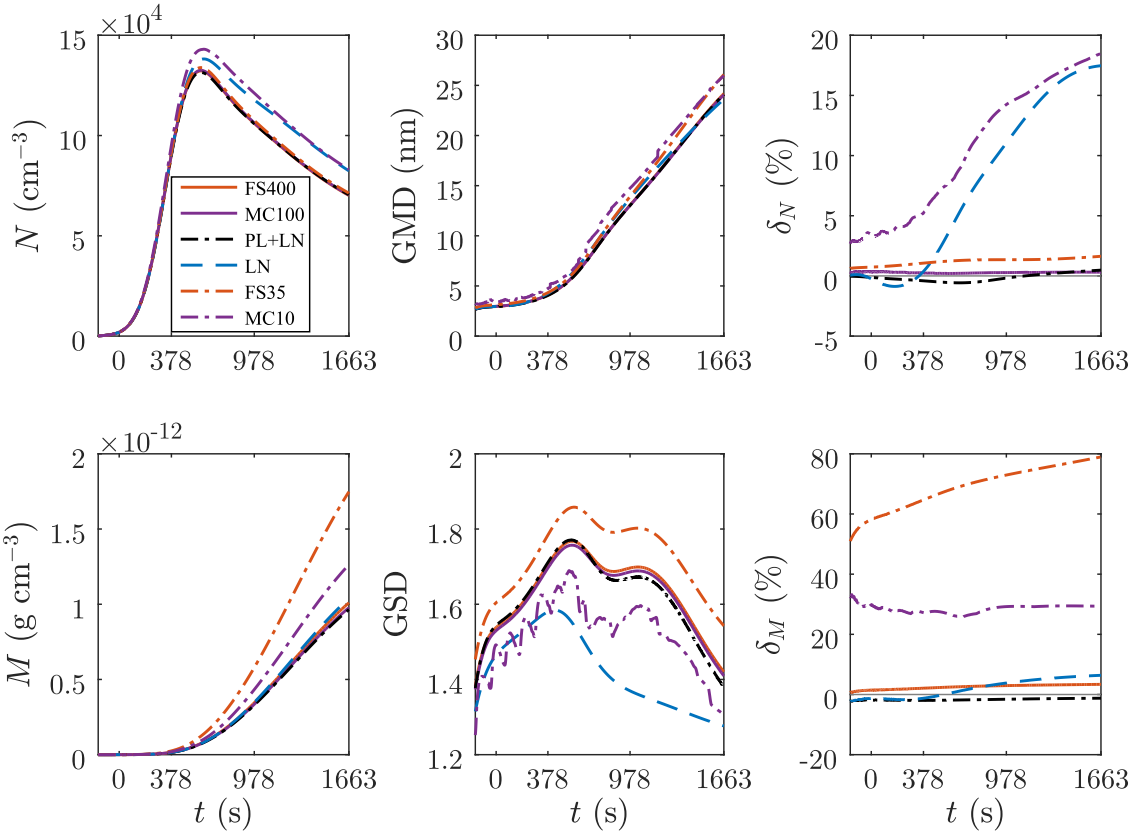

Figure 13. ~~The development~~ Number (N) and mass (M) concentrations, GMD, and GSD of the nucleation mode ~~geometric mean diameter~~ and the relative errors of the concentrations (δ_N and δ_M) in the chamber event~~simulation~~, produced by different models. The ~~values from all~~ outputs of the ~~models except FS24~~ FS400 and ~~MC6~~ the MC100 models are nearly equal~~at the end of the simulations. The abbreviations~~, and thus they are ~~explained in Tab. 3. The development of the nucleation mode geometric standard deviation~~ difficult to distinguish in the ~~chamber event simulation. The abbreviations are explained in Tab. 3~~figure.

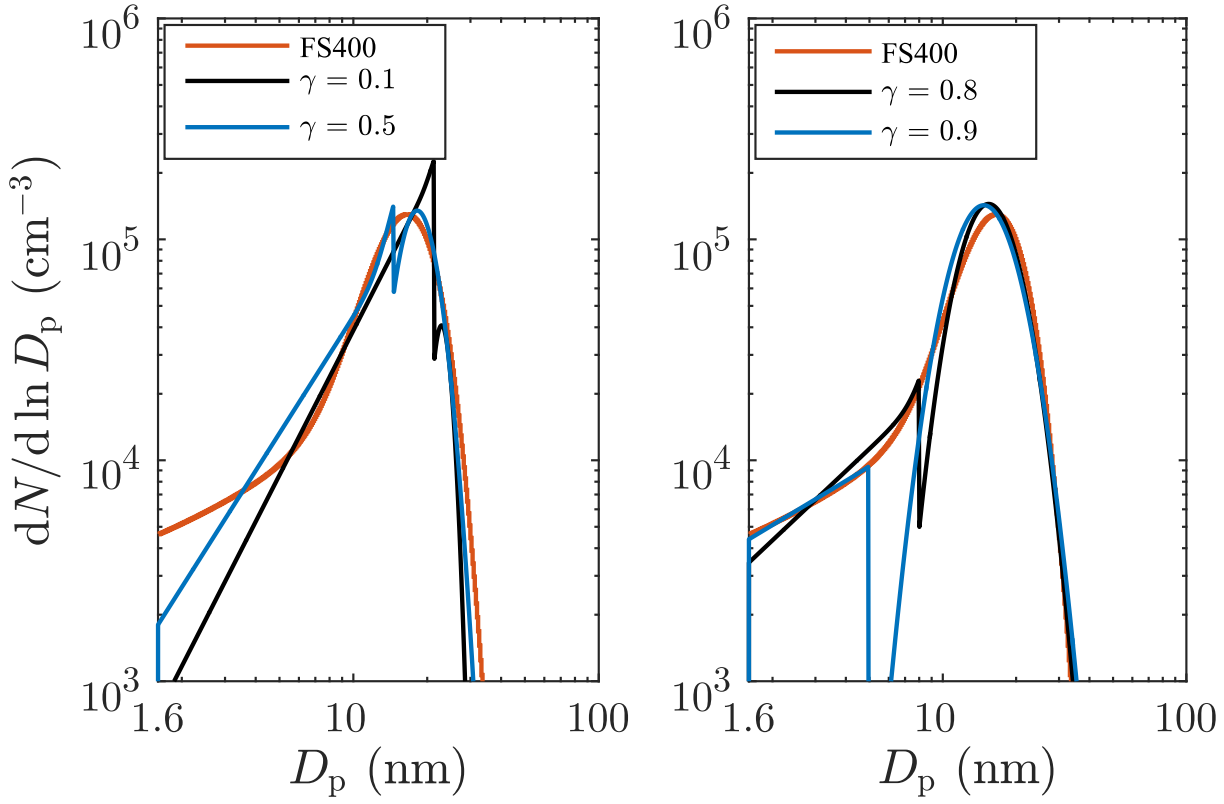

Figure 14. Particle size distributions ~~as in Fig. 12~~978 s after the UV lights were switched on, ~~but~~ with the different values for the condensational transfer factor γ using the PL+LN model compared to the FS400 model.

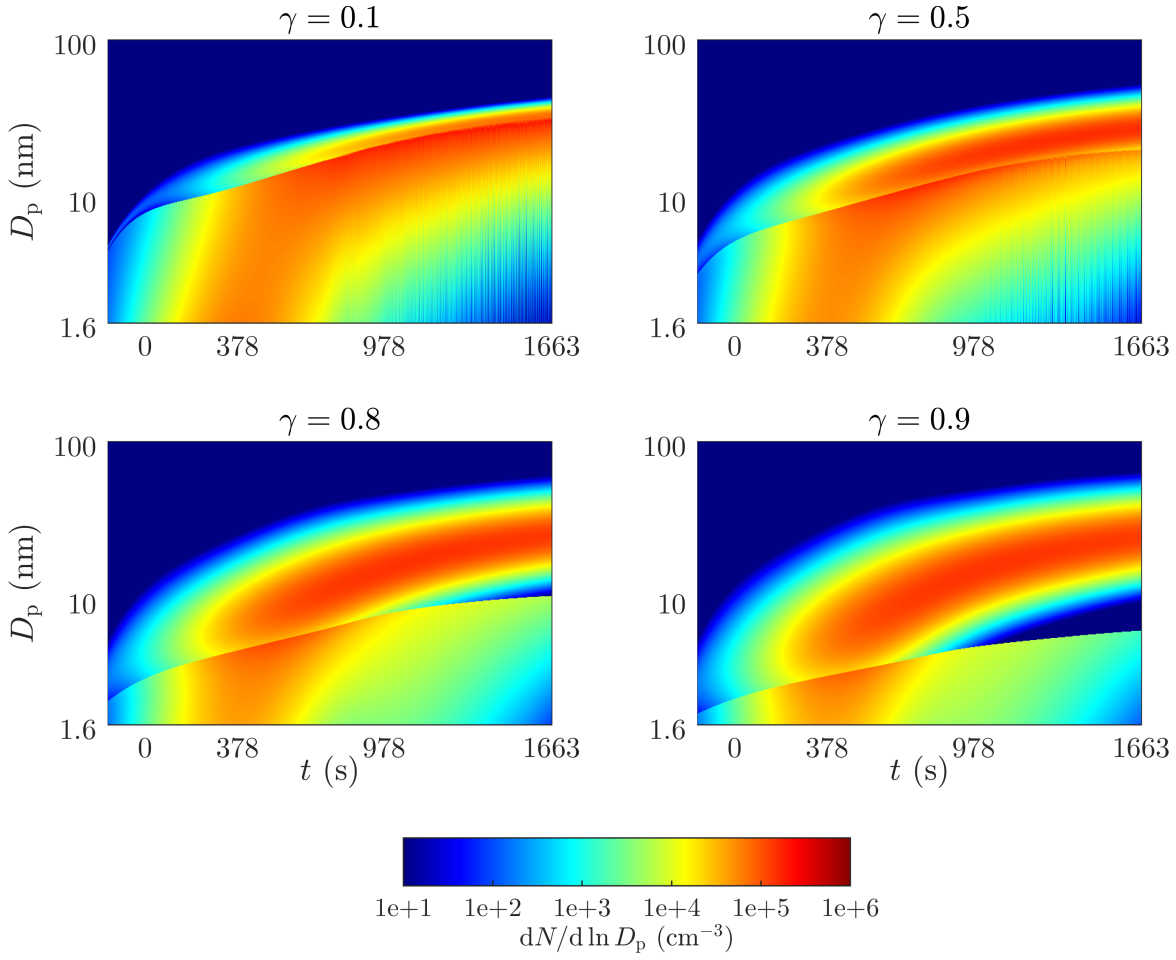

Figure 15. Contour plots of particle distributions simulated by the PL+LN models with different values of γ in the chamber event.

Using a combined power law and log-normal distribution model to simulate particle formation and growth in a mobile aerosol chamber

M. Olin, T. Anttila, and M. Dal Maso

Aerosol Physics Laboratory, Department of Physics, Tampere University of Technology, P.O. Box 692, 33101 Tampere, Finland

Correspondence to: M. Olin (miska.olin@tut.fi)

Abstract. We present the combined power law and log-normal distribution (PL+LN) model, a computationally efficient model to be used in simulations where the particle size distribution cannot be accurately represented by log-normal distributions, such as in simulations involving the initial steps of aerosol formation, where new particle formation and growth occur simultaneously, or in the case of inverse modelling. The model was evaluated against highly accurate sectional models using input parameter values that reflect conditions typical to particle formation occurring in the atmosphere and in vehicle exhaust, and tested in the simulation of a particle formation event performed in a mobile aerosol chamber at Mäkelänkatu street canyon measurement site in Helsinki, Finland. The number, surface area, and mass concentrations in the chamber simulation were conserved with the relative errors lower than 2 % using the PL+LN model, whereas a moment-based log-normal model and sectional models with the same computing time as with the PL+LN model caused relative errors up to 17 % and 79 %, respectively.

1 Introduction

Particle size distribution is the most important characteristic of nanoparticles, as it controls their deposition to the human respiratory system, their behavior in the atmosphere, and the properties of engineered nanoparticles. The rates of several aerosol processes, such as condensation, coagulation, and deposition, are affected by particle size; thus, the particle size distribution controls also the evolution of the aerosol. While the rates of the aerosol processes depend on the particle size, different particles within a particle size mode have different rates of aerosol processes and, thus, they evolve with different rates. This causes also the shape of the size distribution to evolve. Because particle size distributions usually contain particles with the diameters of several orders of magnitude rather than being monodisperse, i.e., equally sized, an accurate representation of aerosol properties and evolution requires that particle sizes are expressed as distributions. Due to a high count of particles with different sizes, shapes, and compositions within a volume of interest, computational costs to model them separately are extremely too high. Therefore, aerosol models typically model one or more parameter of the size distribution, such as particle number or mass concentration of the total particle size range or of several size ranges separately. Simplifications made for size distributions in aerosol models cause unrealistic shapes for the distributions.

Methods that model a particle size distribution the most realistically are sectional methods, in which the size distribution is split into separate size sections. The accuracy of a sectional model can be controlled by the number of the size sections. Increasing the number of sections increases accuracy, but the computational cost is also increased. In multidimensional simulations, such as in Computational Fluid Dynamics (CFD) and in climate simulations, computational efficiency is a key property of the model. Simulations involving inverse modelling (Verheggen and Mozurkewich, 2006), where the values of model input parameters (e.g., new particle formation rate or condensational growth rate) are varied systematically to find out the values that most exactly produce the measured results, may suffer from long computing times even in one-dimensional cases.

Sectional methods vary depending on the conserved property of the aerosol. Only a single property, e.g., particle number, particle surface area, or particle mass concentration, can be conserved in the simulation but other properties will suffer from numerical diffusion, which is seen as the overestimation of the non-conserved properties (Wu and Biswas, 1998). Less numerical diffusion can be obtained, e.g., by using a moving-center fixed-sectional method, in which size sections have fixed boundaries but the centers of the sections are allowed to vary so that number and mass concentrations are conserved better(Jacobson, 1997). However, implementing the moving-center fixed-sectional method in Eulerian simulation, such as in CFD simulation, with simultaneous new particle formation, condensation, coagulation, and transportation is challenging due to discontinuous behavior of the section variables (all particles of a section are transferred to an adjacent section when the center of a section exceeds a section boundary during growth), computationally time-consuming due to the transfer of the particles between the sections, and memory-consuming due to the requirement of storing also the center values of the sections. Wang and Zhang (2012) have modelled simultaneous new particle formation and growth within diesel exhaust plumes using the moving-center fixed-sectional method in three-dimensional CFD simulation and have obtained promising results for particle size distributions compared to the measured distributions with only 8 size sections in a particle diameter decade. However, they did not report comparison between their model and any highly accurate aerosol model; thus, the effect of numerical diffusion to their results is unknown. Another method to decrease numerical diffusion is the TwO-Moment Aerosol Sectional (TOMAS) model, in which both the number and the mass concentrations are stored for all size sections (Adams and Seinfeld, 2002). The TOMAS model provides conservation for both the number and the mass concentrations of the total distribution, but the memory consumption in multidimensional simulations can be too high due to a high number of variables to be stored in every computational cell.

Other approaches to model the particle size distribution are methods based on the moments of the distribution (Whitby and McMurry, 1997), which are both computationally efficient (Mitrakos et al., 2007) and have continuous behavior of the variables. The number of the conserved properties of the aerosol is controlled by the number of the modelled moments; e.g., conserving number, surface area, and mass concentrations can be obtained by modelling the corresponding three moments. The number of the variables being stored during the simulation is the number of the modelled moments, which is significantly less compared to sectional methods, in which the number of the variables can be several hundreds. The major drawback in the methods based on moments is that the size distribution needs to be presented with a pre-defined function, unless the quadrature-method of moments (QMOM, McGraw (1997)) is used. QMOM provides accurate results (Barrett and Webb, 1998) but the reconstruction of the distribution parameters from the moments is not unique (Mitrakos et al., 2007). The typical choice for the size distribution function is the log-normal distribution or the combination of several log-normal distributions. They correspond

well with many laboratory aerosols and aged aerosols, but during the initial steps of the formation and growth of aerosol the size distribution can differ significantly. For example, Tammet and Kulmala (2014) recommend two-power law for the size distribution of atmospheric aerosols measured at least in Northern Europe. Two-power law distribution has four parameters, which implies that four moments are required for the reconstruction of the parameters from the moments, if the distribution is modelled using the moment method. However, there is no analytical solution for the system of equations of the two-power law approach, and solving the system of equations with four variables numerically is computationally very expensive.

The general dynamic equation (GDE) for the number concentration of a size section j, with new particle formation and condensational growth without any other aerosol processes, is (Seinfeld and Pandis, 2006)

$$\frac{\mathrm{d}N_j}{\mathrm{d}t} = \begin{cases} J(t) - \frac{g(t,D_\mathrm{p})}{\Delta D_j} N_j, & j = 1 \\ \frac{g(t,D_\mathrm{p})}{\Delta D_{j-1}} N_{j-1} - \frac{g(t,D_\mathrm{p})}{\Delta D_j} N_j, & j > 1 \end{cases}, \tag{1}$$

where N_j and ΔD_j are the number concentration and the diameter width of the size section, respectively. $J(t)$ is new particle formation rate as a function of time t, and $g(t, D_\mathrm{p})$ is condensational growth rate $\frac{\mathrm{d}D_\mathrm{p}}{\mathrm{d}t}$, where D_p is the particle diameter. In the case of simultaneous new particle formation and condensation with time- and size-independent rates, the analytical solution for the GDE provides the particle size distribution

$$\frac{\mathrm{d}N}{\mathrm{d}\ln D_\mathrm{p}} = \begin{cases} \frac{J}{g} D_\mathrm{p}, & D_1 \le D_\mathrm{p} \le D_2 \\ 0, & \text{otherwise} \end{cases}, \tag{2}$$

where D_1 is the diameter of the newly formed particle (assumed constant) and D_2 is the largest diameter. Equation (2) is in the form of a power law where the power of D_p is unity. In a realistic particle formation process, $J(t)$ and $g(t, D_\mathrm{p})$ do not remain constants and other aerosol processes affect also; thus, the power of D_p can differ and log-normal features will appear in the distribution. Here, we present a method to express the particle size distribution as a combination of a power law and a log-normal distribution. This moment-based combined power law and log-normal distribution model was evaluated against highly accurate sectional models using theoretical test cases and a real-world case, which represents a simulation of a particle formation event occurred in a mobile aerosol chamber.

2 Model description

The combined power law (PL) and log-normal (LN) distribution model (PL+LN) is based on the sum of these distributions. The PL distribution handles the formation and the initial growth of new particles; the LN distribution represents the log-normal shape of the distribution and it is formed by coagulation and condensation from the PL distribution.

2.1 Particle size distributions

2.1.1 Power law distribution

The formulation of the PL distribution originates from Eq. (2), where the power of D_p is allowed to vary,

$$\left.\frac{\mathrm{d}N}{\mathrm{d}\ln D_\mathrm{p}}\right|_\mathrm{PL} = \begin{cases} \frac{N_\mathrm{PL}\alpha}{D_2^\alpha - D_1^\alpha} D_\mathrm{p}^\alpha, & D_1 \le D_\mathrm{p} \le D_2, \alpha \neq 0 \\ \frac{N_\mathrm{PL}}{\ln(D_2/D_1)}, & D_1 \le D_\mathrm{p} \le D_2, \alpha = 0\,, \\ 0, & \text{otherwise} \end{cases} \tag{3}$$

where N_PL is the total particle number concentration, α is the slope parameter, D_1 is the smallest diameter, and D_2 is the largest diameter of the PL distribution. In this form, the PL distribution has four parameters, which leads to numerical challenges for the reconstruction of the distribution parameters from four moments. Nevertheless, by fixing one parameter, only three moments are required to be modelled and the reconstruction will simplify. Here, the value of D_1 is fixed to the diameter of a newly formed particle, which is also physically sensible because that value is not expected to vary significantly; in atmospheric particle formation, the value is about $1.5 \pm 0.3\,\mathrm{nm}$ (Kulmala et al., 2013).

Three moments required in the modelling of the PL distribution with parameters N_PL, α, and D_2 are, in this article, number, N_PL, surface area, S_PL, and mass, M_PL, concentrations,

$$N_\mathrm{PL} = N_\mathrm{PL} \tag{4}$$

$$\begin{aligned} S_\mathrm{PL} &= \int_{-\infty}^{\infty} s_\mathrm{p} \left.\frac{\mathrm{d}N}{\mathrm{d}\ln D_\mathrm{p}}\right|_\mathrm{PL} \mathrm{d}\ln D_\mathrm{p} \\ &= s_1 N_\mathrm{PL} \frac{\alpha}{\alpha+2} \frac{\left(\frac{D_2}{D_1}\right)^{\alpha+2} - 1}{\left(\frac{D_2}{D_1}\right)^{\alpha} - 1} \end{aligned} \tag{5}$$

$$\begin{aligned} M_\mathrm{PL} &= \int_{-\infty}^{\infty} m_\mathrm{p} \left.\frac{\mathrm{d}N}{\mathrm{d}\ln D_\mathrm{p}}\right|_\mathrm{PL} \mathrm{d}\ln D_\mathrm{p} \\ &= m_1 N_\mathrm{PL} \frac{\alpha}{\alpha+3} \frac{\left(\frac{D_2}{D_1}\right)^{\alpha+3} - 1}{\left(\frac{D_2}{D_1}\right)^{\alpha} - 1}, \end{aligned} \tag{6}$$

where s_p and m_p are the surface area and the mass of a particle, respectively, and s_1 and m_1 are the surface area and the mass of a newly formed particle, respectively. All particles are assumed to be spherical. Equations (5) and (6) have singularities at α values of -3, -2, and 0. In those cases, the equations have different formulations, and from now on, the singularity equations are not shown here due to the fact that α will never equal a singularity value precisely in a simulation. To model the composition of particles can be done by separating the mass concentration to different components using the assumption that the particles are internally mixed, i.e., the composition does not vary with particle diameter. Modelling of the particle composition is, however, outside of the scope of this article.

The reconstruction of the distribution parameters from the moments N_{PL}, S_{PL}, and M_{PL} is performed as follows. The zeroth moment N_{PL} is already one of the distribution parameters, but S_{PL} and M_{PL} are not. The latter are converted to the system of equations of two unknown variables α and $d = D_2/D_1$

$$\begin{cases} \frac{M_{\mathrm{PL}}}{N_{\mathrm{PL}}} \frac{1}{m_1} & = \left(\frac{\alpha}{\alpha+3}\right)\left(\frac{d^{\alpha+3}-1}{d^{\alpha}-1}\right) \\ \frac{M_{\mathrm{PL}}}{S_{\mathrm{PL}}} \frac{s_1}{m_1} & = \left(\frac{\alpha+2}{\alpha+3}\right)\left(\frac{d^{\alpha+3}-1}{d^{\alpha+2}-1}\right) \end{cases}. \tag{7}$$

However, there is no analytical solution for this system of equations, but solving two variables numerically is sufficiently fast for this purpose. A pre-calculated interpolation table is used in the numerical solution, with which a more rapid calculation is obtained. The interpolation table increases the memory cost of the model, but as the table is unique (independent on temporal or spatial coordinate) it needs to be stored in one memory location only.

2.1.2 Log-normal distribution

The LN distribution is expressed by the equation

$$\left.\frac{\mathrm{d}N}{\mathrm{d}\ln D_{\mathrm{p}}}\right|_{\mathrm{LN}} = \frac{N_{\mathrm{LN}}}{\sqrt{2\pi}\ln\sigma} \exp\left[-\frac{\ln^2(D_{\mathrm{p}}/D_{\mathrm{g}})}{2\ln^2\sigma}\right], \tag{8}$$

where N_{LN} is the total particle number concentration, σ the geometric standard deviation, and D_{g} the geometric mean diameter of the LN distribution. The LN distribution is also modelled as three moments, N_{LN}, S_{LN}, and M_{LN}. Following the method of Whitby and McMurry (1997), the reconstruction of the distribution parameters from the moments can be performed using the equations

$$N_{\mathrm{LN}} = N_{\mathrm{LN}} \tag{9}$$

$$D_{\mathrm{g}} = 6^{-2/3}\pi^{-5/6}\rho^{2/3} N_{\mathrm{LN}}^{-5/6} S_{\mathrm{LN}}^{3/2} M_{\mathrm{LN}}^{-2/3} \tag{10}$$

$$\ln^2\sigma = \ln\left(6^{2/3}\pi^{1/3}\rho^{-2/3} N_{\mathrm{LN}}^{1/3} S_{\mathrm{LN}}^{-1} M_{\mathrm{LN}}^{2/3}\right), \tag{11}$$

where ρ is the particle density.

2.1.3 Connection between the distributions

The combined particle distribution is modelled as the superposition of the PL and the LN distributions

$$\left.\frac{\mathrm{d}N}{\mathrm{d}\ln D_{\mathrm{p}}}\right|_{\mathrm{PL+LN}} = \left.\frac{\mathrm{d}N}{\mathrm{d}\ln D_{\mathrm{p}}}\right|_{\mathrm{PL}} + \left.\frac{\mathrm{d}N}{\mathrm{d}\ln D_{\mathrm{p}}}\right|_{\mathrm{LN}}. \tag{12}$$

Figure 1 presents examples of the PL+LN distribution. PL distributions with different values of α are shown in the left pane; $N = 10^6\,\mathrm{cm}^{-3}$, $D_1 = 1.5\,\mathrm{nm}$, and $D_2 = 5\,\mathrm{nm}$ are equal in all four distributions. The right pane shows the PL distribution with values $N = 10^6\,\mathrm{cm}^{-3}$, $\alpha = 1$, $D_1 = 1.5\,\mathrm{nm}$, and $D_2 = 3\,\mathrm{nm}$, the LN distribution with values $N = 5\times10^5\,\mathrm{cm}^{-3}$, $D_{\mathrm{g}} = 4\,\mathrm{nm}$, and $\sigma = 1.1$, and the combination of them.

A schematic presentation of the connections between the distributions is shown in Fig. 2. Particles in the PL distribution, formed by new particle formation and grown by condensation and coagulation (Fig. 3), are transferred to the LN distribution through three intermodal processes: coagulational transfer, intermodal coagulation, and condensational transfer. The coagulational transfer is accounted by intramodal coagulation, i.e., self-coagulation, which is basically an intramodal process, but in this model it is used to initiate the LN distribution by transferring the coalesced resultant particles larger than D_2 to the LN distribution. The coagulational transfer is described in more detail in Sec. 2.2.5. After the LN distribution is initiated, particles of the both distributions begin to collide intermodally (the intermodal coagulation). In that case, the resultant particles are always assigned to the LN distribution, which is thought to consist of larger particles than the PL distribution.

The coagulational transfer remains the only process initiating the formation of the LN distribution if the condensational transfer is neglected. Therefore, in the case of low particle number concentration, i.e., low intramodal coagulation rate, the formation rate of the LN distribution is slow; thus, the combined distribution would be mainly in a power law form. However, in realistic particle formation events, log-normal features in the size distribution are widely observed (Hinds, 1999). This is due to the facts that the aerosol processes have normally time- and size-dependent rates and that the particles can be multicomponent, and due to the intramodal coagulation that eventually results in self-preserving log-normal distribution (Friedlander, 2000). The model described here connects the formation of the LN distribution with the intramodal coagulation only. Therefore, log-normal features can be generated artificially to the PL+LN distribution by transferring some of the particles from the PL distribution to the LN distribution. This transfer is calculated through condensation (the condensational transfer). Particles that are to be grown beyond the diameter D_2 are transferred to the LN distribution by the condensational transfer instead of keeping them in the PL distribution and increasing the value of D_2. The condensational transfer is described in more detail in Sec. 2.2.5.

2.2 Aerosol processes

The general dynamic equation for a particular moment X ($= N_{\mathrm{PL}}$, S_{PL}, M_{PL}, N_{LN}, S_{LN}, or M_{LN}) in a one-dimensional (temporal coordinate only) simulation is

$$\frac{\mathrm{d}X}{\mathrm{d}t} = \mathrm{npf}_X + \mathrm{cond}_X + \mathrm{coag}_X + \mathrm{loss}_X^{\mathrm{coag}} + \mathrm{loss}_X^{\mathrm{dep}} + \mathrm{transfer}_X^{\mathrm{coag}} + \mathrm{transfer}_X^{\mathrm{cond}}, \tag{13}$$

where terms on the right hand side denote new particle formation, condensation, coagulation, coagulational losses, depositional losses, coagulational transfer, and condensational transfer, respectively. The formulation of the terms is described next.

2.2.1 New particle formation

New particle formation is modelled by a term

$$\mathrm{npf}_X = \begin{cases} J(t), & X = N_{\mathrm{PL}} \\ J(t)\, s_1, & X = S_{\mathrm{PL}} \\ J(t)\, m_1, & X = M_{\mathrm{PL}} \\ 0, & X = N_{\mathrm{LN}},\ S_{\mathrm{LN}},\ \text{or}\ M_{\mathrm{LN}} \end{cases}, \tag{14}$$

where $J(t)$ can be calculated, e.g., through any nucleation theory, in which $J(t)$ depend also on vapor concentrations and temperature, for example. However, finding the correct formulation for $J(t)$ is outside of the scope of this article; thus, we decided to use formation rate as an input parameter that can be either a constant, J, or a time-dependent function, $J(t)$. Additionally, inverse modelling is done to obtain $J(t)$ from measured particle number concentrations.

The sizes of a newly formed particle (D_1, s_1, and m_1) can be obtained from nucleation theories, but they are assumed to be constants here. In the case where $J(t)$ suddenly drops to zero but condensation still continues, concentration of particles with diameters around D_1 would subsequently decrease down to zero due to the growth of newly formed particles to larger diameters. Therefore, D_1, as a parameter of the PL distribution, should be a variable to model the distribution accurately. However, this would change the distribution back to a more complex four-parameter distribution that is outside of the scope of this article. In that case or with smoothly decreasing $J(t)$, α has a tendency to increase.

2.2.2 Condensation

Condensation rate [$\mathrm{kg\,m^{-3}s}$] of vapor v on a particle distribution, PL or LN (denoted with i), can be modelled as (Olin et al., 2015)

$$\mathrm{cond}_{M_i} = \int_{-\infty}^{\infty} \frac{\mathrm{d}m_{\mathrm{p},v}}{\mathrm{d}t} \left.\frac{\mathrm{d}N}{\mathrm{d}\ln D_\mathrm{p}}\right|_i \mathrm{d}\ln D_\mathrm{p}, \tag{15}$$

where $\frac{\mathrm{d}m_{\mathrm{p},v}}{\mathrm{d}t}$ is the mass growth rate of a particle [$\mathrm{kg\,s^{-1}}$] due to vapor v (Lehtinen and Kulmala, 2003),

$$\frac{\mathrm{d}m_{\mathrm{p},v}}{\mathrm{d}t} = 2\pi(D_\mathrm{p}+D_v)(\mathcal{D}_\mathrm{p}+\mathcal{D}_v)(C_{v,\infty}-C_{v,\mathrm{p}})\frac{\mathrm{Kn}+1}{0.377\mathrm{Kn}+1+\frac{4}{3\phi}(\mathrm{Kn}^2+\mathrm{Kn})}, \tag{16}$$

where D_v is the diameter of a vapor molecule. $\mathcal{D}_\mathrm{p}$ and $\mathcal{D}_v$ are the diffusion coefficients of a particle and of a vapor molecule, respectively. $C_{v,\infty}$ and $C_{v,\mathrm{p}}$ are the mass concentration of the vapor in the far-field and over the particle surface, respectively. Kn and ϕ are the Knudsen number and the mass accommodation coefficient, respectively. The concentration $C_{v,\mathrm{p}}$ is

$$C_{v,\mathrm{p}} = \Gamma_v\, C_{v,\mathrm{sat}} \exp\left(\frac{4\mathcal{S}m_v}{k_\mathrm{B}T\rho D_\mathrm{p}}\right), \tag{17}$$

where Γ_v, $C_{v,\mathrm{sat}}$, and m_v are activity, the saturation concentration, and the molecule mass of the vapor, respectively, $\mathcal{S}$ is surface tension, k_B is the Boltzmann constant, and T is temperature.

In one-dimensional simulation, the mass growth rate can be considered a function of time and the particle diameter only, not of the spatial location, if the other parameters in Eq. (16) are considered also. Here, the mass growth rate (single-component case) is expressed using condensational growth rate $g(t, D_\mathrm{p})$

$$\frac{\mathrm{d}m_\mathrm{p}}{\mathrm{d}t}(t, D_\mathrm{p}) = \frac{\mathrm{d}m_\mathrm{p}}{\mathrm{d}D_\mathrm{p}} \cdot \frac{\mathrm{d}D_\mathrm{p}}{\mathrm{d}t}(t, D_\mathrm{p}) = \frac{\pi}{2}\rho D_\mathrm{p}^2\, g(t, D_\mathrm{p}). \tag{18}$$

Hence, the condensation rate for a particle distribution becomes

$$\mathrm{cond}_{M_i} = \frac{\pi}{2}\rho \int_{-\infty}^{\infty} D_\mathrm{p}^2\, g(t, D_\mathrm{p}) \left.\frac{\mathrm{d}N}{\mathrm{d}\ln D_\mathrm{p}}\right|_i \mathrm{d}\ln D_\mathrm{p}, \tag{19}$$

which has an analytical solution for the both distributions, PL and LN, when $g(t, D_\mathrm{p})$ can be expressed with a polynomial of D_p. The mass growth rate is proportional to D_p^2 if the following conditions are met: 1) the particle size is in free-molecular regime, 2) $D_p \gg D_v$, 3) $C_{v,\infty} \gg C_{v,\mathrm{p}}$. The last one applies when the particle size is large or when the vapor has low saturation vapor pressure. Since particle sizes near the molecular size are modelled in this article, only the first condition applies satisfactorily. Nevertheless, this article concentrates mainly in cases where the mass growth rate is assumed to be proportional to D_p^2. Additionally, a single test case, where the mass growth rate is calculated using Eqs. (16) – (17), is presented. The main point in this article is not to provide the correct formulation for $g(t, D_\mathrm{p})$, but to compare different models, and additionally to perform inverse modelling to obtain $g(t)$ from the time evolution of measured aerosol size distributions. Due to the assumption of the proportionality of the mass growth rate, the condensational growth rate becomes size-independent, and finally, the condensation terms used in Eq. (13) become

$$\mathrm{cond}_X = \begin{cases} 0, & X = N_i \\ 2\pi\, g(t) \int_{-\infty}^{\infty} D_\mathrm{p}\, \mathrm{d}N_i, & X = S_i \\ \frac{\pi}{2} \rho\, g(t) \int_{-\infty}^{\infty} D_\mathrm{p}^2\, \mathrm{d}N_i, & X = M_i \end{cases} \tag{20}$$

where $\mathrm{d}N_i$ is an abbreviation of

$$\left.\frac{\mathrm{d}N}{\mathrm{d}\ln D_\mathrm{p}}\right|_i \mathrm{d}\ln D_\mathrm{p}. \tag{21}$$

The analytical solution for Eq. (20) is

$$\mathrm{cond}_X = X\, g(t) \cdot \begin{cases} 0, & X = N_\mathrm{PL} \\ \frac{2}{D_1}\left(\frac{\alpha+2}{\alpha+1}\right)\left(\frac{d^{\alpha+1}-1}{d^{\alpha+2}-1}\right), & X = S_\mathrm{PL} \\ \frac{3}{D_1}\left(\frac{\alpha+3}{\alpha+2}\right)\left(\frac{d^{\alpha+2}-1}{d^{\alpha+3}-1}\right), & X = M_\mathrm{PL} \\ 0, & X = N_\mathrm{LN} \\ \frac{2}{D_\mathrm{g}} \exp\left(-\frac{3}{2}\ln^2\sigma\right), & X = S_\mathrm{LN} \\ \frac{3}{D_\mathrm{g}} \exp\left(-\frac{5}{2}\ln^2\sigma\right), & X = M_\mathrm{LN} \end{cases} \tag{22}$$

when α is not -3, -2, or -1.

When the mass growth rate is calculated from the vapor concentrations and the properties of the vapor and the particles using Eqs. (16) – (17), it rarely can be expressed with a polynomial of D_p, unless polynomial fits are done for the function. However, if the vapor concentrations or the other properties are allowed to vary during the simulation, fits for the mass growth rate function may become inconvenient. In that case, the integral in Eq. (19) cannot be solved analytically. Therefore, numerical integration is required, in which Eq. (19) is calculated in a form of

$$\mathrm{cond}_{M_i} = \frac{\pi}{2}\rho \sum_{j=1}^{n} D_j^2\, g(t, D_j)\ \left.\frac{\mathrm{d}N}{\mathrm{d}\ln D_\mathrm{p}}\right|_i \ln\frac{D_{j+1}}{D_j}, \tag{23}$$

where D_j is the particle diameter of the size section j used in numerical integration when the particle diameter range is split into n sections. Computational cost of numerical integration is, however, higher compared to analytical solution of the integrals. Therefore, Gaussian quadratures are used here to reduce the associated computing time; they provide the optimal particle diameters and their weights for efficient evaluation of the integrals. The details of the Gaussian quadratures are described in Appendix A.

2.2.3 Coagulation

Coagulation is modelled as intramodal coagulation within the PL distribution and within the LN distribution, and as intermodal coagulation from the PL distribution to the LN distribution. The coagulation terms derived from the equations of Whitby and McMurry (1997) are

$$\begin{aligned}\mathrm{coag}_{N_{\mathrm{PL}}} = &-\frac{1}{2}\int_{-\infty}^{\infty}\int_{-\infty}^{\infty}\beta(D_\mathrm{p},D'_\mathrm{p})\,\mathrm{d}N_{\mathrm{PL}}\,\mathrm{d}N'_{\mathrm{PL}}\\ &-\int_{-\infty}^{\infty}\int_{-\infty}^{\infty}\beta(D_\mathrm{p},D'_\mathrm{p})\,\mathrm{d}N_{\mathrm{PL}}\,\mathrm{d}N'_{\mathrm{LN}} \qquad (24)\\ \mathrm{coag}_{S_{\mathrm{PL}}} = &-\frac{1}{2}\int_{-\infty}^{\infty}\int_{-\infty}^{\infty}\left[2s_\mathrm{p}-\left(s_\mathrm{p}^{\frac{3}{2}}+s_\mathrm{p}'^{\frac{3}{2}}\right)^{\frac{2}{3}}\right]\beta(D_\mathrm{p},D'_\mathrm{p})\,\mathrm{d}N_{\mathrm{PL}}\,\mathrm{d}N'_{\mathrm{PL}}\\ &-\int_{-\infty}^{\infty}\int_{-\infty}^{\infty}s_\mathrm{p}\,\beta(D_\mathrm{p},D'_\mathrm{p})\,\mathrm{d}N_{\mathrm{PL}}\,\mathrm{d}N'_{\mathrm{LN}} \qquad (25)\\ \mathrm{coag}_{M_{\mathrm{PL}}} = &-\int_{-\infty}^{\infty}\int_{-\infty}^{\infty}m_\mathrm{p}\,\beta(D_\mathrm{p},D'_\mathrm{p})\,\mathrm{d}N_{\mathrm{PL}}\,\mathrm{d}N'_{\mathrm{LN}} \qquad (26)\\ \mathrm{coag}_{N_{\mathrm{LN}}} = &-\frac{1}{2}\int_{-\infty}^{\infty}\int_{-\infty}^{\infty}\beta(D_\mathrm{p},D'_\mathrm{p})\,\mathrm{d}N_{\mathrm{LN}}\,\mathrm{d}N'_{\mathrm{LN}} \qquad (27)\\ \mathrm{coag}_{S_{\mathrm{LN}}} = &-\frac{1}{2}\int_{-\infty}^{\infty}\int_{-\infty}^{\infty}\left[2s_\mathrm{p}-\left(s_\mathrm{p}^{\frac{3}{2}}+s_\mathrm{p}'^{\frac{3}{2}}\right)^{\frac{2}{3}}\right]\beta(D_\mathrm{p},D'_\mathrm{p})\,\mathrm{d}N_{\mathrm{LN}}\,\mathrm{d}N'_{\mathrm{LN}}\\ &+\int_{-\infty}^{\infty}\int_{-\infty}^{\infty}\left[\left(s_\mathrm{p}^{\frac{3}{2}}+s_\mathrm{p}'^{\frac{3}{2}}\right)^{\frac{2}{3}}-s'_\mathrm{p}\right]\beta(D_\mathrm{p},D'_\mathrm{p})\,\mathrm{d}N_{\mathrm{PL}}\,\mathrm{d}N'_{\mathrm{LN}} \qquad (28)\\ \mathrm{coag}_{M_{\mathrm{LN}}} = &\int_{-\infty}^{\infty}\int_{-\infty}^{\infty}m_\mathrm{p}\,\beta(D_\mathrm{p},D'_\mathrm{p})\,\mathrm{d}N_{\mathrm{PL}}\,\mathrm{d}N'_{\mathrm{LN}}, \qquad (29)\end{aligned}$$

where $\beta(D_\mathrm{p},D'_\mathrm{p})$ is the coagulation coefficient of particles with the diameters of D_p and D'_p calculated with the equation

$$\beta(D_\mathrm{p},D'_\mathrm{p}) = 2\pi(D_\mathrm{p}+D'_\mathrm{p})(\mathcal{D}_\mathrm{p}+\mathcal{D}'_\mathrm{p})f(\mathrm{Kn}_{\mathrm{coag}}), \qquad (30)$$

where $f(\mathrm{Kn_{coag}})$ is the transition regime function of Dahneke (1983)

$$f(\mathrm{Kn_{coag}}) = \frac{1 + \mathrm{Kn_{coag}}}{1 + 2\mathrm{Kn_{coag}} + 2\mathrm{Kn_{coag}^2}}, \tag{31}$$

where $\mathrm{Kn_{coag}}$ is the Knudsen number for coagulation

$$\mathrm{Kn_{coag}} = \frac{4(\mathcal{D}_\mathrm{p} + \mathcal{D}'_\mathrm{p})}{(D_\mathrm{p} + D'_\mathrm{p})\sqrt{\bar{c}^2 + \bar{c}'^2}}, \tag{32}$$

where $\bar{c}$ and $\bar{c}'$ are the mean thermal velocities of particles with the diameters of D_p and D'_p.

The integrals in Eqs. (24) – (29) cannot be solved analytically in the transition regime because Eq. (31) cannot be presented in a polynomial form. Therefore, the integrals are calculated numerically or by using quadratures in the same manner as with the condensation term described in Appendix A.

2.2.4 Particle losses

The losses due to coagulation of the particles in the PL+LN distribution to the background distribution excluded from the PL+LN distribution are considered the coagulational losses. Particles in the background distribution are assumed to be significantly larger than the particles in the PL+LN distribution. Therefore, the particle diameters of the background distribution can be approximated with a single diameter value, e.g., $\mathrm{CMD_{bg}}$ (count median diameter). According to Kerminen and Kulmala (2002), the coagulation coefficient will then become

$$\beta(D_\mathrm{p}, \mathrm{CMD_{bg}}) \approx \beta(D_1, \mathrm{CMD_{bg}}) \left(\frac{D_\mathrm{p}}{D_1}\right)^{l_\mathrm{bg}}, \tag{33}$$

where l_bg is the exponent depending on $\mathrm{CMD_{bg}}$. The value of l_bg ranges between -2 and -1 (Lehtinen et al., 2007). The coagulational loss term, e.g., for a number concentration is

$$\mathrm{loss}_{N_i}^\mathrm{coag} = N_\mathrm{bg} \int_{-\infty}^{\infty} \beta(D_\mathrm{p}, \mathrm{CMD_{bg}}) \mathrm{d}N_i \approx N_\mathrm{bg}\, \beta(D_1, \mathrm{CMD_{bg}}) D_1^{-l_\mathrm{bg}} \int_{-\infty}^{\infty} D_\mathrm{p}^{l_\mathrm{bg}}\, \mathrm{d}N_i, \tag{34}$$

in which the last integral can be solved analytically. The analytical solutions for the coagulational loss terms are

$$\mathrm{loss}_X^\mathrm{coag} = X N_\mathrm{bg} \cdot \begin{cases} \beta(D_1, \mathrm{CMD_{bg}}) \left(\frac{\alpha}{\alpha + l_\mathrm{bg}}\right) \left(\frac{d^{\alpha + l_\mathrm{bg}} - 1}{d^\alpha - 1}\right), & X = N_\mathrm{PL} \\ \beta(D_1, \mathrm{CMD_{bg}}) \left(\frac{\alpha+2}{\alpha+2+l_\mathrm{bg}}\right) \left(\frac{d^{\alpha+2+l_\mathrm{bg}} - 1}{d^{\alpha+2} - 1}\right), & X = S_\mathrm{PL} \\ \beta(D_1, \mathrm{CMD_{bg}}) \left(\frac{\alpha+3}{\alpha+3+l_\mathrm{bg}}\right) \left(\frac{d^{\alpha+3+l_\mathrm{bg}} - 1}{d^{\alpha+3} - 1}\right), & X = M_\mathrm{PL} \\ \beta(D_\mathrm{g}, \mathrm{CMD_{bg}}) \exp\left[\frac{1}{2} l_\mathrm{bg}^2 \ln^2 \sigma\right], & X = N_\mathrm{LN} \\ \beta(D_\mathrm{g}, \mathrm{CMD_{bg}}) \exp\left[\left(\frac{1}{2} l_\mathrm{bg}^2 + 2 l_\mathrm{bg}\right) \ln^2 \sigma\right], & X = S_\mathrm{LN} \\ \beta(D_\mathrm{g}, \mathrm{CMD_{bg}}) \exp\left[\left(\frac{1}{2} l_\mathrm{bg}^2 + 3 l_\mathrm{bg}\right) \ln^2 \sigma\right], & X = M_\mathrm{LN} \end{cases} \tag{35}$$

when α is not 0 or $-l_{\mathrm{bg}}$.

The losses to walls due to diffusion of particles are considered the depositional losses. They are modelled with the method of Hussein et al. (2009), in which the deposition rate of particles in a test chamber is

$$\lambda = \frac{1}{V}\sum_{w} A_w u \tag{36}$$

where V is the volume of the chamber, A_w is the surface area of the wall w, and u is the deposition velocity of particles. A simple approximation for the deposition velocity is used here

$$u \propto D_{\mathrm{p}}^{-1}, \tag{37}$$

which is valid for particles smaller than $100\,\mathrm{nm}$ according to Lai and Nazaroff (2000). The depositional loss term, e.g, for a number concentration now become

$$\mathrm{loss}_{N_i}^{\mathrm{dep}} = \int_{-\infty}^{\infty} \lambda \mathrm{d}N_i = k_{\mathrm{dep}} \int_{-\infty}^{\infty} D_{\mathrm{p}}^{-1} \mathrm{d}N_i \tag{38}$$

where all effects, except the effect of the diameter, are included in the deposition coefficient k_{dep}. The last integral can be solved analytically, from which the depositional loss terms become

$$\mathrm{loss}_{X}^{\mathrm{dep}} = X k_{\mathrm{dep}} \cdot \begin{cases} D_1^{-1}\left(\frac{\alpha}{\alpha-1}\right)\left(\frac{d^{\alpha-1}-1}{d^{\alpha}-1}\right), & X = N_{\mathrm{PL}} \\ D_1^{-1}\left(\frac{\alpha+2}{\alpha+1}\right)\left(\frac{d^{\alpha+1}-1}{d^{\alpha+2}-1}\right), & X = S_{\mathrm{PL}} \\ D_1^{-1}\left(\frac{\alpha+3}{\alpha+2}\right)\left(\frac{d^{\alpha+2}-1}{d^{\alpha+3}-1}\right), & X = M_{\mathrm{PL}} \\ D_{\mathrm{g}}^{-1}\exp\left(\frac{1}{2}\ln^2\sigma\right), & X = N_{\mathrm{LN}} \\ D_{\mathrm{g}}^{-1}\exp\left(-\frac{3}{2}\ln^2\sigma\right), & X = S_{\mathrm{LN}} \\ D_{\mathrm{g}}^{-1}\exp\left(-\frac{5}{2}\ln^2\sigma\right), & X = M_{\mathrm{LN}} \end{cases} \tag{39}$$

when α is not 0 or 1.

The effect of particle losses on the PL distribution is seen as decreased α. In the trivial case, as in Eq. (1), α becomes less than zero when $k_{\mathrm{dep}} > g$. This effect is due to increased losses with increasing particle diameters because larger particles have longer residence times from the moment since their formation. However, Eq. (37) counteracts in this effect by decreasing the deposition velocity with increasing particle size, but with small g, the effect of increased residence time dominates over the effect of decreased deposition velocity. Additionally, α is further decreased due to coagulational losses.

2.2.5 Intermodal particle transfer

The intermodal coagulation is included together with the intramodal coagulation in the coagulation terms (coag_X) seen in Eqs. (24) – (29). The coagulational ($\mathrm{transfer}_X^{\mathrm{coag}}$) and condensational ($\mathrm{transfer}_X^{\mathrm{cond}}$) transfer are modelled as follows.

Particles with the diameter higher than the cut diameter

$$D_{\text{coag}} = \left(D_2^3 - D_{\text{p}}'^3\right)^{1/3} \tag{40}$$

form particles with the diameter higher than D_2 after coagulating with a particle having a diameter of D_{p}', assuming full coalescence (Fig. 2). Those resultant particles are transferred from the PL distribution to the LN distribution, because their particle diameters will correspond with the form of a log-normal distribution rather than a power law distribution, which can be observed using a highly accurate sectional model. The coagulational transfer terms are negative for the PL distribution and positive for the LN distribution to conserve the moments, and they are expressed as

$$\text{transfer}_{N_{\text{PL}}} = -\,\text{transfer}_{N_{\text{LN}}} = -\frac{1}{2}\int_{-\infty}^{\infty}\int_{\ln D_{\text{coag}}}^{\infty} \beta(D_{\text{p}}, D_{\text{p}}')\,\mathrm{d}N_{\text{PL}}\,\mathrm{d}N_{\text{PL}}' \tag{41}$$

$$\text{transfer}_{S_{\text{PL}}} = -\,\text{transfer}_{S_{\text{LN}}} = -\frac{1}{2}\int_{-\infty}^{\infty}\int_{\ln D_{\text{coag}}}^{\infty} \left(s_{\text{p}}^{\frac{3}{2}} + s_{\text{p}}'^{\frac{3}{2}}\right)^{\frac{2}{3}} \beta(D_{\text{p}}, D_{\text{p}}')\,\mathrm{d}N_{\text{PL}}\,\mathrm{d}N_{\text{PL}}' \tag{42}$$

$$\text{transfer}_{M_{\text{PL}}} = -\,\text{transfer}_{M_{\text{LN}}} = -\frac{1}{2}\int_{-\infty}^{\infty}\int_{\ln D_{\text{coag}}}^{\infty} \left(m_{\text{p}} + m_{\text{p}}'\right)\beta(D_{\text{p}}, D_{\text{p}}')\,\mathrm{d}N_{\text{PL}}\,\mathrm{d}N_{\text{PL}}', \tag{43}$$

which are calculated using the quadrature or numerical integration as in the case of the coagulation terms.

Considering a time step of Δt in a Lagrangian simulation, particles with the diameters larger than $D_{\text{cond}} = D_2 - g\,\Delta t$ will grow due to condensation to have the diameters larger than D_2 (Fig. 2). Modelling condensation only, the value of D_2 at the next time step would increase to $D_2 + g\,\Delta t$. The condensational transfer is used to transfer the particles in the PL distribution with the diameters of $D_{\text{cond}} < D_{\text{p}} < D_2$ to the LN distribution. However, if the condensational transfer is modelled fully, D_2 would never increase and all condensation would affect the LN distribution only. In that case, the distributions would separate from each other. For this reason, the effect of condensational transfer is dampened using a factor γ as a multiplier in the condensational transfer equations. The factor can obtain values between zero and unity, and it describes how the particles will be distributed between the PL and the LN distributions. The value $\gamma = 0$ produces a distribution that will be mainly in a power law form; the value $\gamma = 1$ produces a log-normal distribution only. To choose a suitable value for γ for a simulation, the user should consider how well does the aerosol formation event follow the approximations of the theory described here. The value 0 is suitable only when the aerosol processes follow the theory exactly. To simulate a realistic particle formation event, the value has to be increased towards unity using the following guidelines. The more the following conditions are met, the higher γ should be used: (1) particle formation or growth are multicomponent processes, (2) the particle formation rate or the condensation growth rate vary significantly with time, (3) the condensational growth rate varies significantly with the particle size, (4) the background aerosol acting as a coagulation sink does not remain in a nearly constant state during the time domain of the simulation, (5) particle sizes in the background aerosol are not significantly higher than in the PL+LN distribution, (6) the depositional losses cannot be approximated with as simple form as described here, e.g., in the case of complex geometry or turbulent flow. In real atmospheric particle formation events, γ should rarely has the value of less than 0.5, which can also be

used as an initial guess if figuring the previous guidelines is problematic. If the shapes of the distributions to be modelled are initially known, the value of γ can be adjusted to obtain a proper model output, e.g., in the case of inverse modelling. The factor γ can also be considered a time-dependent function or a spatially varying variable, but here we concentrate only to constant values of γ because the theory behind the value of γ is currently unknown.

The number of particles in the PL distribution to be transferred to the LN distribution due to the condensational transfer in the time step of Δt is

$$N_{\mathrm{PL}\to\mathrm{LN}} = \gamma \int_{\ln D_{\mathrm{cond}}}^{\ln D_2} \left.\frac{\mathrm{d}N}{\mathrm{d}\ln D_\mathrm{p}}\right|_{\mathrm{PL}} \mathrm{d}\ln D_\mathrm{p}. \tag{44}$$

Considering infinitesimally small time step ($\Delta t \to 0$), D_{cond} approaches D_2 and $N_{\mathrm{PL}\to\mathrm{LN}}$ approaches

$$\gamma \frac{g\Delta t}{D_2} \left.\frac{\mathrm{d}N}{\mathrm{d}\ln D_\mathrm{p}}\right|_{\mathrm{PL},\, D_\mathrm{p}=D_2}. \tag{45}$$

The transferred amounts for S and M are obtained in the same approach as in Eq. (20), and they are negative for the PL distribution and positive for the LN distribution. Hence, the term for the condensational transfer becomes

$$\mathrm{transfer}_X^{\mathrm{cond}} = \gamma \frac{g(t)}{D_2} \left.\frac{\mathrm{d}N}{\mathrm{d}\ln D_\mathrm{p}}\right|_{\mathrm{PL},\, D_\mathrm{p}=D_2} \cdot \begin{cases} -1, & X = N_{\mathrm{PL}} \\ -s_2, & X = S_{\mathrm{PL}} \\ -m_2, & X = M_{\mathrm{PL}} \\ +1, & X = N_{\mathrm{LN}} \\ +s_2, & X = S_{\mathrm{LN}} \\ +m_2, & X = M_{\mathrm{LN}} \end{cases}, \tag{46}$$

where s_2 and m_2 are the surface area and the mass of the particle with the diameter of D_2. The condensational transfer does not alter the moments of the total distribution because particles are not altered in the transfer, it only transfers the particles between the distributions; therefore, the value of γ has a minor effect only on the moments, but a noticeable effect on the shape of the PL+LN distribution.

3 Simulation setup for the evaluation of the PL+LN model

The PL+LN model was evaluated with the simulations of theoretical test cases and a real particle formation case. The evaluation was done against sectional models that yield accurate results due to a high number of size sections. Two types of sectional models were used: fixed-sectional (FS) and moving-center fixed-sectional (MC) models. The models are further subdivided depending on the amount of size sections they use. FS models provide the best accuracy for the particle number concentration and MC models for the mass concentration, when a high number of size sections is modelled. The results from different models and from measurement data are examined by comparing the distributions, the moments (N, S, and M) and the variables, GMD

(geometric mean diameter) and GSD (geometric standard deviation). GMD and GSD can be calculated from a continuous or a discrete total distribution with the equations

$$\ln \mathrm{GMD} = \frac{1}{N} \int_{-\infty}^{\infty} \ln D_\mathrm{p} \, \mathrm{d}N = \frac{1}{N} \sum_j N_j \ln D_{\mathrm{p},j} \tag{47}$$

$$\ln^2 \mathrm{GSD} = \frac{1}{N} \int_{-\infty}^{\infty} \ln^2 \left(\frac{D_\mathrm{p}}{\mathrm{GMD}} \right) \mathrm{d}N = \frac{1}{N} \sum_j N_j \ln^2 \left(\frac{D_{\mathrm{p},j}}{\mathrm{GMD}} \right), \tag{48}$$

where $D_{\mathrm{p},j}$ is the geometric average particle diameter of the size section j. Relative errors of the moments and the variables compared to the reference models are calculated with

$$\delta_X = \frac{X - X_\mathrm{ref}}{X_\mathrm{ref}}, \tag{49}$$

where X and X_ref are the moment or the variable from the model in examination and from the reference model, respectively. FS models are considered the reference models, with the exception of the mass moment, M, in a real particle formation case, for which the reference model is an MC model, because it provides the best mass-conservation.

The capability of the PL+LN model in inverse modelling is also tested using the real measurement data from the particle formation event. The best estimates of the new particle formation rates, $J(t)$, and the condensational growth rates, $g(t)$, obtained from the different models, are compared with each other. These values for $J(t)$ and $g(t)$ are later used in the simulation that is used to examine the output accuracies and computational costs of different models.

The diameter of a newly formed particle was assumed to be a constant, $D_1 = 1.6\,\mathrm{nm}$, in all cases. The value was chosen because it is in the range of a relevant size of a particle from which atmospheric aerosol formation starts (Kulmala et al., 2007) and of a size of a smallest particle that can be detected with the Particle Size Magnifier (PSM) with the detection efficiency of nearly unity (Vanhanen et al., 2011). Single-component modelling was performed assuming a mixture with the particle bulk density of $\rho = 1.4\,\mathrm{g\,cm^{-3}}$ as the component. The value was chosen because it is a relevant density of small particles in the atmosphere (Kannosto et al., 2008).

3.1 Theoretical test cases

Theoretical test cases were used to compare the PL+LN model output with a highly accurate FS model. The FS model had 1000 size sections between 1.6 and 10 nm (FS1000) which is sufficiently dense to produce accurate results. Additionally, the PL+LN model was compared with the model having a log-normal distribution only (LN). All cases were simulated using constant and equal time steps to obtain a reliable comparison; the simulated time domains (t_max) were split into 3000 time steps.

The input parameters of the test cases are presented in Tab. 1. The Atm and Exh cases represent particle formation cases using input parameter values that reflect conditions typical to the atmosphere and to vehicle exhaust, respectively. Typical new particle formation rates in the atmosphere range from 0.01 to $10\,\mathrm{cm^{-3}\,s^{-1}}$ and condensational growth rates from 0.1 to $20\,\mathrm{nm\,h^{-1}}$ (Kulmala et al., 2004). In vehicle exhaust, new particle formation rates can reach up to $10^{10}\,\mathrm{cm^{-3}\,s^{-1}}$ and condensational growth rates up to $20\,\mathrm{nm\,s^{-1}}$ (Rönkkö et al., 2006; Uhrner et al., 2007; Olin et al., 2015). To test the PL+LN

model in a wide range of J and g, low values for Atm cases ($J = 0.1\,\mathrm{cm^{-3}\,s^{-1}}$, $g = 1\,\mathrm{nm\,h^{-1}}$) and high values for the Exh case ($J = 10^8\,\mathrm{cm^{-3}\,s^{-1}}$, $g = 5\,\mathrm{nm\,s^{-1}}$) were chosen. In addition to constant J and g values, a case having time-dependent $J(t)$ and a case having time-dependent $J(t)$ and size-dependent $g(D_\mathrm{p})$ were simulated.

The Atm1 case includes simultaneous new particle formation, condensation, intramodal-, and intermodal coagulation. For the Atm2 case, depositional losses were also added. The deposition coefficient $k_\mathrm{dep} = 1.8\,\mathrm{nm\,h^{-1}}$ was calculated by assuming that particle formation takes place in a test chamber with the dimensions of $3\,\mathrm{m} \times 2\,\mathrm{m} \times 2\,\mathrm{m}$ and with the deposition velocities of salt particles measured by Hussein et al. (2009). For the Atm3 case, a background distribution was added to act as the coagulation sink. The chosen values for the number concentration $N_\mathrm{bg} = 10^3\,\mathrm{cm^{-3}}$ and count median diameter $\mathrm{CMD_{bg}} = 100\,\mathrm{nm}$ of the background distribution have been observed, e.g., in a boreal forest area (Riipinen et al., 2007). The value for the coagulational loss exponent $l_\mathrm{bg} = -1.6$ was obtained from Lehtinen et al. (2007) using $\mathrm{CMD_{bg}} = 100\,\mathrm{nm}$. In the Atm4 case, a bell-shaped time-dependent function for the new particle formation rate (a bell-shaped form in the function of the number concentration between 3 and 6 nm is seen in studies of Sihto et al. (2006); Riipinen et al. (2007)) was modelled with

$$J(t) = J_0\, e^{-\left(\frac{t-t_0}{\tau_\mathrm{J}}\right)^2}, \tag{50}$$

where $t_0 = 1000\,\mathrm{s}$ is the time at which the highest new particle formation rate $J_0 = 0.1\,\mathrm{cm^{-3}\,s^{-1}}$ occurs and $\tau_\mathrm{J} = 5000\,\mathrm{s}$ represents the width of the bell-shaped curve.

The applicability of the PL+LN model using size-dependent condensational growth rates was evaluated with the Atm5 case, where $g(D_\mathrm{p})$ was modelled using Eqs. (16) – (18) and (23) – (A4). In this case, particles were assumed to consist of the mixture of sulfuric acid and water. The growth is modelled as the growth due to sulfuric acid, $\frac{\mathrm{d}m_{\mathrm{p,H_2SO_4}}}{\mathrm{d}t}$, calculated using the sulfuric acid vapor concentration $[\mathrm{H_2SO_4}] = 0.8 \times 10^7\,\mathrm{cm^{-3}}$, following the growth due to water vapor,

$$\frac{\mathrm{d}m_{\mathrm{p,H_2O}}}{\mathrm{d}t} = \left[\frac{1}{Y_{\mathrm{H_2SO_4}}(D_\mathrm{p})} - 1\right] \cdot \frac{\mathrm{d}m_{\mathrm{p,H_2SO_4}}}{\mathrm{d}t}, \tag{51}$$

where $Y_{\mathrm{H_2SO_4}}(D_\mathrm{p})$ is the mass fraction of sulfuric acid in a particle in water equilibrium, i.e., a particle having the composition with which no condensation or evaporation of water vapor occurs in temperature of 280 K and relative humidity of 60 % when the particle diameter is D_p. The approximation of water equilibrium is reasonable because, with these environmental values, $\sim 2 \times 10^{10}$ times more water molecules than sulfuric acid molecules exist and thus there are probably a sufficient amount of water molecules to condense on the particle to reach the equilibrium state before the next sulfuric acid molecule condenses on it. The properties of the vapors and the particles were calculated, using the equilibrium composition, as described in Olin et al. (2015). These environmental values were chosen because they are relevant values met in the atmosphere and they cause the condensational growth rate function that is far beyond a constant value in the particle diameter range of this case (from 1.6 nm to 8 nm), as seen in Fig. 4, which provides a beneficial test to examine how the model behaves with size-dependent g.

The Exh case represents simultaneous new particle formation, condensation, intramodal- and intermodal coagulation, coagulational losses, and depositional losses occurring in diesel vehicle exhaust inside the ageing chamber of a laboratory sampling system. The values $N_\mathrm{bg} = 10^6\,\mathrm{cm^{-3}}$ and $\mathrm{CMD_{bg}} = 60\,\mathrm{nm}$ were obtained from the measurements of Rönkkö et al. (2013) and the corresponding $l_\mathrm{bg} = -1.5$ from Lehtinen et al. (2007) using $\mathrm{CMD_{bg}} = 60\,\mathrm{nm}$. The deposition coefficient

$k_{\mathrm{dep}} = 0.07\,\mathrm{nm\,s^{-1}}$ was calculated using the ageing chamber dimensions of $5\,\mathrm{cm}$ (diameter) $\times$ $100\,\mathrm{cm}$ (length) and the deposition velocities of salt particles measured by Hussein et al. (2009).

Because the test cases are purely theoretical, the need of constructing log-normal features to the distributions through the condensational transfer artificially is minimal. In the Atm4 case, a time-dependent new particle formation rate suggests using the condensational transfer, but, according to the analysis of the shapes and the moments of the distributions, the output is not very sensitive to the value of γ, which is probably due to the bell-shaped function for the new particle formation rate that produces distributions containing both power law and log-normal features. In the Atm5 case, a size-dependent condensational growth rate outputs size distributions having features of a different kind, and thus the PL+LN distribution does not fit very satisfactorily in this case. According to the analysis of the shapes and the moments of the distributions in the Atm5 case, the best estimate for γ is 0.25, which was used in the Atm5 case; $\gamma = 0$ was used in all the other cases.

3.2 Mobile aerosol chamber particle formation event

The mobile aerosol chamber is a Teflon bag with the dimensions of $3\,\mathrm{m} \times 2\,\mathrm{m} \times 2\,\mathrm{m}$. The chamber is operated in a batch process, i.e., firstly, the chamber is filled with the air sample, and secondly, the sample is measured from the chamber. UV lights with the wavelength of $254\,\mathrm{nm}$ (UVC) are used in the chamber to initiate new particle formation and to boost the aging of the aerosol through photochemical processes. The chamber simulates a particle formation event occurring in the atmosphere, but with shorter time scale due to the UV lights. The chamber is designed to be mobile; therefore, it is fit to a car trailer.

The particle formation event measurement was performed at a street canyon measurement site of Helsinki Region Environmental Services Authority (HSY) located in Mäkelänkatu, Helsinki, Finland. The street had dense traffic during the measurement in 22 April 2015. The chamber was firstly filled with urban air and, once filled, the air sample was sucked with the measurement devices located in the mobile laboratory vehicle.

3.2.1 Processing the experimental data

The aerosol sample was measured using Airmodus Particle Size Magnifier (PSM), TSI Ultrafine Condensation Particle Counter (CPC), TSI Nano Scanning Mobility Particle Sizer (Nano-SMPS), TSI Engine Exhaust Particle Sizer (EEPS), and Dekati Electrical Low-Pressure Impactor (ELPI+). PSM in fixed saturator flow setting detects particles with the diameters of higher than about $1.6\,\mathrm{nm}$ (Vanhanen et al., 2011), CPC higher than about $3.6\,\mathrm{nm}$ (Mordas et al., 2008), and Nano-SMPS from about 7 to $64\,\mathrm{nm}$, with the detection efficiency of $50\,\%$ or higher. These cut diameters, $D_{\mathrm{PSM}} = 1.6\,\mathrm{nm}$, $D_{\mathrm{CPC}} = 3.6\,\mathrm{nm}$, and $D_{\text{Nano-SMPS}} = 7\,\mathrm{nm}$, are used to combine the data of PSM, CPC, and Nano-SMPS to obtain total aerosol size distributions for the diameter range of 1.6 – $64\,\mathrm{nm}$ with

$$\left.\frac{\mathrm{d}N}{\mathrm{d}\ln D_{\mathrm{p}}}\right|_{\text{measured}} = \begin{cases} \frac{\max\{N_{\mathrm{PSM}} - N_{\mathrm{CPC}}, 0\}}{\ln(D_{\mathrm{CPC}}/D_{\mathrm{PSM}})}, & D_{\mathrm{PSM}} \le D_{\mathrm{p}} < D_{\mathrm{CPC}} \\ \frac{\max\{N_{\mathrm{CPC}} - N_{\text{Nano-SMPS}}, 0\}}{\ln(D_{\text{Nano-SMPS}}/D_{\mathrm{CPC}})}, & D_{\mathrm{CPC}} \le D_{\mathrm{p}} < D_{\text{Nano-SMPS}} \\ \left.\frac{\mathrm{d}N}{\mathrm{d}\ln D_{\mathrm{p}}}\right|_{\text{Nano-SMPS}}, & D_{\mathrm{p}} \ge D_{\text{Nano-SMPS}} \end{cases}, \tag{52}$$

where N_{PSM}, N_{CPC}, and $N_{\mathrm{Nano\text{-}SMPS}}$ are the total number concentrations measured by the devices, and $\left.\frac{\mathrm{d}N}{\mathrm{d}\ln D_{\mathrm{p}}}\right|_{\mathrm{Nano\text{-}SMPS}}$ is the particle size distribution measured by Nano-SMPS. The maximum functions prevent the size distribution to become negative. Before the concentrations were input into Eq. (52), the concentrations output by the devices were synced. The data measured after the event were used in the synchronization, using the assumption that the device outputs are equal in that moment, because particle sizes are well within the range of high detection efficiency of all three devices. Nano-SMPS measures diameters down to $2\,\mathrm{nm}$, but due to its low accuracy for those diameters, all Nano-SMPS data below $7\,\mathrm{nm}$ was neglected. EEPS and ELPI+ having time resolutions of only $1\,\mathrm{s}$ were used to ensure the stability of the aerosol distribution during a Nano-SMPS scan lasting $150\,\mathrm{s}$: no rapid changes in the aerosol distribution were observed in the time scales shorter than $150\,\mathrm{s}$.

Initially, the aerosol in the chamber consisted of a background aerosol mode with CMD of $15\,\mathrm{nm}$ and the concentration of about $4000\,\mathrm{cm}^{-3}$, according to the Nano-SMPS data shown in Fig. 5. No major changes in the distribution were observed until the UV lights were switched on ($t = 0\,\mathrm{s}$). After switching the UV lights on, a nucleation mode begins to from, which is seen as the appearance of new particles at small particle diameters. It can be also seen that small particles exist though the growth process proceeds, which implies continuing new particle formation. The total distributions were altered from a power law-shape towards a log-normal-shape. After about $500\,\mathrm{s}$, particle concentration finished increasing (Fig. 6), which occurs because the gaseous precursors initiating new particle formation began to expire. The decreasing trend of particle number concentration after $500\,\mathrm{s}$ was accounted by coagulation and deposition. The particles of the nucleation mode and of the background mode grew to about $25\,\mathrm{nm}$ and to about $60\,\mathrm{nm}$ during the event, respectively. The total number, surface area, and mass concentrations of the measured nucleation mode were calculated from the total measured size distributions, Eq. (52), subtracted by log-normal distributions fitted to the background aerosol, assuming spherical particles with the density of $1.4\,\mathrm{g\,cm}^{-3}$. GMD and GSD of the measurement data were calculated also from the nucleation mode size distribution, using Eqs. (47) and (48), although the accuracy of the measured distribution for the diameters below the Nano-SMPS measurement range is poor.

3.2.2 Obtaining $J(t)$ and $g(t)$ through inverse modelling

Obtaining the values for the new particle formation rate, $J(t)$, and for the condensational growth rate, $g(t)$, for the particle formation event, occurred in a mobile aerosol chamber, was performed through inverse modelling. A time domain, starting from $152\,\mathrm{s}$ before switching the UV lights on and ending to $1663\,\mathrm{s}$ after switching the UV lights on, including 13 Nano-SMPS measurement scans, was simulated using different values for $J(t)$ and $g(t)$. Following the approach of Verheggen and Mozurkewich (2006), the least squares method was used to minimize the errors of the concentrations N, S, and M at 13 time moments which represent the middles of the Nano-SMPS scans. The values for $J(t)$ and $g(t)$ were assumed constants within a time step of a Nano-SMPS scan, $150\,\mathrm{s}$. The condensational growth rate was assumed also size-independent due to the lack of knowledge of the vapors participating in the condensation process. ODE45 solver was used in the simulations, and it provides the time steps that are sufficiently short to keep the result from altering more than $1\,\%$ compared to a previous time step but sufficiently long to keep the total computing time convenient.

Coagulation within the nucleation mode was included in the simulations, but the coagulational losses to the background mode was neglected because its low number concentration would had a minor effect only on the nucleation mode. The particles

formed in this case are possibly multicomponent due to the origin of the vapors, the new particle formation rate seems to vary significantly with time, and the measured distributions are wide, GSD values were up to 2. Therefore, a high value for the condensational transfer factor γ is expected to produce the best results using the PL+LN model. A constant value $\gamma = 0.8$ was used in the simulations because it produces the results that are the closest to the results of highly accurate sectional models, in this case. Due to a high value of γ, the coagulational transfer would had a minor effect only, and therefore it was neglected in the simulations. The depositional losses were modelled using the deposition coefficient $k_{\text{dep}} = 3780\,\text{nm}\,\text{h}^{-1}$ which is obtained by fitting the simulated number concentrations with the measured ones after particle formation and growth were quenched ($t > 1500\,\text{s}$).

Firstly, inverse modelling was performed using the PL+LN model. The time series of $J(t)$ and $g(t)$, that produced the most corresponding concentrations compared to the measured ones (Fig. 6), are presented in Figs. 7 and 8. Secondly, inverse modelling was performed using both an FS model having 400 size sections between 1.6 and 100 nm (FS400) and an MC model having 100 size sections between 1.6 and 100 nm (MC100), separately. The computing times of the FS400 and the MC100 models are significantly longer than of the PL+LN model; therefore, the time series of $J(t)$ and $g(t)$, obtained using the PL+LN model, were used as initial guesses when inverse modelling was performed using the FS400 or the MC100 model, to reduce the computing times. The associated computing time of the automatic inverse modelling procedure using the PL+LN model was approximately 2 orders of magnitude shorter than by using the FS400 or the MC100 model, which implies that a significant improvement in the computing time can be obtained using the PL+LN model in the case of inverse modelling. Inverse modelling was also performed using computationally more efficient LN model.

It can be seen from Fig. 7 that there are only minor differences in the values of $J(t)$ between the different models used in inverse modelling. The PL+LN model seems to need higher new particle formation rates compared to the accurate models, the FS400 and the MC100 models. Conversely, the LN model seems to need lower new particle formation rates. These denote that the PL+LN model has a tendency to underestimate the number concentrations, and that the LN model has a tendency to overestimate the number concentrations, because the output number concentrations of the models are nearly equal (Fig. 6). The values of $g(t)$, seen in Fig. 8, have also only minor differences between the different models. The values of $J(t)$ and $g(t)$ before the UV lights ($t < 0\,\text{s}$) seem unphysically high. That is caused because the simulation begins with no particles at $t = -252\,\text{s}$ but the measurement data include some nucleation mode particles at that time, even though the background aerosol distribution was subtracted from the measured distribution. All the particles are not subtracted because the subtraction was done with a purely log-normal distribution, which is exactly not the case of a measured data. Therefore, the simulation time range $-252\,\text{s} < t < -152\,\text{s}$ was used to produce the measured nucleation mode at the time of the first Nano-SMPS scan, $t = -152\,\text{s}$.

The effect of the choice for the lowest particle diameter, D_1, for the PL+LN model was also examined by performing inverse modelling with $D_1 = 1\,\text{nm}$ and $D_1 = 3\,\text{nm}$, in addition to $D_1 = 1.6\,\text{nm}$. Approximately 40 % higher values for $J(t)$ were needed to produce the measured concentrations when $D_1 = 1\,\text{nm}$ was used compared to $D_1 = 3\,\text{nm}$. This deviation occurs because smaller particles have higher losses, and with higher value for D_1, the smallest particles do not exist. The situation is the same for sectional models, because the smallest particle size needs to be chosen for them too. The choice for D_1 does not have significant effect on the condensational growth rate, in this case, due to size-independent $g(t)$.

The effect of the choice for the value of the condensational transfer factor, γ, for the PL+LN model was also examined by performing inverse modelling with the values between 0 and 1, in addition to $\gamma = 0.8$. With the values between 0.4 and 0.9, the times series of $J(t)$ obtained from inverse modelling deviate within 3 %, in average. However, with the values outside of that range, the deviation increased up to 36 %. The highest new particle formation rates are needed when the value of γ is low because the PL distribution dominates the number of particles, which leads to more small particles, which have high losses. Only minor effect (the deviations within 4 %) was seen on the time series of the condensational growth rate when the value of γ was altered between 0 and 1. In conclusion, choosing the value of 0.5 for γ if better guess for its value is lacking, as mentioned earlier, would produce reasonable results.

Figure 9 presents the time series of GMD and GSD of the nucleation mode, obtained from the different models used in inverse modelling and from the measured data. It can be observed that the models output these variables relatively well compared to the measured data, although they were not selected as the variables, of which errors are to be minimized, in inverse modelling. However, underestimations of GSD are seen with the LN model. The measured values of GMD and GSD before the UV lights are inaccurate due to the assumption of a log-normal background aerosol distribution mentioned before.

3.2.3 Simulation setup for the examination of the accuracy and the computational cost of the PL+LN model

To examine the accuracy and computational cost of the PL+LN model, the simulations using different models were performed using equal time series of $J(t)$ and $g(t)$ and equal time stepping. The time series obtained using the FS400 model are considered the best estimates to produce the measurement results due to the highest number of size sections modelled. Therefore, they were used as the time series for all the models used here, PL+LN, LN, FS400, MC100, FS35, and MC10. FS35 and MC10 denote a fixed-sectional model having 35 size sections and a moving-center fixed-sectional model having 10 size sections between 1.6 and 300 nm, respectively. These section number were used because they provide approximately the same computing times as the PL+LN model. Higher upper diameter limit for the FS35 and the MC10 models were chosen due to higher numerical diffusion associated to these models, which causes higher concentrations in large particle diameters compared to more accurate models. The time series of $J(t)$ and $g(t)$ used here are presented as fits in Figs. 7 and 8. The fitted functions were used rather than the time series because the time series having sharp edges would produce distributions having sharp edges as well, which would be unphysical. Here, the time series have sharp edges due to a very limited number of data points (Nano-SMPS scans) within the time domain. It is obvious that because the fits are not very near the time series, the outputs of the models will not be very near the measured data. Nevertheless, the fits were used because the purpose here is to examine the accuracy and the computational cost of the PL+LN model, which is done against the highly accurate models, the FS400 and the MC100 models. This comparison is the most properly done when all the models have the same functions for $J(t)$ and $g(t)$. The time domain to be simulated was split into 7953 time steps for all the models. The time splitting was obtained from the ODE45 solver used with the FS400 model. The time steps had the lengths of between 0 and 0.5 s, the shortest ones being in the beginning of the time domain.

The accuracy of the PL+LN model is examined by comparing the relative errors (δ_X) of the moments, N, S, and M, and the variables, GMD and GSD. The reference distributions used in the comparison are the distributions produced by the FS400

model and by the MC100 model, which are considered the models that most accurately conserve the number and the mass concentrations, respectively. The distributions from the FS400 model are used as the reference distribution when calculating δ_X for all the moments and variables, with the exception of the mass concentration, M, for which the MC100 model is used as the reference model. Because the distributions produced by the sectional models are considered here the correct ones rather than the measured distributions, the modelled distributions are used as the reference distributions. In this manner, the differences of the model outputs are caused by the models itself, e.g., due to numerical diffusion or some simplifications used in the model, not by how accurately they correspond with the measured data. The accuracies of the LN, FS35, and MC10 models are also examined.

All the other input parameters were the same as were used with the inverse modelling. The simulations used to examine the model accuracies provide also the possibility of comparing the computational costs of different models, because all the simulations were run using the same computer (Intel Core i5-3470 processor at 3.2 GHz) and had equal time stepping, and therefore equal number of computations of the general dynamic equation per a moment or a size section. Additionally, the sensitivity of the value of γ was examined using also the values of 0.1, 0.5, and 0.9, in addition to the value of 0.8.

4 Results and discussion

4.1 Theoretical test cases

Figure 10 shows the size distributions at the ends of the theoretical test simulations using different models. The distributions of the Atm cases during the whole time domain are presented as a video in the Supplement. It can be observed that the shape of the distribution produced by the PL+LN model is nearly equal to the reference distribution (FS1000). The largest deviations between the PL+LN distributions and the reference distributions are the gap between the PL and the LN distribution and the sharp peak in the PL distribution. These are most clearly seen in the Atm4 case where α is the highest. In the Atm5 case, the shape of the distribution produced by the FS1000 model is different: the distribution of the smallest particles do not follow a power law form due to low condensational growth rates near the particle diameter of D_1. Consequently, the PL+LN model is not able to express the distribution correctly at very small particle sizes. The effect of γ is also seen with the Atm5 case where the ratio of the concentrations of the LN distribution and of the PL distribution is higher due to higher γ. Conversely, the distributions produced by the LN model are far beyond the reference distributions. In the Atm4 and the Atm5 cases where new particle formation rates decrease towards the end of the simulation, the LN model begins to act better while the reference distribution transforms towards a log-normal shape.

The effect of the depositional losses can be seen as a decreased α in the Atm2 case compared to the Atm1 case. Because $k_{\text{dep}} > g$, the value of α becomes negative. Comparing the Atm3 case with the Atm2 case, it can be seen that the coagulational losses decrease α further. In the Atm4 and the Atm5 cases, the values of α are again increased compared to the Atm3 case. This occurs because $J(t)$ decreases with increasing time but g remains constant, in time, and thus there will be less small particles with increasing time. The distribution of the Exh case is mainly comparable to the Atm1 case with the exception of higher concentration levels in the Exh case due to higher $\frac{J}{g}$. It can be also observed that the ratio of the concentrations of the LN

distribution and of the PL distribution is higher in the Exh case than in the Atm1 case. This is due to increased coagulational transfer in the Exh case because it is calculated through the intramodal coagulation, of which rate is proportional to N_{PL}^2. The depositional and coagulational losses do not have significant effect on the distribution in the Exh case because $k_{\mathrm{dep}} \ll g$ and $N_{\mathrm{bg}} \ll N$.

Figure 11 shows the relative errors of the moments (δ_X) in the PL+LN model compared to the reference model, FS1000, as a function of time, and Tab. 2 at the ends of the test simulations. The highest relative errors of the total concentrations, N, S, and M, are usually met at the ends of the simulated time domains, and they are less than 2 % in all the cases, except the Atm5 case, the total number concentration N being the most accurately conserved moment. In the Atm5 case, $|\delta_X|$ for the moments are 17 % at the highest. The errors of this high level are caused by the reference distribution having features that do not fit well neither with the PL distribution nor with the LN distribution. The form of the size-dependence of the condensational growth rate in the Atm5 case represents, however, one of the worst cases that are to be simulated with the PL+LN model. For comparison, the parameters of the Atm5 case would cause $|\delta_X|$ to reach the levels of 24 % if the condensational transfer is neglected, the levels of 19 % if only the PL distribution is simulated, and the levels of 90 % if only the LN distribution is simulated. GMD and GSD have $|\delta_X|$ of less than 0.5 % in the cases with the constant parameters, but for the Atm4 and the Atm5 cases, the errors are higher (around $\pm 4\,\%$). All the cases, with the exception of the Atm5 case, can be simulated with the PL distribution only to achieve the levels of the relative errors as with the PL+LN distribution, but the need of the LN distribution in addition to the PL distribution arises with the Atm5 case. However, visually inspecting, the LN distribution is needed in all the cases to obtain distributions that have the correct shapes in the highest particle sizes.

The total computing time of the Atm5 case with the PL+LN model compared to the Atm4 case is approximately 2-fold, which is mainly caused by the need of numerical integration in calculation of the condensation terms in the Atm5 case. The associated computing time, and the accuracy, can be controlled by the number of size sections used in numerical integration or by using a polynomial form for the condensational growth rate. Because condensation is calculated using size sections with the FS1000 model, regardless of the size-dependency of the condensational growth rate, the total computing time increases only about 7 % when switching from size-independent condensational growth rates to size-dependent ones. The increase of the total computing time, in that case, is related to additional computations to obtain the values for the condensational growth rate itself.

4.2 Mobile aerosol chamber particle formation event

Particle size distributions obtained from the FS400, the LN, and the PL+LN models are shown as contour plots in Fig. 5 together with the measured distributions. Comparing the plots of the LN and the PL+LN models with the plot of the FS400 model, it can be seen that the PL+LN model behaves better for small diameters than the LN model. However, there is a sharp discontinuity between the PL and the LN distributions in the PL+LN model. In this case, the discontinuity is mainly formed due to the condensational transfer that is separating the distributions from each other. It is also seen that the PL+LN model is capable in vanishing the PL distribution when the aerosol ages and begins to have mainly a log-normal like form. Particle distributions 378 and 978 s after the UV lights were switched on are also shown in Fig. 12. The time $t = 378\,\mathrm{s}$ presents the center of the Nano-SMPS scan where the new particle formation rate is at the highest. At the time $t = 978\,\mathrm{s}$, new particle

formation was mostly quenched but growth still occurred. The shapes of the distributions produced by the PL+LN model are near the reference distributions (FS400) with the exception of the gaps between the PL and the LN distributions. The shapes of the distributions at the largest particles produced by the LN model correspond better with the measured distributions than at the smallest particles. In the simulation using the FS35 model, a high numerical diffusion that widens the distribution towards the larger particles is seen. The distributions produced by the MC models, MC100 and MC10, have sharp features but follow the distributions produced by the FS400 model. The number of size sections in the MC10 model is obviously too low to plot the distributions well. The modelled distributions at the time $t = 978\,\mathrm{s}$ are not very near the measured distribution due to the fitted functions used for $J(t)$ and $g(t)$.

Table 3 presents the computational costs and the accuracies of the models. Computing times are reported relative to the computing time of the PL+LN simulation, 24 s. The PL+LN model has the best accuracy for the total number (N) and mass (M) concentrations compared to the sectional models with approximately the same computing time (FS35 and MC10) and to the LN model. The FS35 model is relatively accurate in N output but suffers from high numerical diffusion seen as high relative error (79 %) in M. The PL+LN model has also low memory consumption due to a low number of variables. The LN model is, however, the most computationally efficient but the relative errors are high too (up to 17 % in N).

The development of N, M, GMD, GSD, and the relative errors of N and M are shown in Fig. 13. It can be seen that the PL+LN model has nearly the same output for N as the reference models during the whole time domain. The beginning of the overestimation of N in the LN and in the MC10 models are clearly seen at the region where the new particle formation has the highest rate ($t \approx 400\,\mathrm{s}$). The LN model functions better in M, but overestimations are encountered with the MC10 model. In addition to the MC10 model, the FS35 model overestimates M clearly. The PL+LN model outputs M very accurately during the whole time domain. GMD is overestimated slightly with the FS35 and the MC10 models due to numerical diffusion, but the PL+LN and the LN models output it accurately during the whole time domain. The highest error in GMD produced by the PL+LN model is the underestimation of 1.3 % compared to the FS400 model which occurs at the time of the highest new particle formation rate. The highest deviations between the models are seen in the development of GSD. The PL+LN model underestimates GSD with 3 % at the end of the time domain, but the FS35 model overestimates it significantly and the MC10 model and the LN model underestimate it significantly. Additionally, the MC10 model suffers from uneven behavior due to its low number of size sections. The relative errors of the moments, δ_N and δ_M, are at the highest levels mostly at the ends of the simulations. The models having at least the same computational efficiency as the PL+LN model (the FS35, the MC10, and the LN models) fail to produce N and M accurately: the relative errors can be up to tens of percent. The relative errors with the PL+LN model are below 2 % during the whole time domain. In conclusion, the PL+LN model has the best accuracy for the production of N, M, GMD, and GSD during the whole time domain compared to the other models having at least the same computational efficiency.

Figure 14 presents the particle distribution at the time of $t = 978\,\mathrm{s}$ using the PL+LN model with different values of γ. It can be seen that the PL distribution in the total distribution is mostly dominating when a low value for γ is used (left pane). Conversely, using a high value of γ (right pane) produces a more log-normal like form, which, at least in this case, corresponds best with the measured distribution. However, a gap between the PL and the LN distributions is larger in cases of high values

of γ. The sensitivity of the value of γ is also shown in Tab. 4, in which the relative errors of N, M, GMD, and GSD are reported. It can be seen that a value near 0.8 provides the most accurate results, depending on the variable of the main interest. By comparing the errors of N and M produced by the PL+LN model with the errors produced by different models reported in Tab. 3, it can be seen that the lowest errors for N and M simultaneously are produced by the PL+LN model regardless of the value of γ used. Contour plots with different values of γ are shown in Fig. 15. By visual inspection, it can be seen that the values 0.5 and 0.8 produce the contour plots being the closest to the measured contour plot in Fig. 5.

5 Conclusions

The combined power law and log-normal distribution (PL+LN) model was developed to represent a particle size distribution in simultaneous new particle formation and growth situation, in which log-normal distributions do not represent the aerosol sufficiently well. The PL+LN distribution combines a power law form typical to simultaneous new particle formation and growth situation at the initial steps of aerosol formation with a log-normal form typical to aged aerosols. The PL+LN model is useful in simulations involving the initial steps of aerosol formation where a sectional representation of the size distribution causes too high computational cost, such as in multidimensional simulations or in the case of using inverse modelling to obtain the best estimates for parameters used as input in the model. These parameters can be, e.g., the new particle formation rate or the condensational growth rate that the most accurately produce the distributions as the measured ones. The model uses six moment variables to model the distribution, denoting lower memory consumption compared to sectional models which require tens or hundreds variables. The model includes simultaneous new particle formation, condensation, coagulation, coagulational loss, and depositional loss processes.

The PL+LN model was evaluated using theoretical test simulations and a real-world particle formation event simulation. The test cases represented particle formation events with the parameters related to the atmosphere and to vehicle exhaust. The real-world case was the simulation of a particle formation event measurement performed in a mobile aerosol chamber at Mäkelänkatu street canyon measurement site in Helsinki, Finland. The evaluation was done against highly accurate sectional models using fixed-sectional and moving-center fixed-sectional methods. The accuracy of the total number, surface area, and mass concentrations simulated by the PL+LN model was examined: the relative errors of the concentrations were lower than $2\,\%$ compared to the highly accurate sectional models, with the exception of a theoretical test case having size-dependent condensational growth rate with which the relative errors were up to $17\,\%$ due to the shape of the size distribution produced. The performance of producing geometric mean diameter (GMD) and geometric standard deviation (GSD) of the total distributions using different models was also examined: the highest relative error with the PL+LN model was $3.5\,\%$ for GMD when size-dependent new particle formation rate was modelled in a theoretical test case. The shapes of the distributions produced by the PL+LN model were noticeably more similar to the reference distributions than produced by a simple log-normal distribution model.

Considering the same computing time as the PL+LN model in the chamber event simulation, only 35 size sections for a fixed-sectional model and 10 size sections for a moving-center fixed-sectional model were allowed to be modelled. With these

section numbers, the results for the number and mass concentrations, for GMD, and for GSD were not as accurate as using the PL+LN model: the relative errors were up to tens of percent. Additionally, a simple log-normal distribution model seemed to output GMD relatively well in this case, but the number concentration was overestimated and GSD was underestimated during almost the whole time domain, especially at times when new particle formation and growth occurred simultaneously.

The new particle formation rates, $J(t)$, and the condensational growth rates, $g(t)$, used in the chamber simulation were obtained through inverse modelling. Firstly, the PL+LN and the LN models were used to obtain the best estimates for $J(t)$ and $g(t)$ that produce the measured concentrations the most accurately. Secondly, the time series of $J(t)$ and $g(t)$ obtained using the PL+LN model were used as initial guesses in the inverse modelling with the highly accurate models. Only minor differences were found in the time series of $J(t)$ and $g(t)$ obtained using different models: the PL+LN model overestimates and the LN model underestimates $J(t)$ slightly. The associated computing times using the highly accurate sectional models are approximately 2 orders of magnitude longer compared to the PL+LN model. Therefore, the PL+LN model provides a rapid and accurate solution to obtain input parameters, such as new particle formation and condensational growth rates, from the measured data through inverse modelling.

Appendix A: Gaussian quadratures

The Hermite-Gauss quadrature (Steen et al., 1969) is used in the integrals involving the LN distribution, as the density function of the LN distribution, Eq. (8), is in the form of the weight function of the Hermite-Gauss quadrature e^{-x^2}. E.g., an integral

$$\int_{-\infty}^{\infty} D_\mathrm{p}^2\, g(t, D_\mathrm{p})\, \frac{\mathrm{d}N}{\mathrm{d}\ln D_\mathrm{p}}\bigg|_\mathrm{LN} \mathrm{d}\ln D_\mathrm{p} = \frac{N_\mathrm{LN}}{\sqrt{2\pi}\ln\sigma} \int_{-\infty}^{\infty} D_\mathrm{p}^2\, g(t, D_\mathrm{p}) \exp\left[-\frac{\ln^2(D_\mathrm{p}/D_\mathrm{g})}{2\ln^2\sigma}\right] \mathrm{d}\ln D_\mathrm{p} \tag{A1}$$

becomes, using the Hermite-Gauss quadrature,

$$\frac{N_\mathrm{LN}}{\sqrt{\pi}} \sum_{j=1}^{n} w_j D_\mathrm{p}^2\, g(t, D_j) \tag{A2}$$

where D_j and w_j are the abscissa and the weight for the bin j obtained from the quadrature, and n is the degree of the quadrature. In this article, the degree of $n = 5$ is used for the LN distribution denoting that the integrals are calculated with five diameter values. The integrals involved in the PL distribution are in the form of D_p^α which is not a weight function of any specific quadrature; therefore, a Gaussian quadrature for this purpose was developed. E.g., an integral

$$\int_{-\infty}^{\infty} D_\mathrm{p}^2\, g(t, D_\mathrm{p})\, \frac{\mathrm{d}N}{\mathrm{d}\ln D_\mathrm{p}}\bigg|_\mathrm{PL} \mathrm{d}\ln D_\mathrm{p} = \frac{N_\mathrm{PL}\alpha}{D_2^\alpha - D_1^\alpha} \int_{\ln D_1}^{\ln D_2} D_\mathrm{p}^2\, g(t, D_\mathrm{p})\, D_\mathrm{p}^\alpha\, \mathrm{d}\ln D_\mathrm{p} \tag{A3}$$

becomes, using the quadrature developed here,

$$\frac{N_\mathrm{PL}\ln d^\alpha}{d^\alpha - 1} \sum_{j=1}^{n} w_j D_\mathrm{p}^2\, g(t, D_j) \tag{A4}$$

where D_j and w_j are the abscissa and the weight for the bin j obtained from the quadrature. The degree of $n = 4$ is used for the PL distribution.

The degree of the quadrature developed here, $n = 4$, is relatively low, but by using higher degrees, internal equations in the quadrature will become more complicated which results in increased computing time. In the cases described in this article, the degree of 4 results in the absolute relative errors of the condensation and the coagulation terms less than 10^{-2} compared to a very high degree numerical integration or, if exists, to an analytical solution, but only when $\alpha > 0.5$, in the case of the condensation terms, and when $d < 3$, in the case of the coagulation terms. A drawback of the quadrature with a low degree is that with the values of $\alpha < 0.5$ (condensation) and $d > 3$ (coagulation), errors increase, which causes numerical problems during a simulation. Therefore, the quadrature is used only with the values of $\alpha < 0.5$ (condensation) or $d < 3$ (coagulation), but numerical integration as in Eq. (23) otherwise, or, if exists, an analytical solution for the condensation terms as in Eq. (22). In numerical integration, $n = 200$ size sections are used for condensation calculation, which is required to produce the absolute relative errors less than 10^{-2}. Calculating coagulation using numerical integration, $n = 20$ is used. However, with only 20 size sections, relative errors increase up to 30 % when d increases towards 100 and α towards ± 5. Nevertheless, a higher degree is not used due to increasing computing time, which is squarely proportional to the number of size sections due to double integrals in the coagulation terms. Therefore, the degrees are kept low to maintain computational efficiency. To produce the same accuracy by using numerical integration with n size sections as by using the quadrature with the degree of 4 for the PL distribution, with the values of α and d where the quadrature is applicable, about 1 or 2 orders of magnitude longer computing time is consumed. The degree for the Hermite-Gauss quadrature, $n = 5$, can be increased easily without encountering steep increases to computing time; nevertheless, in the cases of this article, $n = 5$ produces the absolute relative errors of less than 10^{-4} for the condensation and the coagulation terms.

Acknowledgements. This work was funded by the Maj and Tor Nessling Foundation (project number 2014452), by Tampere University of Technology Graduate School, and by the Finnish Funding Agency for Technology and Innovation (Tekes) as a part of the CLEEN MMEA program. Authors acknowledge the personal of the Air Protection Group at the Helsinki Region Environmental Services Authority (HSY) for enabling the measurement campaign at the HSY's street canyon measurement site in Helsinki.

References

Adams, P. and Seinfeld, J.: Predicting global aerosol size distributions in general circulation models, J. Geophys. Res.-Atmos., 107, AAC 4–1–AAC 4–23, doi:10.1029/2001JD001010, 2002.

Barrett, J. and Webb, N.: A comparison of some approximate methods for solving the aerosol general dynamic equation, J. Aerosol Sci., 29, 31–39, doi:10.1016/S0021-8502(97)00455-2, 1998.

Dahneke, B.: Simple kinetic theory of Brownian diffusion in vapors and aerosols, in: Theory of Dispersed Multiphase Flow, edited by Meyer, R. E., pp. 97–133, Academic Press, doi:10.1016/B978-0-12-493120-6.50011-8, 1983.

Friedlander, S. K.: Smoke, dust, and haze: Fundamentals of aerosol dynamics, Oxford University Press, New York, USA, 2nd edn., 2000.

Hinds, W. C.: Aerosol technology: properties, behavior, and measurement of airborne particles, John Wiley & Sons, Inc., Hoboken, USA, 2nd edn., 1999.

Hussein, T., Hruška, A., Dohányosová, P., Džumbová, L., Hemerka, J., Kulmala, M., and Smolík, J.: Deposition rates on smooth surfaces and coagulation of aerosol particles inside a test chamber, Atmos. Environ., 43, 905–914, doi:10.1016/j.atmosenv.2008.10.059, 2009.

Jacobson, M.: Development and application of a new air pollution modeling system–II. Aerosol module structure and design, Atmos. Environ., 31, 131–144, doi:10.1016/1352-2310(96)00202-6, 1997.

Kannosto, J., Virtanen, A., Lemmetty, M., Mäkelä, J. M., Keskinen, J., Junninen, H., Hussein, T., Aalto, P., and Kulmala, M.: Mode resolved density of atmospheric aerosol particles, Atmos. Chem. Phys., 8, 5327–5337, doi:10.5194/acp-8-5327-2008, 2008.

Kerminen, V.-M. and Kulmala, M.: Analytical formulae connecting the "real" and the "apparent" nucleation rate and the nuclei number concentration for atmospheric nucleation events, J. Aerosol Sci., 33, 609–622, doi:10.1016/S0021-8502(01)00194-X, 2002.

Kulmala, M., Vehkamäki, H., Petäjä, T., Maso, M. D., Lauri, A., Kerminen, V.-M., Birmili, W., and McMurry, P.: Formation and growth rates of ultrafine atmospheric particles: a review of observations, J. Aerosol Sci., 35, 143–176, doi:10.1016/j.jaerosci.2003.10.003, 2004.

Kulmala, M., Riipinen, I., Sipilä, M., Manninen, H. E., Petäjä, T., Junninen, H., Dal Maso, M., Mordas, G., Mirme, A., Vana, M., Hirsikko, A., Laakso, L., Harrison, R. M., Hanson, I., Leung, C., Lehtinen, K. E. J., and Kerminen, V.-M.: Toward direct measurement of atmospheric nucleation, Science, 318, 89–92, doi:10.1126/science.1144124, 2007.

Kulmala, M., Kontkanen, J., Junninen, H., Lehtipalo, K., Manninen, H., Nieminen, T., Petäjä, T., Sipilä, M., Schobesberger, S., Rantala, P., Franchin, A., Jokinen, T., Järvinen, E., Äijälä, M., Kangasluoma, J., Hakala, J., Aalto, P., Paasonen, P., Mikkilä, J., Vanhanen, J., Aalto, J., Hakola, H., Makkonen, U., Ruuskanen, T., Mauldin III, R., Duplissy, J., Vehkamäki, H., Bäck, J., Kortelainen, A., Riipinen, I., Kurtén, T., Johnston, M., Smith, J., Ehn, M., Mentel, T., Lehtinen, K., Laaksonen, A., Kerminen, V.-M., and Worsnop, D.: Direct observations of atmospheric aerosol nucleation, Science, 339, 943–946, doi:10.1126/science.1227385, 2013.

Lai, A. and Nazaroff, W.: Modeling indoor particle deposition from turbulent flow onto smooth surfaces, J. Aerosol Sci., 31, 463–476, doi:10.1016/S0021-8502(99)00536-4, 2000.

Lehtinen, K. E. J. and Kulmala, M.: A model for particle formation and growth in the atmosphere with molecular resolution in size, Atmos. Chem. Phys., 3, 251–257, doi:10.5194/acp-3-251-2003, 2003.

Lehtinen, K. E. J., Dal Maso, M., Kulmala, M., and Kerminen, V.-M.: Estimating nucleation rates from apparent particle formation rates and vice versa: Revised formulation of the Kerminen-Kulmala equation, J. Aerosol Sci., 38, 988–994, doi:10.1016/j.jaerosci.2007.06.009, 2007.

McGraw, R.: Description of aerosol dynamics by the quadrature method of moments, Aerosol Sci. Tech., 27, 255–265, doi:10.1080/02786829708965471, 1997.

Mitrakos, D., Hinis, E., and Housiadas, C.: Sectional modeling of aerosol dynamics in multi-dimensional flows, Aerosol Sci. Tech., 41, 1076–1088, doi:10.1080/02786820701697804, 2007.

Mordas, G., Manninen, H., Petäjä, T., Aalto, P., Hämeri, K., and Kulmala, M.: On operation of the ultra-fine water-based CPC TSI 3786 and comparison with other TSI models (TSI 3776, TSI 3772, TSI 3025, TSI 3010, TSI 3007), Aerosol Sci. Tech., 42, 152–158, doi:10.1080/02786820701846252, 2008.

Olin, M., Rönkkö, T., and Dal Maso, M.: CFD modeling of a vehicle exhaust laboratory sampling system: sulfur-driven nucleation and growth in diluting diesel exhaust, Atmos. Chem. Phys., 15, 5305–5323, doi:10.5194/acp-15-5305-2015, 2015.

Riipinen, I., Sihto, S.-L., Kulmala, M., Arnold, F., Dal Maso, M., Birmili, W., Saarnio, K., Teinilä, K., Kerminen, V.-M., Laaksonen, A., and Lehtinen, K. E. J.: Connections between atmospheric sulphuric acid and new particle formation during QUEST III–IV campaigns in Heidelberg and Hyytiälä, Atmos. Chem. Phys., 7, 1899–1914, doi:10.5194/acp-7-1899-2007, 2007.

Rönkkö, T., Virtanen, A., Vaaraslahti, K., Keskinen, J., Pirjola, L., and Lappi, M.: Effect of dilution conditions and driving parameters on nucleation mode particles in diesel exhaust: Laboratory and on-road study, Atmos. Environ., 40, 2893–2901, doi:10.1016/j.atmosenv.2006.01.002, 2006.

Rönkkö, T., Lähde, T., Heikkilä, J., Pirjola, L., Bauschke, U., Arnold, F., Schlager, H., Rothe, D., Yli-Ojanperä, J., and Keskinen, J.: Effects of gaseous sulphuric acid on diesel exhaust nanoparticle formation and characteristics, Environ. Sci. Technol., 47, 11 882–11 889, doi:10.1021/es402354y, 2013.

Seinfeld, J. and Pandis, S.: Atmospheric chemistry and physics: From air pollution to climate change, John Wiley and Sons, Inc., New York, USA, 2nd edn., 2006.

Sihto, S.-L., Kulmala, M., Kerminen, V.-M., Dal Maso, M., Petäjä, T., Riipinen, I., Korhonen, H., Arnold, F., Janson, R., Boy, M., Laaksonen, A., and Lehtinen, K. E. J.: Atmospheric sulphuric acid and aerosol formation: implications from atmospheric measurements for nucleation and early growth mechanisms, Atmos. Chem. Phys., 6, 4079–4091, doi:10.5194/acp-6-4079-2006, 2006.

Steen, N., Byrne, G., and Gelbard, E.: Gaussian quadratures for the integrals $\int_0^\infty \exp(-x^2) f(x) dx$ and $\int_0^b \exp(-x^2) f(x) dx$, Math. Comp., 23, 661–671, 1969.

Tammet, H. and Kulmala, M.: Performance of four-parameter analytical models of atmospheric aerosol particle size distribution, J. Aerosol Sci., 77, 145 – 157, doi:10.1016/j.jaerosci.2014.08.001, 2014.

Uhrner, U., von Löwis, S., Vehkamäki, H., Wehner, B., Bräsel, S., Hermann, M., Stratmann, F., Kulmala, M., and Wiedensohler, A.: Dilution and aerosol dynamics within a diesel car exhaust plume-CFD simulations of on-road measurement conditions, Atmos. Environ., 41, 7440–7461, doi:10.1016/j.atmosenv.2007.05.057, 2007.

Vanhanen, J., Mikkilä, J., Lehtipalo, K., Sipilä, M., Manninen, H. E., Siivola, E., Petäjä, T., and Kulmala, M.: Particle size magnifier for nano-CN detection, Aerosol Sci. Tech., 45, 533–542, doi:10.1080/02786826.2010.547889, 2011.

Verheggen, B. and Mozurkewich, M.: An inverse modeling procedure to determine particle growth and nucleation rates from measured aerosol size distributions, Atmos. Chem. Phys., 6, 2927–2942, doi:10.5194/acp-6-2927-2006, 2006.

Wang, Y. and Zhang, K.: Coupled turbulence and aerosol dynamics modeling of vehicle exhaust plumes using the CTAG model, Atmos. Environ., 59, 284–293, doi:10.1016/j.atmosenv.2012.04.062, 2012.

Whitby, E. and McMurry, P.: Modal aerosol dynamics modeling, Aerosol Sci. Tech., 27, 673–688, doi:10.1080/02786829708965504, 1997.

Wu, C.-Y. and Biswas, P.: Study of numerical diffusion in a discrete-sectional model and its application to aerosol dynamics simulation, Aerosol Sci. Tech., 29, 359–378, doi:10.1080/02786829808965576, 1998.

Table 1. Input parameters for the test cases. Case names with Atm have the parameter sets related to atmospheric particle formation and the Exh case related to particle formation occurring in vehicle exhaust. J and g are the new particle formation rate and the condensational growth rate, respectively. N_{bg} is the concentration of the background aerosol distribution having a count median diameter of $\mathrm{CMD}_{\mathrm{bg}}$. The coagulational loss exponent l_{bg} depend on the value of $\mathrm{CMD}_{\mathrm{bg}}$. Wall deposition is modelled using the deposition coefficient k_{dep}. The length of the simulated time domain is t_{max}.

Case	J ($\mathrm{cm^{-3}\,s^{-1}}$)	g	T (K)	Coagulation	N_{bg} ($\mathrm{cm^{-3}}$)	$\mathrm{CMD}_{\mathrm{bg}}$ (nm)	l_{bg}	k_{dep}	γ	t_{max}
Atm1	0.1	$1\,\mathrm{nm\,h^{-1}}$	280	intra, inter	0	–	–	0	0	5 h
Atm2	0.1	$1\,\mathrm{nm\,h^{-1}}$	280	intra, inter	0	–	–	$1.8\,\mathrm{nm\,h^{-1}}$	0	5 h
Atm3	0.1	$1\,\mathrm{nm\,h^{-1}}$	280	intra, inter, bg	10^3	100	-1.6	$1.8\,\mathrm{nm\,h^{-1}}$	0	5 h
Atm4	Eq. (50)	$1\,\mathrm{nm\,h^{-1}}$	280	intra, inter, bg	10^3	100	-1.6	$1.8\,\mathrm{nm\,h^{-1}}$	0	5 h
Atm5	Eq. (50)	Eqs. (16) – (18)	280	intra, inter, bg	10^3	100	-1.6	$1.8\,\mathrm{nm\,h^{-1}}$	0.25	5 h
Exh	10^8	$5\,\mathrm{nm\,s^{-1}}$	500	intra, inter, bg	10^6	60	-1.5	$0.07\,\mathrm{nm\,s^{-1}}$	0	1 s

Table 2. Relative errors, δ_X (%), of the variables at the ends of the test case simulations using the PL+LN model compared to the variables produced by the fixed-sectional model with 1000 size sections. The input parameter sets are shown in Tab. 1. N, S, and M are the number, the surface area, and the mass concentration of the total particle distribution, respectively. GMD and GSD are the geometric mean diameter and the geometric standard deviation of the distribution.

Case	N	S	M	GMD	GSD
Atm1	-0.001	-0.310	-0.573	+0.068	-0.193
Atm2	-0.052	-0.481	-0.838	-0.083	-0.039
Atm3	+0.173	-0.884	-1.296	-0.086	-0.505
Atm4	+0.202	-0.816	-1.518	+0.933	-1.251
Atm5	+6.957	-2.384	-7.666	-3.511	-2.879
Exh	+0.007	-0.356	-0.680	+0.084	+0.011

Table 3. Computational costs of different models and relative errors of number (N) and mass (M) concentrations obtained from the time of 1663 s after the UV lights were switched on in the chamber simulation. The number of variables compared to size sections in MC models is 2-fold because the centers of the size sections need to be stored in addition to the concentrations of the sections. Relative values are calculated using a model with (ref.) as the reference model.

Model name	Method	Size sections	Variables	Relative computing time	Error in N (%)	Error in M (%)
FS35	fixed-sectional	35	35	1.0	+1.6	+79
MC10	moving-center	10	20	1.0	+18	+29
LN	log-normal	-	3	0.09	+17	+6.4
PL+LN	combined PL and LN	-	6	1.0 (ref.)	+0.48	-1.2
FS400	fixed-sectional	400	400	170	0 (ref.)	+3.4
MC100	moving-center	100	200	200	+0.31	0 (ref.)

Table 4. Relative errors (%) of the variables in the chamber simulation with the PL+LN model using different values for the condensational transfer factor γ. The errors are compared to the FS400 model, except for M that is compared to the MC100 model.

γ	N	M	GMD	GSD
0.1	-1.2	-7.8	+2.6	-5.8
0.5	+0.75	-2.7	-3.7	+3.4
0.8	+0.48	-1.2	-0.33	-2.8
0.9	+2.6	-0.43	-0.11	-6.0

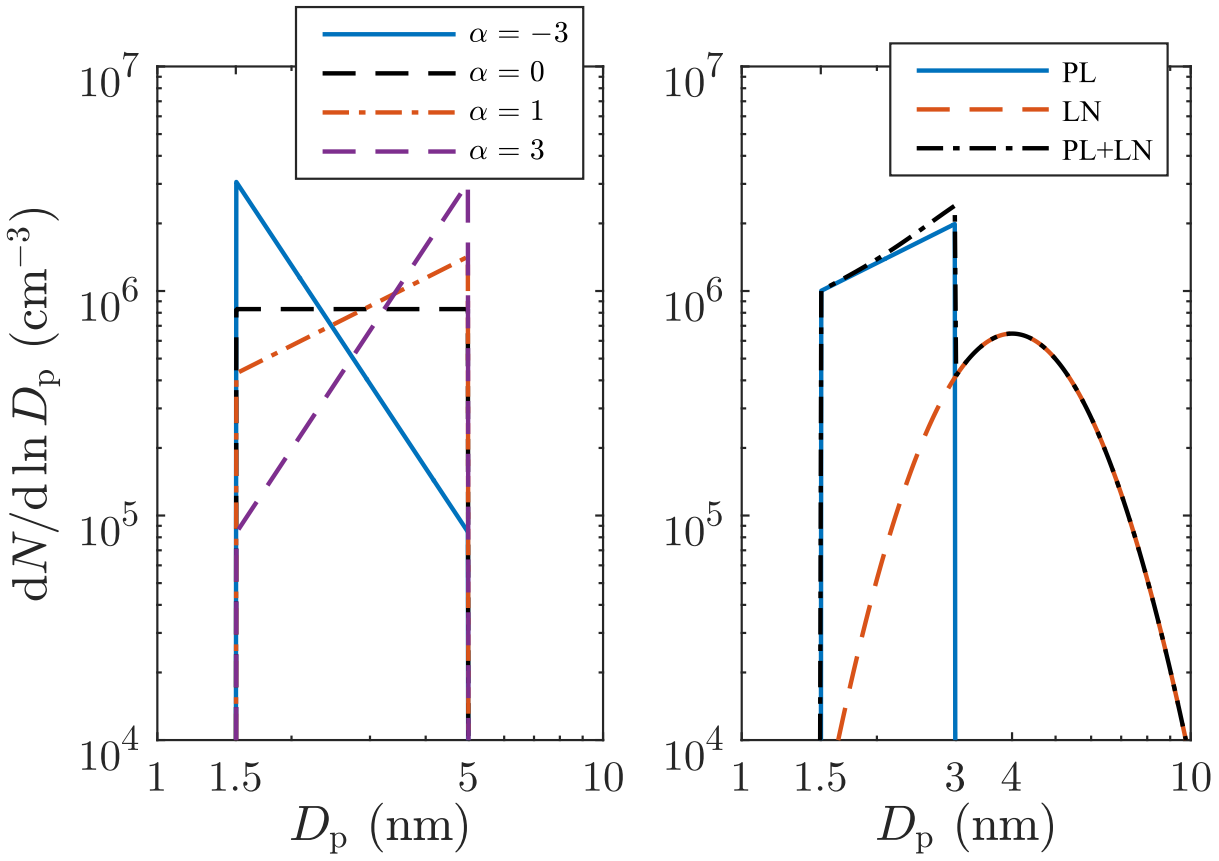

Figure 1. Left pane shows examples of power law distributions with different values of the slope parameter α. Right pane shows the combination of a power law (PL) and a log-normal (LN) distribution (PL+LN).

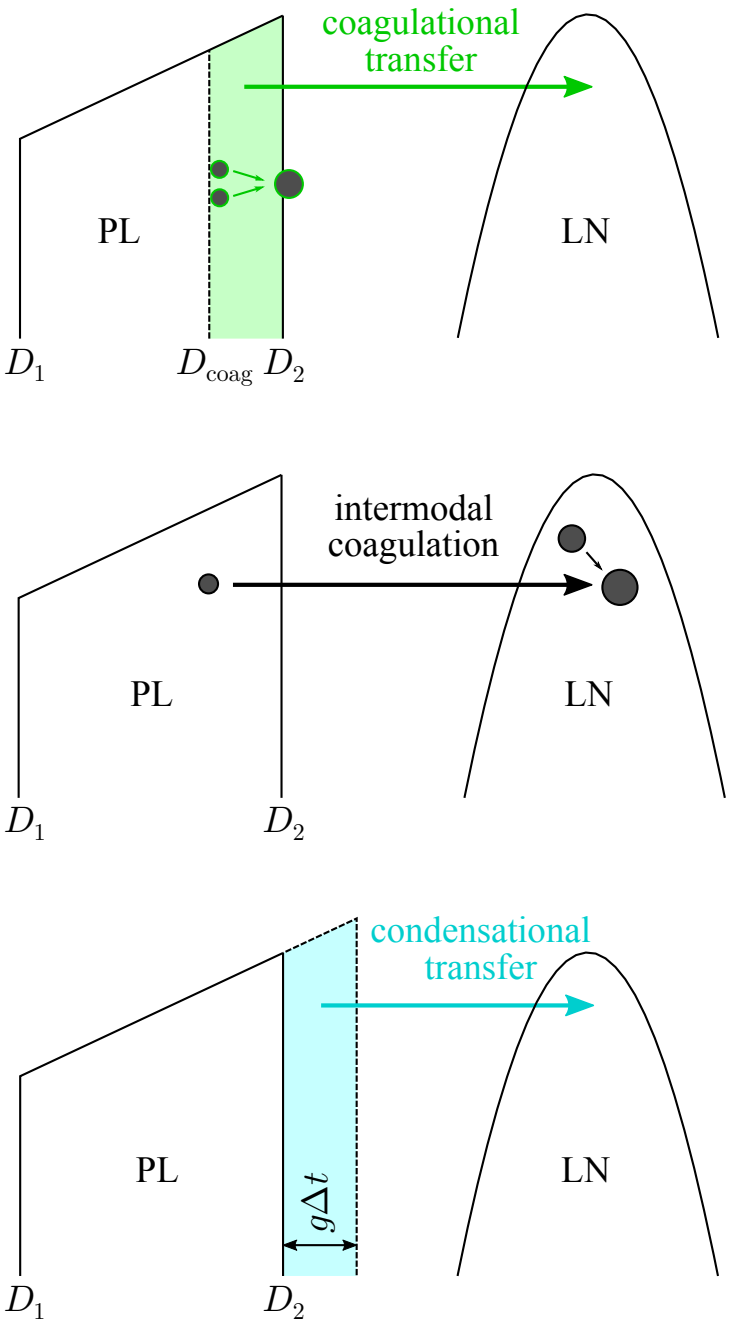

Figure 2. Intermodal processes between the PL and the LN distributions. Particles larger than D_{coag} (green area) form particles larger than D_2 by the intramodal coagulation in the PL distribution; the coalesced resultant particles are transferred to the LN distribution. When the LN distribution exists, particles of the both distributions begin to coagulate intermodally; the resultant particles are assigned to the LN distribution. Condensation grows the largest particle diameter by $g\Delta t$ in a time step of Δt, but the condensational transfer transfers a part of the particles larger than D_2 (blue area) to the LN distribution.

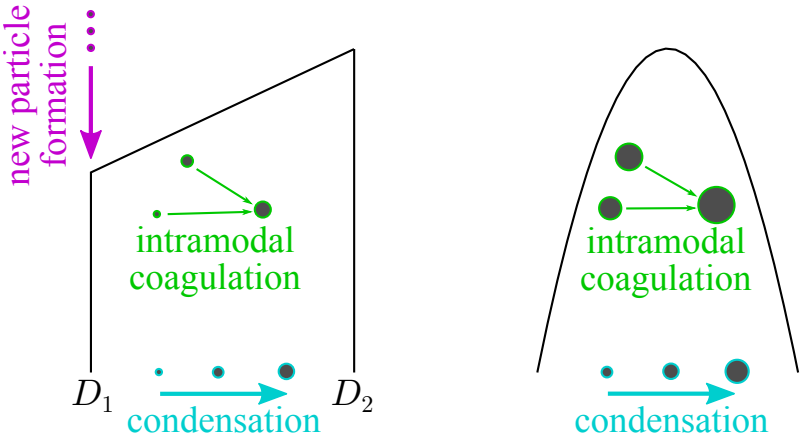

Figure 3. Intramodal processes. New particle formation forms particles with the diameter of D_1 to the PL distribution. Condensation and intramodal coagulation grow particles within a distribution.

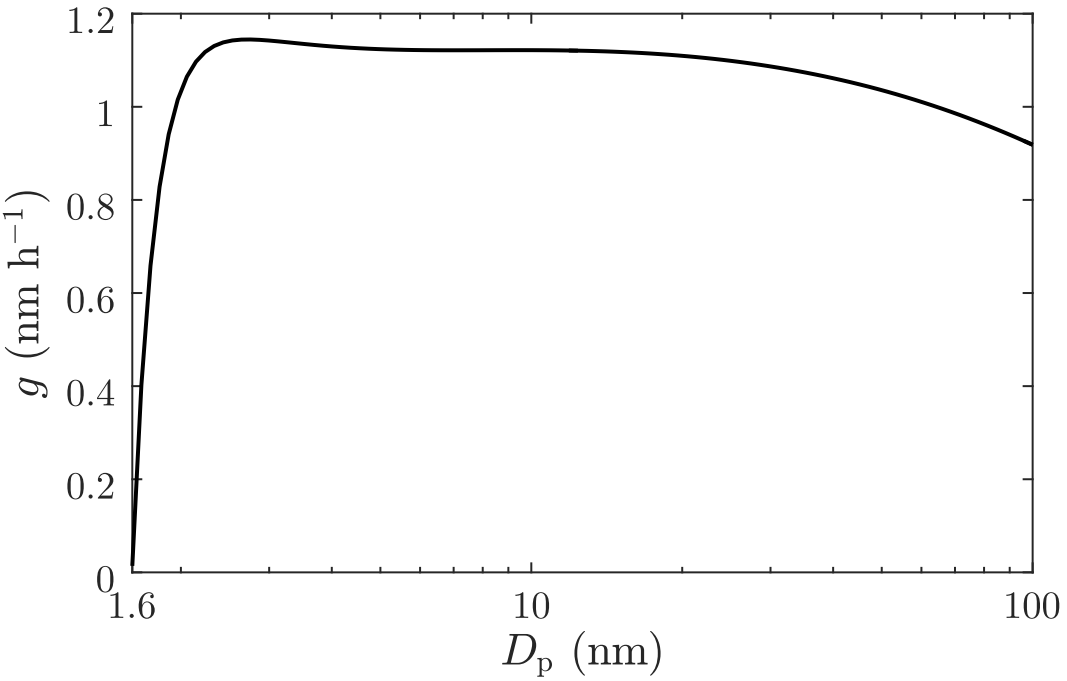

Figure 4. Size-dependent condensational growth rate of sulfuric acid-water particles with the sulfuric acid vapor concentration of $0.8 \times 10^7\,\mathrm{cm}^{-3}$, temperature of 280 K, and relative humidity of 60 % as a function of the particle diameter, used in the Atm5 case.

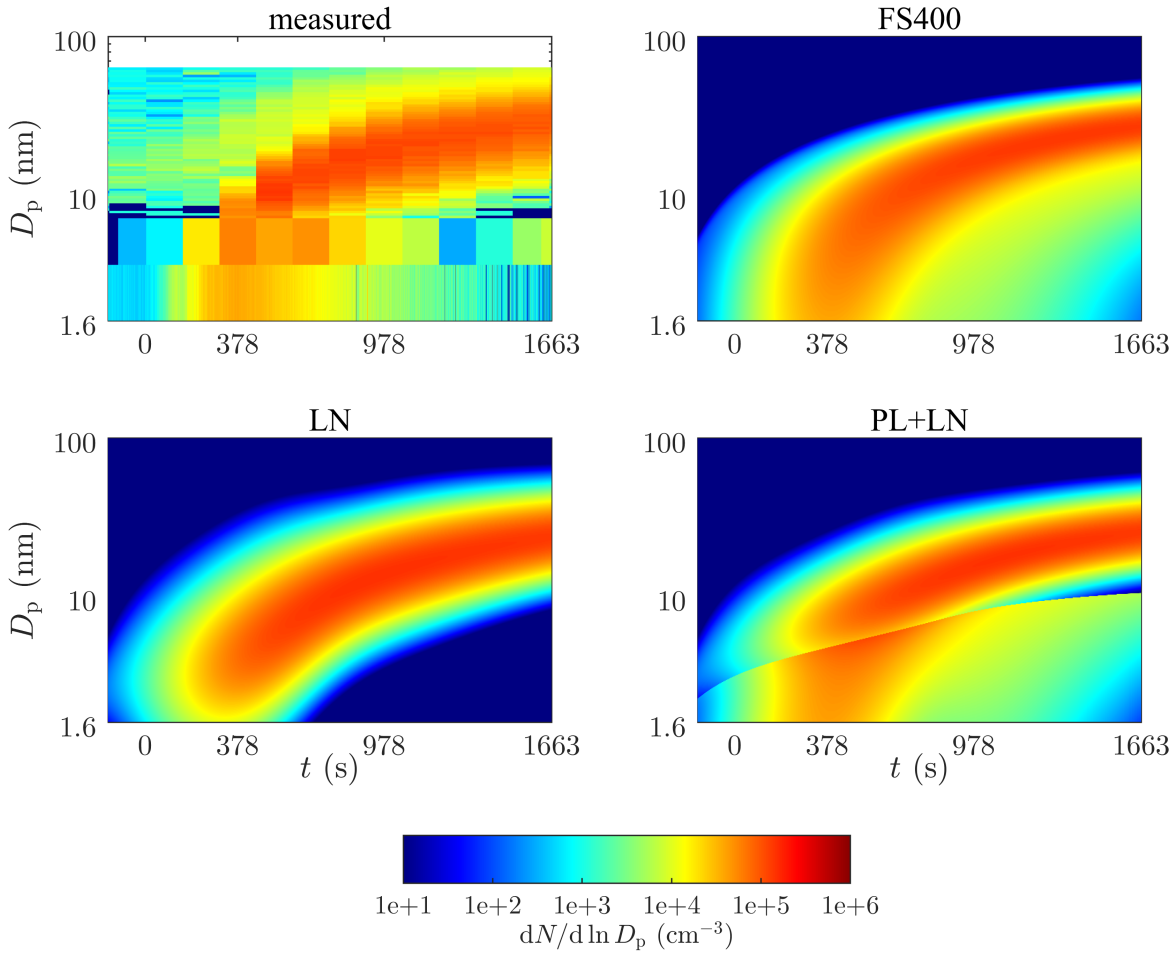

Figure 5. Contour plots of particle distributions measured by PSM, CPC, and Nano-SMPS and simulated by different models in the chamber event. FS400 denotes the fixed-sectional model with 400 size sections. The value of 0.8 was used for γ with the PL+LN model. The UV lights were switched on at time $t = 0\,\mathrm{s}$. Note that the background particle distribution seen in the measured data was excluded from the simulations.

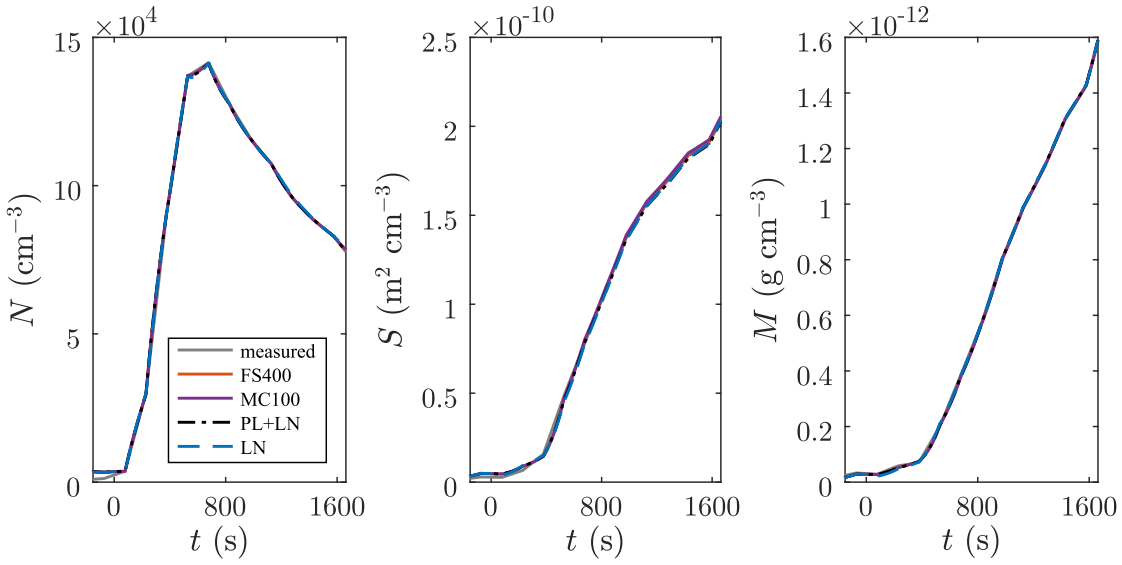

Figure 6. Number (N), surface area (S), and mass (M) concentrations of the nucleation mode in the chamber event. The measured concentrations and the concentrations produced during inverse modelling using different models are nearly equal. The data are shown for the centers of the Nano-SMPS scans only, because those values only are used in inverse modelling. MC100 denotes the moving-center fixed-sectional model with 100 size sections.

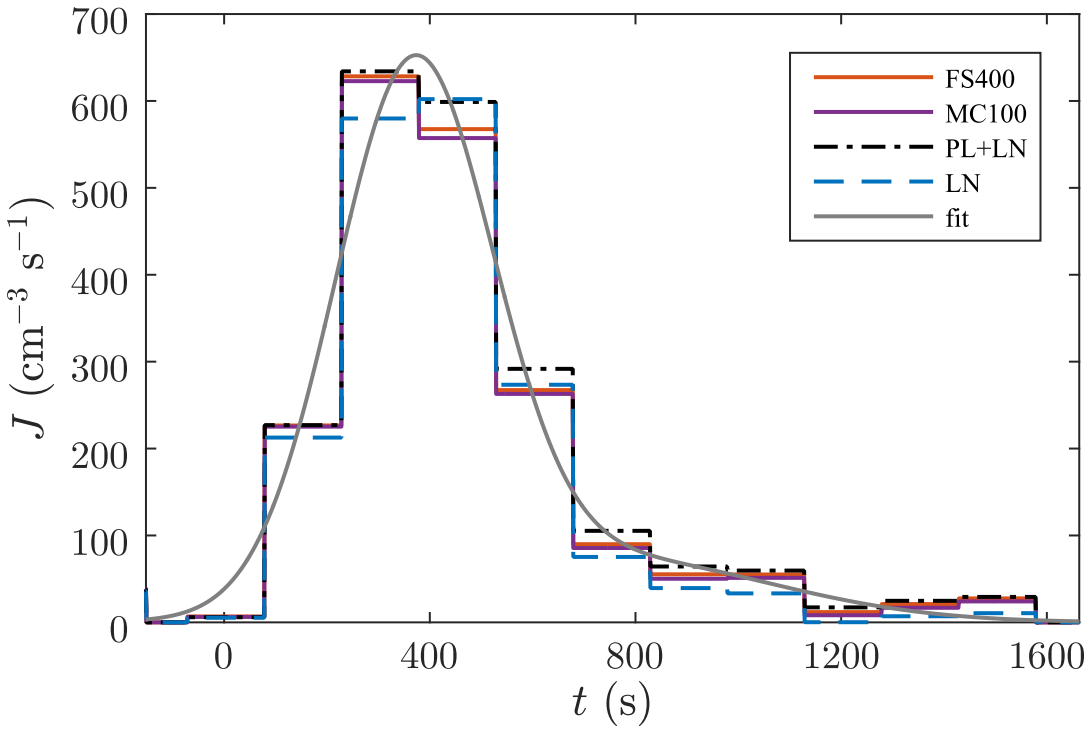

Figure 7. Time series for the new particle formation rates in the chamber event that produce the measured concentrations, N, S, and M, the most accurately compared to the measured ones, using different models. The fit denotes a bell-shaped function fitted to the values from the FS400 model.

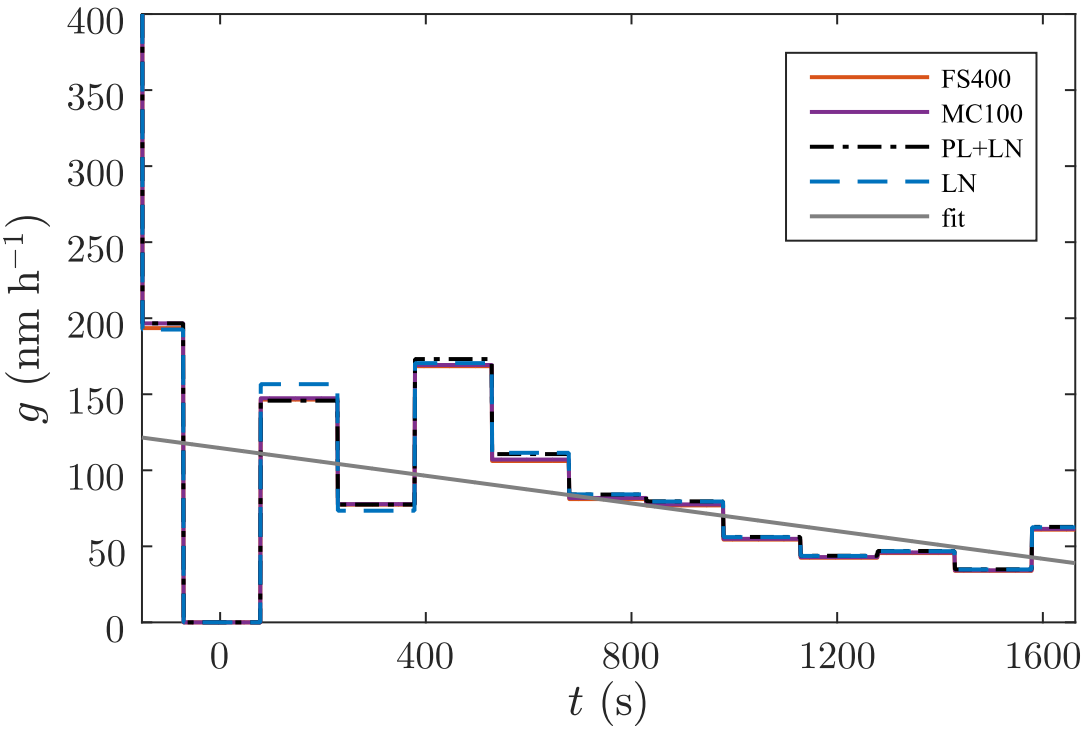

Figure 8. Time series for the condensational growth rates in the chamber event that produce the measured concentrations, N, S, and M, the most accurately compared to the measured ones, using different models. The fit denotes a linear function fitted to the values from the FS400 model.

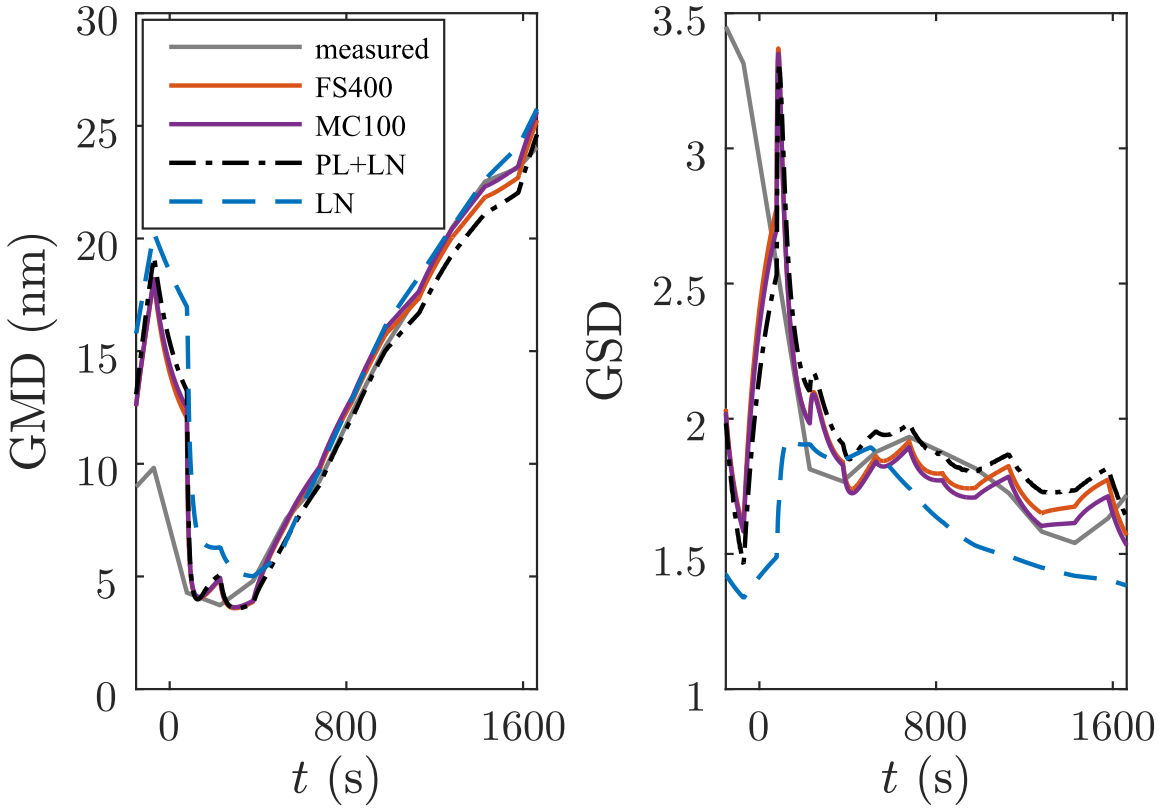

Figure 9. Geometric mean diameter (GMD) and geometric standard deviation (GSD) of the nucleation mode in the chamber event, obtained through inverse modelling, using different models.

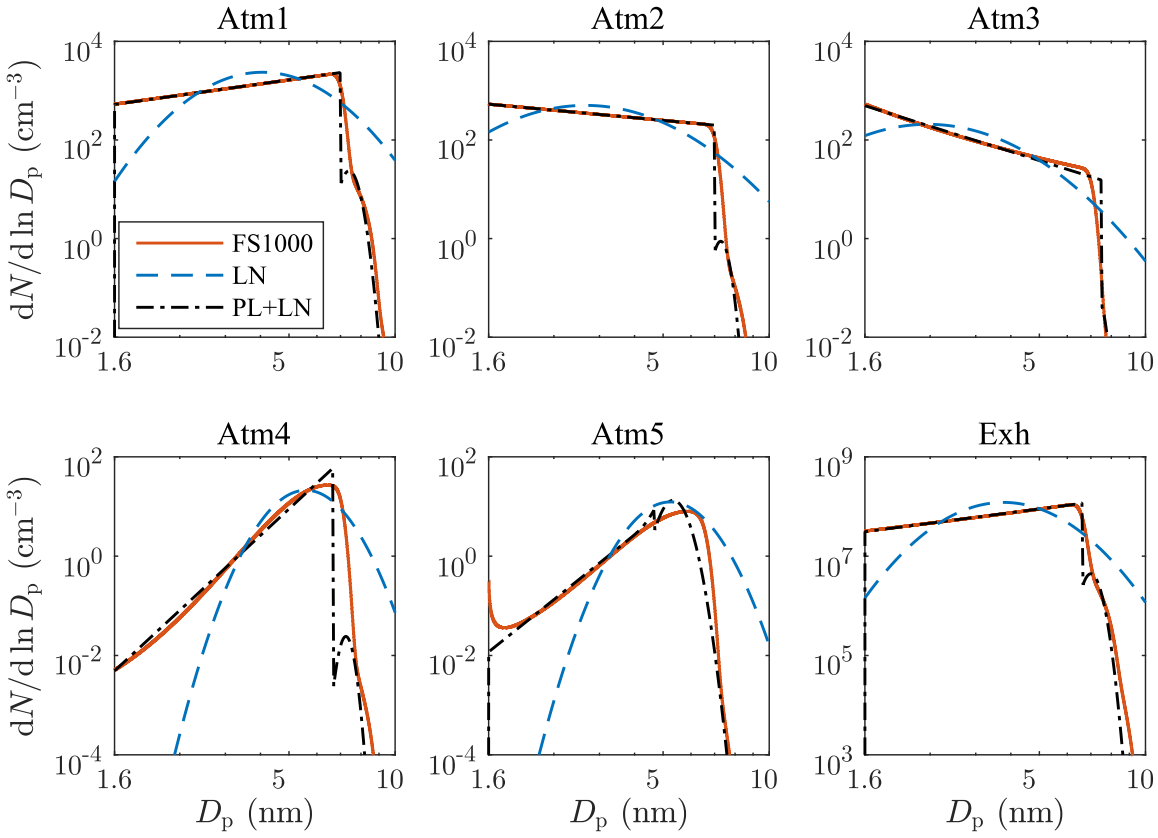

Figure 10. Particle size distributions at the ends of the test case simulations produced by different models. The input parameter sets are shown in Tab. 1. FS1000 denotes the fixed-sectional model with 1000 size sections. Note the different scales in the vertical axes on the bottom row.

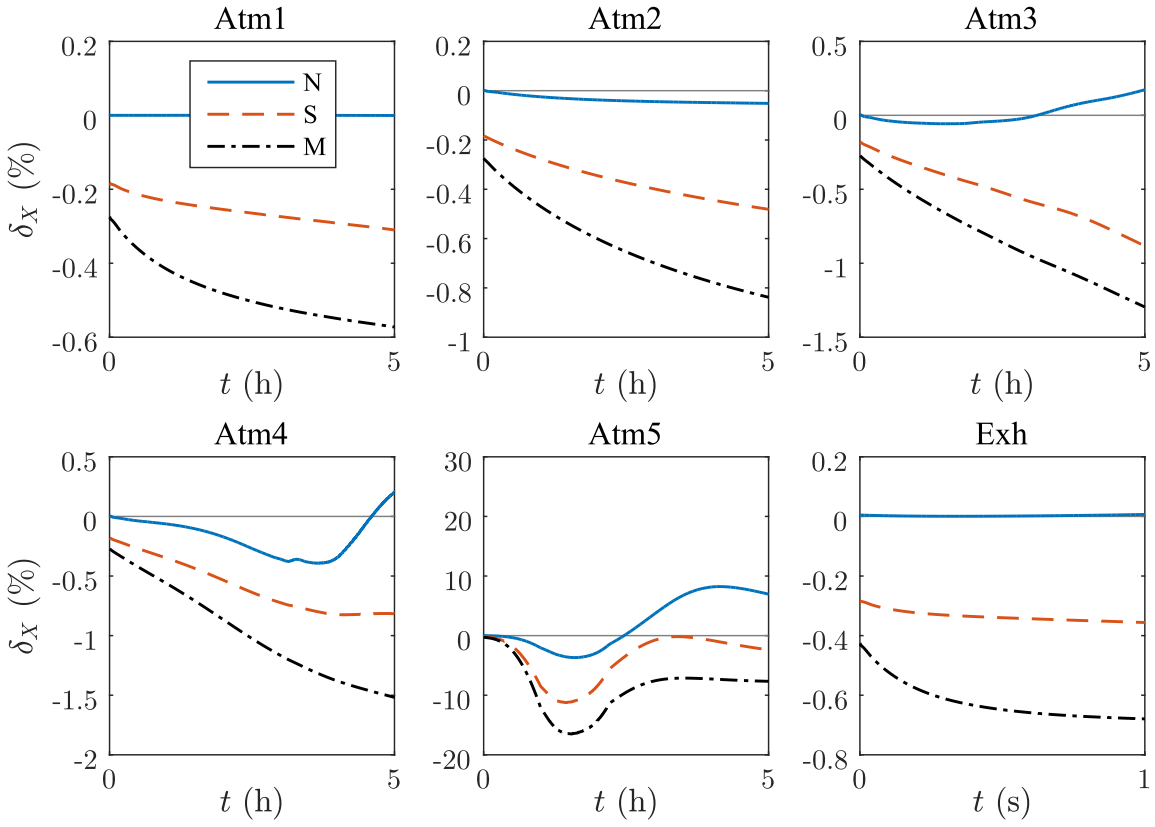

Figure 11. The relative errors of the moments (δ_X) in the test cases produced by the PL+LN model. The input parameter sets are shown in Tab. 1.

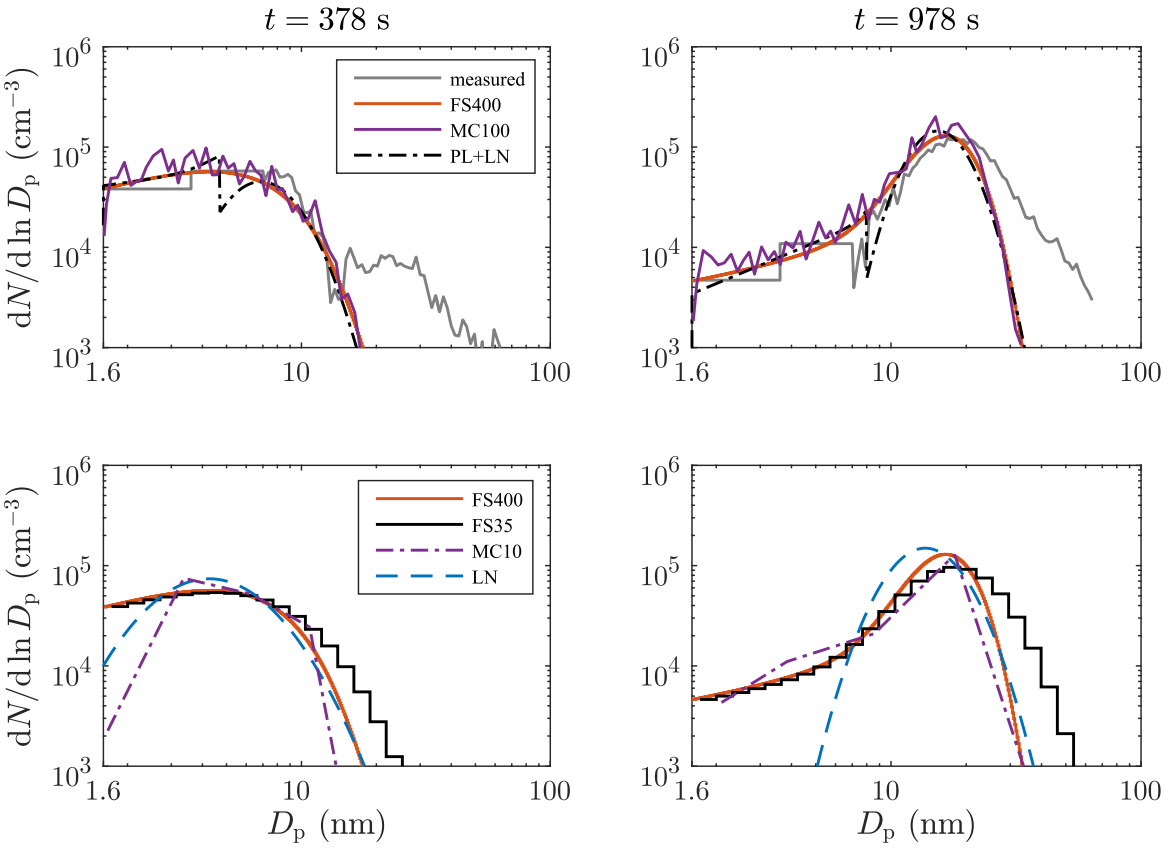

Figure 12. Particle size distributions in the chamber event 378 and 978 s after the UV lights were switched on. The top row shows the accurate model outputs together with the measured distribution. The bottom row shows the less accurate model outputs together with the accurate FS400 model output. The measured distributions include also the background distributions around 30 and 50 nm which were excluded from the simulations. The abbreviations are explained in Tab. 3.

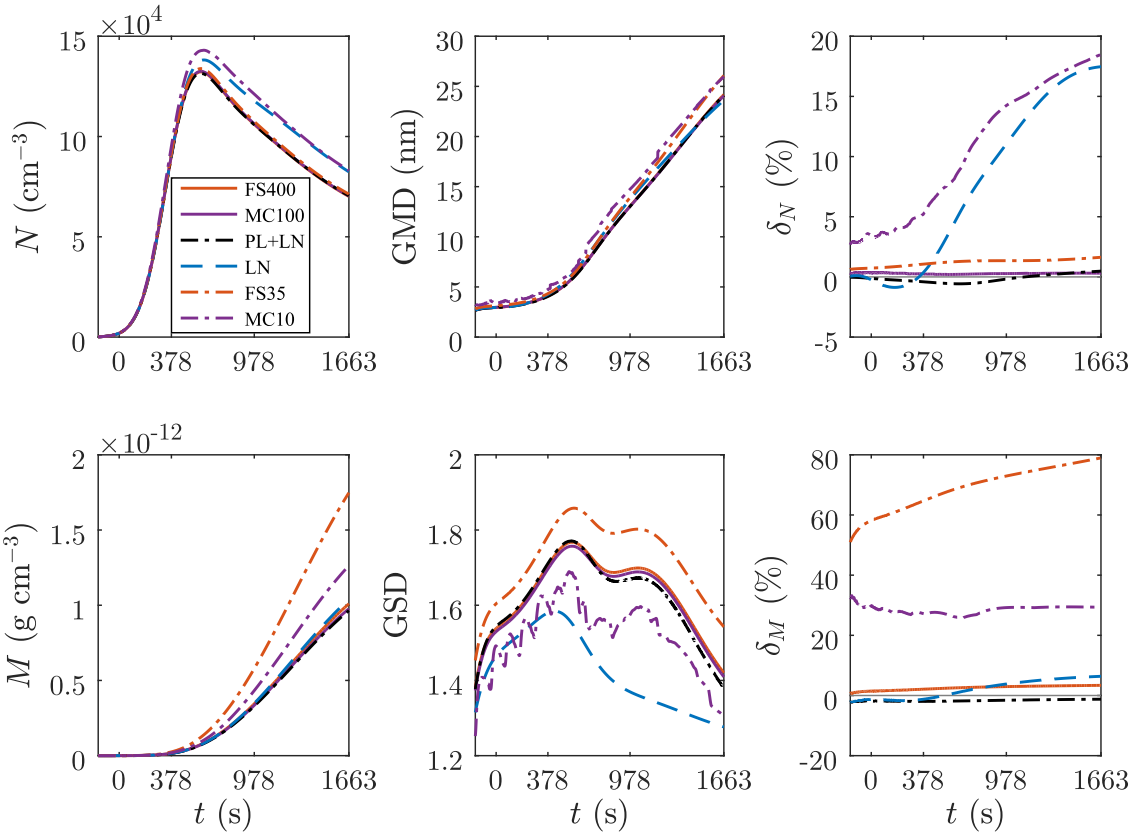

Figure 13. Number (N) and mass (M) concentrations, GMD, and GSD of the nucleation mode and the relative errors of the concentrations (δ_N and δ_M) in the chamber event, produced by different models. The outputs of the FS400 and the MC100 models are nearly equal, and thus they are difficult to distinguish in the figure.

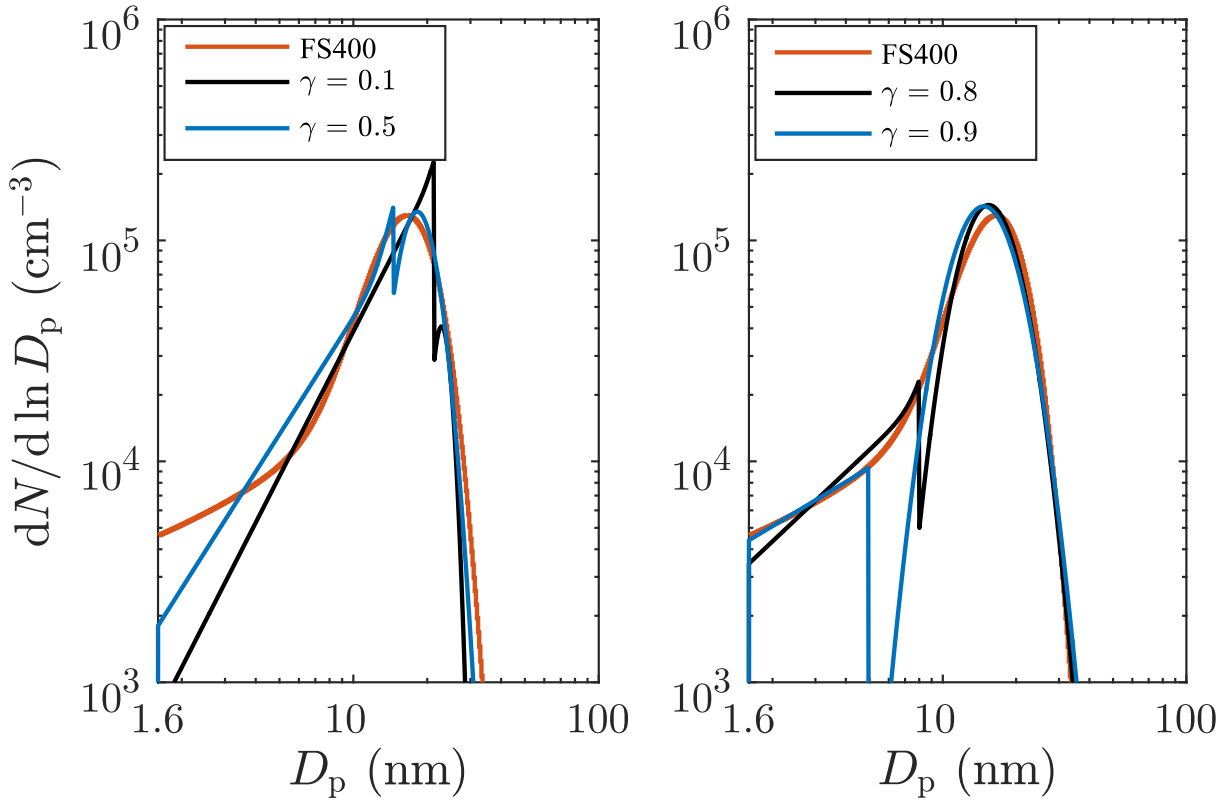

Figure 14. Particle size distributions 978 s after the UV lights were switched on, with the different values for the condensational transfer factor γ using the PL+LN model compared to the FS400 model.

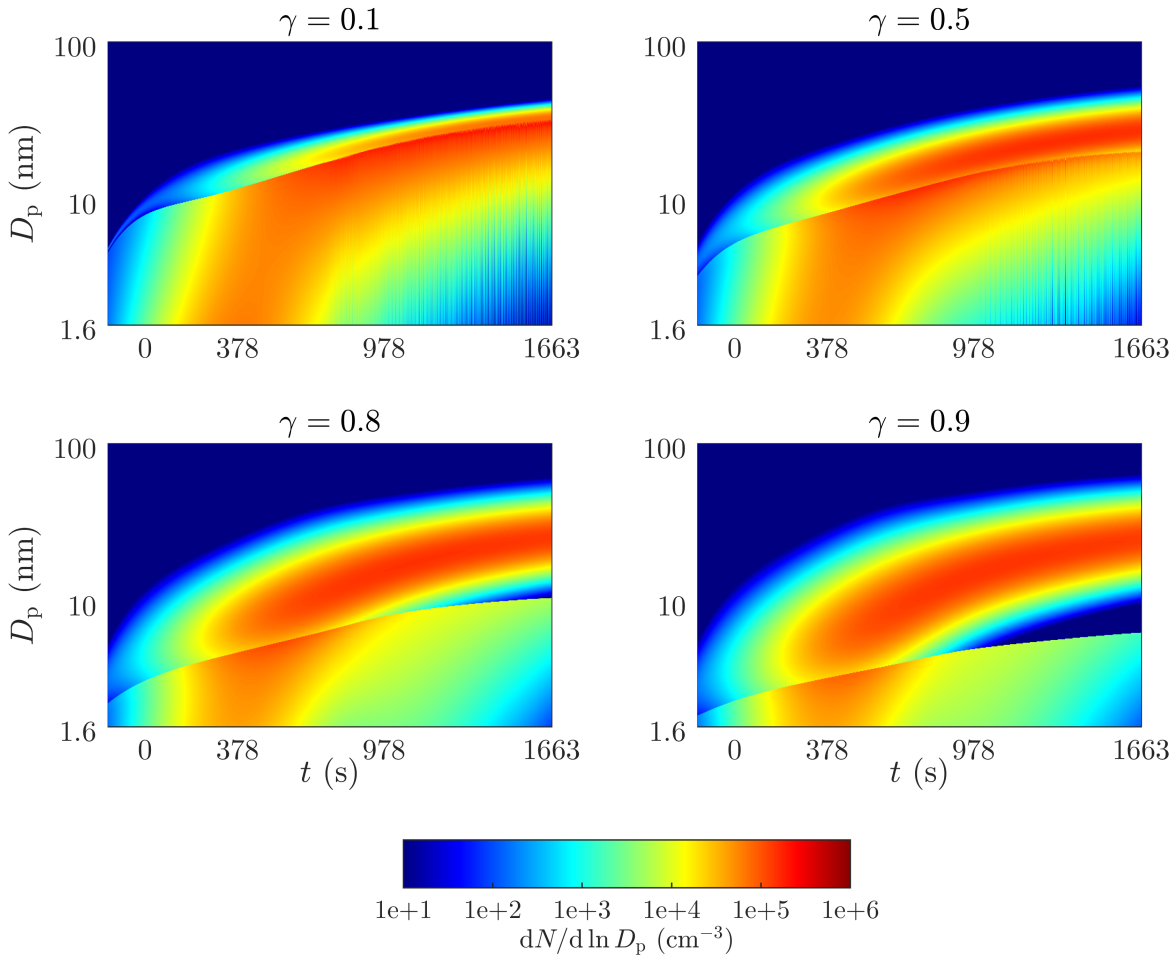

Figure 15. Contour plots of particle distributions simulated by the PL+LN models with different values of γ in the chamber event.